The Impact of varying thermal and hydraulic properties on HT-ATES systems

A Study Based on Sediments of the Maassluis Formation with a focus on thermal properties

AESM7000: Master Thesis

Luis Barlet

Delft University of Technology

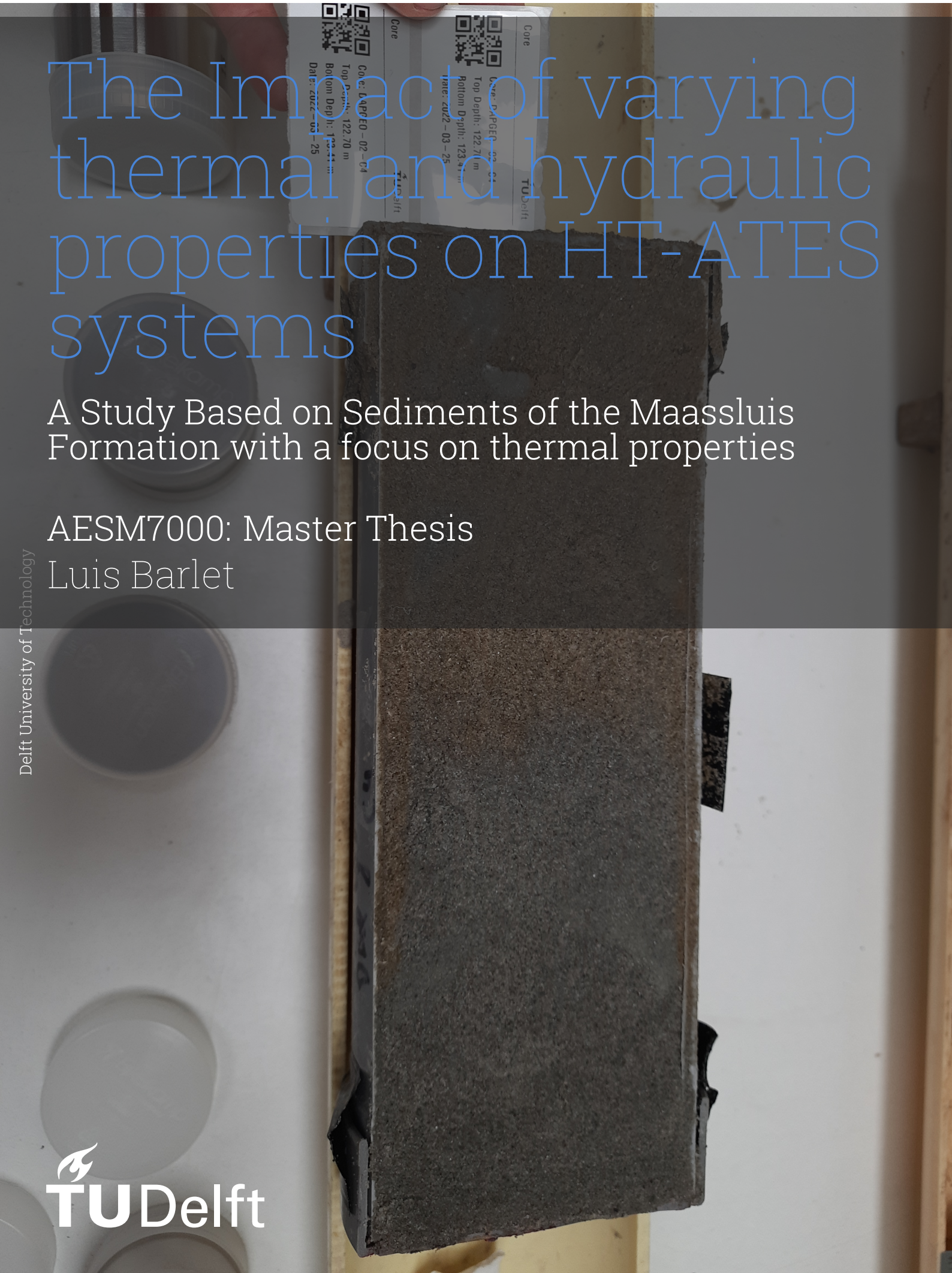

TUDelft

The Impact of varying thermal and hydraulic properties on HT-ATES systems

A Study Based on Sediments of the Maassluis Formation with a focus on thermal properties

by

Luis Barlet

to obtain the degree of Master of Science
at the Delft University of Technology,
Faculty of Civil Engineering and Geosciences

Student number: 5849454
Supervisors: Dr. M. Bloemendal, TU Delft
Prof. P. Vardon, TU Delft
S. Beernink TU Delft

TU Delft

Abstract

To address the gap of constant heat supply by geothermal doublets and the varying demand throughout a year, High Temperature Aquifer Thermal Energy Storage (HT-ATES) systems have attracted a growing amount of research interest as a way of storing the excess heat produced in summer for later use during the winter months.

The performance of seasonal heat storage systems in confined shallow aquifers depends on several (hydro)geological and design parameters. The storage aquifer and sealing aquitard characteristics are subject to uncertainty and spatial heterogeneity. The present study examines the variability of hydrological and, in particular, thermal properties in cores taken from boreholes of the Maassluis formation in four different locations in the Western Netherlands. Because the uncertainty of thermal properties is rarely implemented in (HT-)ATES models, it is the main focus of this research. In a laboratory study, the hydraulic conductivity and thermal properties of the cores and smaller-scale core plugs are measured to create a database of those parameters for the Maassluis formation, which is a promising heat storage target. The samples are classified according to their grain size and evaluated with respect to their spatial variability. Results yield thermal conductivities ranging from $1.35 W/mK$ to $2.37 W/mK$ for clay samples and from $2.05 W/mK$ to $2.94 W/mK$ for sands.

These thermal conductivities are subsequently utilized to populate a numerical model of a potential HT-ATES system at the TU-Delft campus, using the SEAWAT code. The present study aims to assess the impact of the expected range of thermal conductivity in the aquifer and sealing layers on two key aspects: firstly, the recovery efficiency over the lifetime of the system, and secondly, the thermal impact on the subsurface.

Simulation outcomes demonstrate that recovery efficiency differences are marginal for varied thermal conductivities. In contrast, the vertical hydraulic conductivity of the aquifer exerts a significant influence, resulting in absolute recovery efficiency differences of up to 7% in the modeled scenarios. Varied thermal conductivity of the sealing layer modeled can have a noticeable thermal impact on the subsurface around the system, while the horizontal spread of heat into the aquifer is predominantly influenced by buoyancy flow, caused primarily by larger vertical hydraulic conductivities.

The overall impact of the uncertainty of thermal sediment properties on system performance is minor when compared to other uncertainties However, the effect of thermal plume spread could be significant, depending on the surrounding environment.

Contents

List of Figures

List of Tables

1

Introduction

1.1. Context of the Research

In view of the increasingly urgent need to reduce CO_2 emissions to achieve climate goals (UN, 2015) there is a growing demand for sustainable and fossil-fuel-free energy production. The sector of building heating (and cooling) is no exception. As it is responsible for approximately 40% of the energy consumption (RHC, 2013), the supply of clean heat to buildings plays an important role in the energy transition.

This is where energy production and storage using the subsurface can contribute to achieving these goals and decarbonizing that sector. Shallow and deep geothermal energy gives access to environmentally friendly heat (and power) to supply even whole city quarters. Although deep geothermal wells can be a constant and steady source for heat, they come with the problem of often not being able to produce the required heat in winter, while producing more than needed in the summer months(Bloemendal et al., 2020). This energy imbalance is visualized in figure 1.1 and raises the question of storing the excess heat produced for later use, when it is actually in demand.

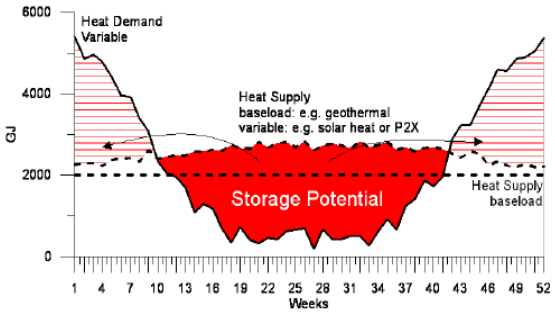

Figure 1.1: Difference in heat demand and supply throughout the year (Hartog et al., 2016)

This is where Aquifer Thermal Energy Storage (ATES) systems can provide a solution. Heat stored in suitable sedimentary aquifers can then be extracted when the demand is there in the colder winter months. Especially in the Netherlands the underground is already used quite widely for heat storage, with more than 2000 ATES systems in place (Bloemendal and Hartog, 2018). While most of these systems are Low-Temperature (LT)-ATES, High-Temperature (HT-ATES) are getting increasing attention in the past years (Drijver et al., 2019). With storage temperatures of up to 90°C High-Temperature systems present themselves as an ideal way to store excess heat from the before mentioned deep geothermal wells or waste heat from industrial plants.

One place where the feasibility of that coupling of HT-ATES with a geothermal plant has been researched is the TU Delft geothermal plant (Bloemendal et al., 2020), located in the province of South Holland, the Netherlands. In multiple research projects (for example WINDOW: Beernink, Oerlemans, et al., 2022) potential target formations have been identified.

A sedimentary formation that meets the required criteria to be considered as a promising target aquifer, is the Maassluis formation in the Netherlands (Bloemendal et al., 2020). While it shows to be promising for using it as HT heat storage, there still is a large uncertainty attached to the relevant subsurface parameters regarding their absolute values, as well as their spacial extent and heterogeneity on different scales. The existence of actual field data and samples from the formations of interest is often limited, so in the process of modeling these subsurface storage systems assumptions have to be made or models are overly simplified. This includes the presence of different sedimentary layers, but also their, for example, hydraulic conductivity or thermal properties.

While the hydraulic conductivity is usually adjusted based on the local hydrogeology of the aquifer to be modeled, the same is not the case for the thermal properties (for example: Bloemendal et al., 2021). These properties are almost never measured in the field, so here typically just one general value is assigned to the bulk sediment inside the systems aquifers and/or aquitards. The focus on the hydraulic conductivity is understandable, as this will significantly impact system performance and together with the storage geometry is a big performance factor to consider (Bloemendal and Hartog, 2018). Nevertheless, an accurate representation of actual thermal properties of the aquifers and sealing layers modeled, impacts heat losses and therefore the simulation outcomes.

In the case of HT-ATES the thermal aquifer and aquitard properties are especially of interest because of additional problems caused here due to large temperature differences between injected and ambient water in the hot well of a doublet. Because of this difference density-driven flow occurs, that usually is neglected in LT-ATES models but can have a large impact on the recovery efficiency of HT-ATES systems (Beernink et al., 2024). It is therefore critical for economically feasible operation and longevity of such systems.

The goal is to minimize heat losses to achieve higher recovery efficiencies of the stored heat while the temperature influence on the layers around the storage aquifer can also be of interest, where other ATES systems or drinking water resources could be affected and that effect is desired to be minimized. Understanding how these properties vary across the formation can lead to more accurate representation in models and because of that more precise prediction of system performances. Additionally, by doing that, the actual impact of varying thermal properties across the ranges determined can be quantified.

In the 4 pilot wells in Leeuwarden, in the North of the Netherlands, and Delft, Maasdijk and Rotterdam in the South-West of the Netherlands, that were drilled as part of the before-mentioned research, coring has taken place. Consequently a number of cores is available for further hands-on research at different scales at TU Delft.

These cores will be used for laboratory studies to address the problem of the uncertainty of sediment hydraulic and thermal properties and the effect of those changing properties on the operation of HT Aquifer Thermal Energy storage.

1.2. Objective of the Research

The problems described above make it necessary to further investigate the available cores on different scales. The insights gained during that study can then be used to create an underground model and quantify their impact. From the given level of knowledge the following research question arises as the main point to be addressed in this study:

”How large is the impact of the uncertainty and heterogeneity of thermal properties on the recovery efficiency and thermal influence of HT-ATES systems?“

This can further be grouped into a research package to be answered by a laboratory study:

- ”What are the thermal properties of Maassluis formation sediments within different samples of the formation?“
- ”How do these properties vary within the formation and in cores taken from different locations in the Netherlands?“
- ”To what degree are these changes linked to changes in other (hydraulic) properties?“

And a second package that is to be addressed by numerical modeling efforts:

- ”To what degree is the recovery efficiency of a potential modeled HT-ATES systems in the Maassluis formation sensitive to these changes?”
- ”How large is the thermal impact on the subsurface surrounding the system when varying these properties?”

To answer these question and tackle the knowledge gap in the impact of thermal properties on HT-ATES system performance various experiments are subject of this thesis. First a carefully executed set of lab measurements is performed. The information gained from the laboratory results and previous knowledge are then used to populate numerical underground models using SEAWAT. Different model scenarios are run with the goal to assess performance of HT-ATES systems under different conditions for an example system in the Maassluis formation in the Netherlands.

1.3. Report Structure

First, relevant background information is given in chapter 2 regarding the study area, the functioning principles of ATES systems and factors impacting their performance, as well as properties measured and the numerical code used. Then the methodology of the research is shown in chapter 3. The first part here deals with the execution of lab measurements to create a Maassluis subsurface database and the second part goes through the setup of the SEAWAT underground model and the different scenarios modeled. Following that the results for the lab and the modeling work are presented in chapter 4 Afterwards the results are analyzed and discussed and the research questions consequently answered in chapter 5. Lastly, the report is concluded in chapter 6.

2

Background

2.1. Geological Background

The Maassluis is a geological formation that is part of the upper north sea group. It is located in the west to central Netherlands and extends also into the Dutch offshore area. Its exact extend is shown in figure 2.1. It was deposited from late Pliocene to early Pleistocene in a near coastal depositional environment at the southern margin of the north sea basin (H. Jansen et al., 2004) The name was first introduced by Doppert et al., 1975 for marine shell-bearing sands. It is named after the town Maassluis in the southern Netherlands where the original type borehole can be found (Huizer and Weerts, 2003).

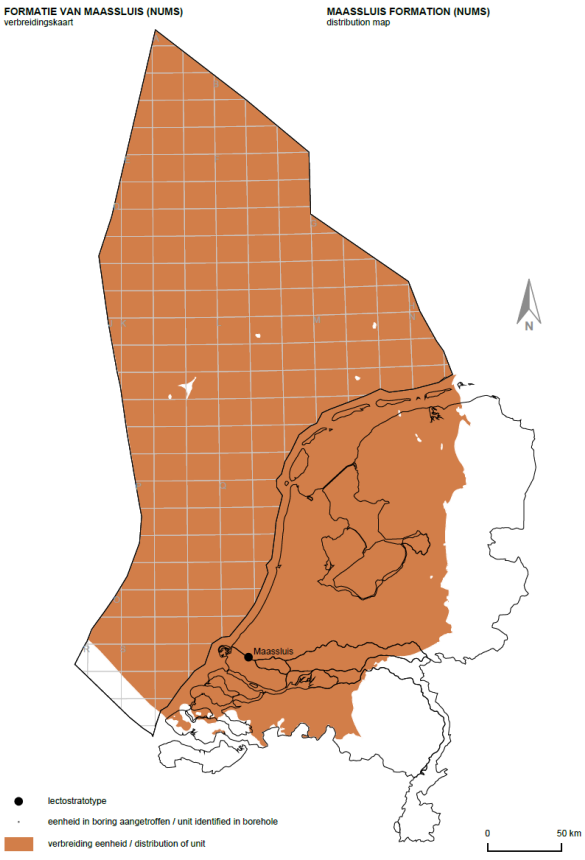

Figure 2.1: Extends of the Maassluis formation in the Netherlands (from TNO-GDN, 2024)

The lithology is dominated by very fine to medium coarse gray sands with grain sizes from 63 to 300μm. These sands contain shells and chalk as well as micas. Additionally clay layers and lenses are present that are dark gray and often silty. Thin shell layers and organics are also found sparsely.

H. Jansen et al., 2004 classify the deposition as a coastal environment with shell beds in the eastern part, that grades into a more open marine environment westwards towards the current shoreline of the Netherlands with a coarsening upwards trend. Between Den Haag and Noordwijk they find that the formation is made up of two distinct units, with coastal sands at the top and coarsening upwards clay and sandy clay units underneath. This is confirmed by Noorbergen et al., 2015, who find, based on the Noordwijk borehole, a shallow marine bottom part with clear coarsening upwards in Gamma Ray (GR) logs, and a near shore part on top of that.

The boundary to the underlying layer in the study area, the shallow marine Oosterhout formation, is gradual, characterized by a decrease in grain size and increasing glauconite content in the upper part of the Oosterhout. Where a marine clay layer is present at that depth - mostly towards the west of the formation extend area - the boundary to the Oosterhout is sharp (TNO-GDN, 2024).

The Maassluis is overlain mostly by fluvial and tidal deposit sand and clay of the Waalre formation in the southern part of the study area. The boundary is sometimes hard to distinguish, it is classified by the absence of marine shells in the Waalre and Peize formation. The occurrence of reworked shells in the bottom parts of these formations is possible though, making the upper boundary of the Maassluis unclear (Huizer and Weerts, 2003).

General directional trends are present in the Maassluis. The overall grain size is generally decreasing from the SE towards the NW, the same is true for the shell content. All in all there is a coarsening upwards trend, from clay to sand, that indicates the depositional environment gradually shallowing (Huizer and Weerts, 2003).

The depth of the formation ranges between 50m and 300m below the surface (Noorbergen et al., 2015). While the thickness of the formation is very variable ranging from a few 10s of meters to about 250m, as it is determined by the shape of the north sea basin during deposition, there is a trend apparent of increasing thickness towards the NW.

2.2. (HT-) Aquifer Thermal Energy Storage

The working principle of Aquifer Thermal Energy Storage (ATES) systems has been roughly outlined in the introduction already. The excess available heat in form of hot water, in this case stemming from a geothermal doublet producing steadily throughout the year cannot be utilized and therefore needs to be stored in order for it not to be wasted. In this kind of Open Underground Thermal Energy Storage system an aquifer is targeted with a variable number of wells, depending on the specific system. In most scenarios at least one hot/warm and one cold well are used. The principle is illustrated in figure 2.2. In summer excess warm water is injected in the warm well, while cold water is extracted from the cold well. In winter the injection/extraction are reversed to produce the warm water. Although the figure shows LT-ATES operation, the same principle applies to hot injection temperatures.

Injection and extraction over each storage cycle can be in balance or unbalanced over every cycle, with balanced schemes usually more favorable to reduce thermal impact over time and keep recovery efficiency high throughout a system’s lifetime.

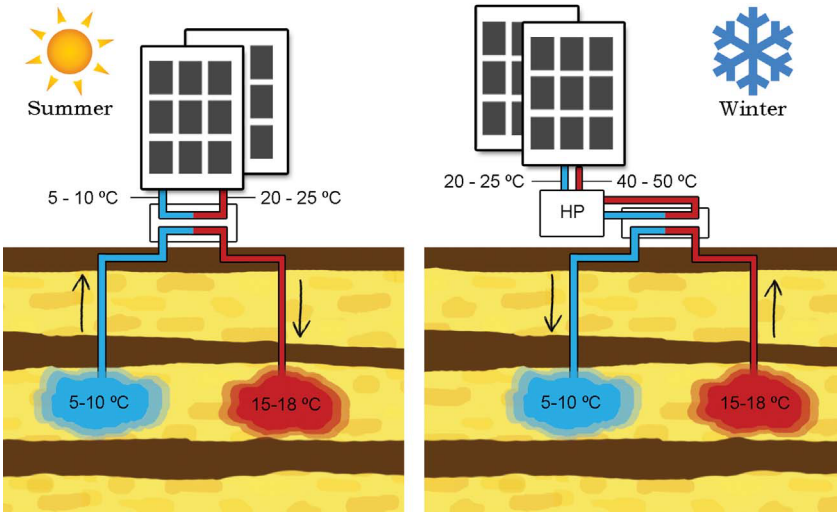

Figure 2.2: Illustration of the basic working principle of LT-ATES as seasonal storage (from Bloemendal and Hartog, 2018)

2.2.1. Subsurface Requirements for HT-ATES

In order for a system to operate efficiently a number of requirements have to be met.

Guglielmetti, 2021 conducted research on the national potential of HT-ATES in the Netherlands. They determined generally high potential for the province of South Holland in the Maassluis formation, which this study focuses on. Additionally they came up with a number of subsurface criteria needed to be met as a minimum for planned HT-ATES systems:

- Storage aquifer of at least 15m thickness
- (Horizontal) hydraulic aquifer conductivity of at least $3 - 5m/d$, fine to medium coarse sand is favored
- Confining layer above - and preferably also below - the aquifer to limit buoyancy flow and restrict losses
- Depth of more than 50m to limit the negative effects on the shallow subsurface
- Limited amounts of groundwater flow

Depending on local conditions and operational parameters of a planned system, larger aquifer thicknesses or depth might be required.

Factors like the hydrogeological properties of the target aquifer, its size or the required storage volume and planned injection temperature all influence how an ATES system performs at a specific location.

It is a complex system with lots of processes interacting (Beernink et al., 2024), so how well a system works depends on various parameters. These are outlined in the following chapter

2.2.2. State of the Art

Fleuchaus et al., 2018 looked at the worldwide application of Aquifer Thermal Energy Storage and found that of the more than 2800 systems operational at the time of their research, 85% of those where located in the Netherlands. Overall 99% of all systems were low temperature (LT-)ATES systems with storage temperatures of 25°C or less.

Looking at research conducted regarding HT-ATES in the Netherlands, Wesselink et al., 2018 concluded, that HT-ATES has potential in the Netherlands under existing policies and could offer a good

solution if it were for example to be coupled with geothermal heat plants. As part of the WINDOW research project, Zwamborn, 2022 identified potential locations for HT-ATES and their integration in district heating networks. They show that locations in the western part of the Netherlands are generally more favorable for HT-ATES, largely due to the geological conditions found there. Other studies come to the same conclusion (Dinkelman and van Bergen, 2022), which is beneficial as this is the most populated area of the Netherlands with highest heat demand and also the area of interest for this research.

Especially the Maassluis formation has been identified as a promising target for underground heat storage in previous studies (Bloemendal et al., 2020). Main aspects that show the formations high potential as a storage aquifer are its thickness and high hydraulic conductivity.

Currently only one full-scale HT-ATES is operational in the Netherlands. That is the system in Middenmeer, which became operational in 2021 (Dinkelman, 2022). It targets the Maassluis formation over a depth of 360-383m at a storage temperature of about 85°C.

In the Netherlands ATES, as open loop geothermal systems, fall under the water law. The province of Zuid-Holland, where three of the pilot wells studied here are located, allows injection temperatures exceeding 25°C only as part of a research or pilot project (Provincie Zuid-Holland, 2015). For the implementation of HT-ATES on a broader scale changes to that approach therefore would be required. What is allowed in terms of thermal impact on sealing layers depends on local regulations.

2.2.3. Storage Characteristics

The shape of the thermal plume of the injected warm water in the aquifer will change depending on a number of properties of the subsurface and the injected water.

The aquifer volume infiltrated causes, according to Doughty et al., 1982, simplified a cylinder with a hydraulic radius R_h of:

$$R_h = \sqrt{\frac{V_{in}}{n\pi L}} \tag{2.1}$$

For an ideal, fully penetrating well with no losses and ignoring heterogeneities, the thermal radius is given by (Bloemendal and Hartog, 2018):

$$R_{th} = \sqrt{\frac{c_w V_{in}}{c_{aq}\pi L}} \tag{2.2}$$

where V_{in} is the stored volume of water, L the thickness of the aquifer and c_w and c_{aq} are the volumetric heat capacities of water and the storage aquifer. The thermal radius is lower than the hydraulic radius due to the heat being stored in the sediment grains of the aquifer (see figure 2.3). For the given idealized case the relation between the two is approximately $R_{th} \approx 0.66 \cdot R_h$. The thermal plume of a HT-ATES system will differ from the cylindrical shape typical for LT-ATES system because of the tilting of the thermal front, but the thermal radius still is an interesting parameter to consider even for those cases.

The ratio of screen length over thermal radius L/R_{th} was introduced by Doughty et al., 1982 as a dimensionless parameters that can reflect thermal recovery efficiencies for a storage with those specific parameters.

With the storage volume V of $250,000m^3$, aquifer thickness of 50m, a water heat capacity of $4.2MJ/m^3/K$ and an average aquifer heat capacity of $2.66MJ/m^3/K$, the thermal radius for our system therefore will be about 50m. This is leads to a L/R_{th} ratio of 1. According to Beernink et al., 2024, for HT-ATES where buoyancy driven flow - which will be covered in the next section - can potentially lead to large heat losses due to tilting of the thermal front, ratios of 1 or lower can strongly reduce losses.

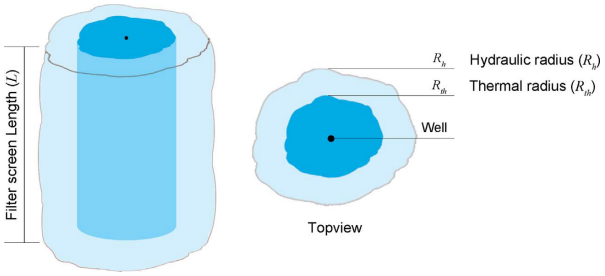

Figure 2.3: The shape of the thermal and hydraulic radius of an idealized ATES (from Bloemendal and Hartog, 2018)

2.2.4. Heat Loss Principles

Not all injected heat can be recovered from the storage aquifer in each cycle. This is caused by the heat losses due to three governing principles: Conduction and Dispersion, which occur for all ATES systems, as well as buoyancy flow, or free convection losses, which are only relevant in systems with increased temperature differences between injected and ambient fluid (Doughty et al., 1982). The three principles are visualized in figure 2.4.

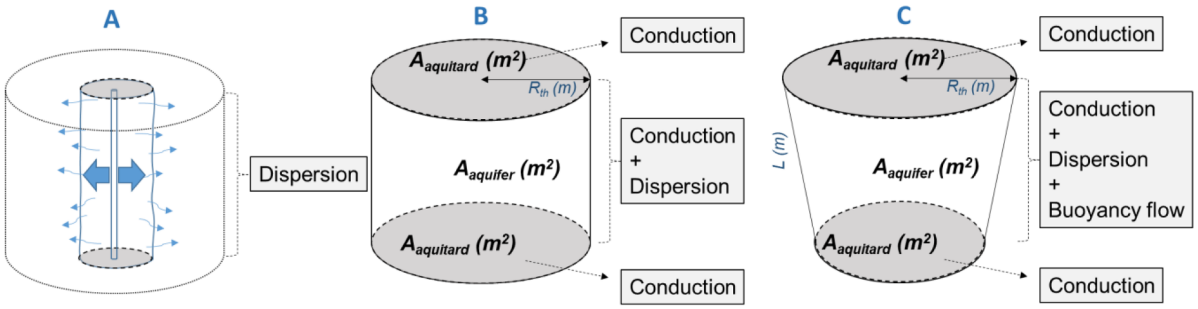

Figure 2.4: Heat loss principles in confined aquifers (from Beernink et al., 2024)

2.2.4.1. Conduction and Dispersion

Heat losses in ATES systems occur due to conduction and mechanical dispersion at the boundary of the stored heat body. The effective thermal dispersion D_{eff}, given by Bloemendal and Hartog, 2018, describes the contribution of conduction and dispersion to losses. Conduction is represented by the first part of the formula and depending on the volumetric heat capacity c_f of the fluid, and the thermal conductivity λ_{aq} and porosity ϕ of the aquifer:

$$D_{eff} = \frac{\lambda_{aq}}{\phi c_w} + \alpha \frac{v}{\phi} \tag{2.3}$$

The rate of conduction can be determined from this by the standard deviation $\sigma = \sqrt{2D_T t}$, where t is the storage time and D_T is the first part of equation 2.3, the effective thermal dispersion. The second part of 2.3 is the mechanical dispersion, depending on porosity, dispersivity α and the water flow velocity v. This is the forced convection from injection/extraction at the well for cases without groundwater flow.

Bloemendal and Hartog, 2018 show that, even at high assumed dispersivity values the conduction term dominates versus dispersion unless very early in the injection cycle.

Recovery losses of a conductive static thermal cylinder according to Doughty et al., 1982 are given as η^{cond}:

$$\eta^{\text{cond}} = \left(1 - 2\frac{\sqrt{Dt/\pi}}{R_h}\right)\left(1 - 2\frac{\sqrt{Dt/\pi}}{L}\right) \tag{2.4}$$

The left part of the equation is the conduction into the aquifer (the radial component) and the right part the vertical conduction of heat into the aquitards. As there is close to zero flow into the aquitards, dispersion losses can be neglected at the top and bottom of the thermal plume for fully penetrating wells (Doughty et al., 1982).

As injection goes on in a storage cycle the thermal front movement is dominated by advective heat transport of the injected water, leading to a sharp heat interface. During storage and extraction, conduction will be dominant, causing a less sharp heat interface. Heat staying behind due to that will cause an increase of efficiency over multiple cycles Bloemendal and Hartog, 2018). Therefore conductive losses are minimized when the surface area of the cylindrical temperature plume A/V is as small as possible (Bloemendal and Hartog, 2018):

$$\frac{A}{V} = \frac{2\pi R_{th}^2 + 2\pi R_{th} L}{\pi R_{th}^2 L} = \frac{2}{L} + \frac{2}{R_{th}} \tag{2.5}$$

2.2.4.2. Buoyancy Flow

Additionally a third heat loss principle occurs in High-Temperature ATES systems. This buoyancy flow (also called free convection) is caused by differences in density and viscosity between the colder ambient water and the hot water injected into the aquifer. Due to its lower density the stored hot water will rise upwards in the aquifer by free convection, tilting the initially vertical thermal front over time, like it is visualized in figure 2.5. That causes hot water at the top of the aquifer to flow away from the well while cold water will flow towards the well at the bottom (Schout et al., 2014).

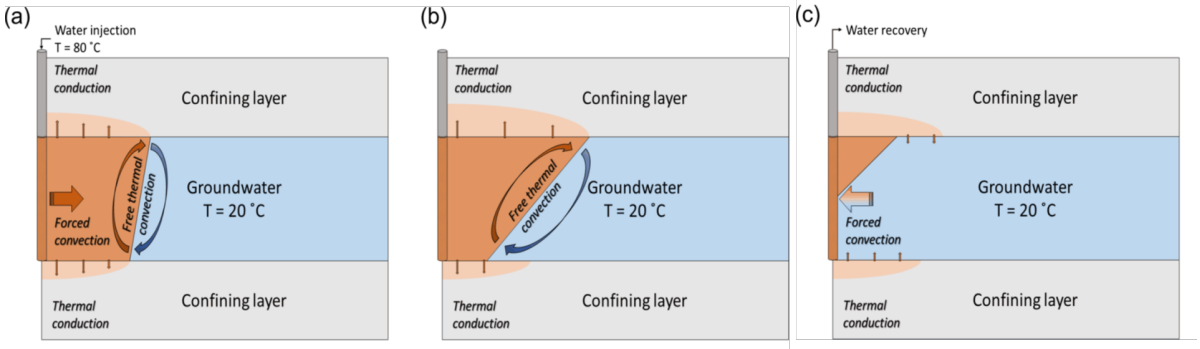

Figure 2.5: The principle of buoyancy flow from injection of hot water in cooler aquifer throughout a seasonal injection (a), storage (b) and extraction (c) cycle (from Van Lopik et al., 2016)

The characteristic tilting time t_0 is the amount of time it takes until a vertical thermal front reaches an angle of 60°, assuming an infinite horizontal aquifer (Hellström et al., 1988):

$$t_0 = \frac{H}{\sqrt{k_h \cdot k_v}} \cdot \frac{C_a}{C_w} \cdot \frac{\pi^2 \cdot (\mu_a + \mu_i)}{32 \cdot G \cdot (\rho_a - \rho_i) \cdot g} \tag{2.6}$$

H is the aquifer thickness, k_h and k_v are the horizontal and vertical aquifer permeabilities, C_a and C_w are the volumetric heat capacities of the aquifer and of water, μ_a and μ_i are the viscosities of the ambient and the injected water, ρ_a and ρ_i are the densities of the ambient and the injected water, G is Catalan's constant (0.915) and g is the gravitational constant.

If the length of a cycle is less than that tilting time, the convection in the system becomes significant. The tilting time is predominantly influenced by the temperature difference between injected and ambient ground water, the aquifer thickness and its permeability (Sheldon et al., 2021). While the storage volume and aquifer thickness also affect t_0, Schout et al., 2016 showed that higher recovery efficiencies generally occur in systems with longer characteristic tilting time.

Overall conduction, dispersion and buoyancy flow are determined by the given storage geometry and the potential for buoyancy, which increases when the temperature difference of the injected and the

ambient groundwater and the hydraulic conductivity in vertical direction increase (Beernink et al., 2024). In these systems with high buoyancy potential small L/R_{th} ratios reduce heat losses from tilting of the thermal front. In LT systems most heat losses are due to conduction, while in HT systems buoyancy flow is responsible for the most heat losses (Beernink et al., 2024). It is unclear however how the interaction between the different loss principles changes their contribution over large ranges of storage conditions possible.

2.2.5. Heat Recovery

The performance of ATES systems is usually quantified with the recovery over each injection and extraction cycle, meaning yearly in case of this study. The recovery efficiency η_{th} given by Bloemendal and Hartog, 2018 is defined as the extracted energy E_{out} over the injected energy E_{in} per cycle:

$$\eta_{th} = \frac{E_{out}}{E_{in}} = \frac{(T_{extraction} - T_{ambient}) \cdot V_{extraction} \cdot \rho_w \cdot c_w}{(T_{injection} - T_{ambient}) \cdot V_{injection} \cdot \rho_w \cdot c_w} \tag{2.7}$$

One way to assess the recovery efficiency of HT-ATES is the use of the Rayleigh number Ra. This number was first introduced by Gutierrez-Neri et al., 2011 and indicates the strength of free convection versus heat conduction. It was found to be correlated with the calculated recovery efficiency of a HT-ATES system. The Ra number is defined as:

$$Ra = \frac{g\rho\alpha H k_v \Delta T}{\mu D} \tag{2.8}$$

where g is the gravity acceleration, ρ is the density of the fluid, μ its dynamic viscosity, α its thermal expansion coefficient, k_v the vertical permeability and D the thermal diffusivity of the aquifer. H is the characteristic length scale, which is taken as the aquifer thickness and ΔT is the difference between injected and ambient groundwater temperature.

Above a critical Rayleigh number Ra_c, approximately $4\pi^2$, free convection is the dominant heat transfer process, while below it heat conduction dominates. For higher Ra the recovery efficiency decreases, as the losses to free convection are larger compared to conductive losses.

Previous studies have shown the recovery efficiency in high temperature ATES to be most sensitive to changes in (aquifer) permeability, injection temperature and injection volume, while the impact of changing thermal conductivity is much smaller (Schout et al., 2014).

Here the storage geometry of the system is very important with respect to buoyancy flow occurring in systems with higher storage temperatures. The recovery efficiency will improve significantly in HT cases with larger storage volumes (Kallesøe and Vangkilde-Pedersen, 2019). The storage geometry depends on the aquifer dimensions and the mentioned injection volume, while the potential for buoyancy flow is dependent on the temperature difference between injected and ambient water and the permeability characteristics of the system (Beernink et al., 2024). The impact of buoyancy flow will decrease with smaller screen lengths, normally leading to higher recovery efficiency for those.

While the influence of varying thermal properties on the ATES system performance has been subject to multiple studies in the past, none of them cover their impact on HT-ATES systems in detail for thermal properties obtained from actual laboratory measurements. Here the increased importance of free thermal convection is of major concern.

2.3. Sediment Properties

Present subsurface properties and their spatial distribution are highly uncertain. This is why it is of great interest to conduct measurements on core samples to reduce uncertainty ranges. Following from that is the goal of creating a property database for the Maassluis formation at the DAPGEO-02 borehole and secondarily also the LW, MSD and RD boreholes.

2.3.1. Thermal Properties

The three relevant parameters determining the transport and storage of heat in the aquifer matrix and pore space are thermal conductivity, thermal diffusivity and heat capacity.

The thermal conductivity is the measure of a material to conduct heat, where higher values mean a larger rate of heat transfer and denoted here by λ It is defined by Fourier's Law (Fourier, 1888):

$$q = -\lambda \nabla T \tag{2.9}$$

where q is the heat flux and ∇T is the temperature gradient.

The specific heat capacity c_s is the amount of heat required to heat up one unit of mass of a substance by one unit of temperature.

The thermal diffusivity α is related to the other two by:

$$\alpha = \frac{\lambda}{c_v} \tag{2.10}$$

where λ is the thermal conductivity and c_v the volumetric heat capacity, which is the specific heat capacity times the density ($c_v = c_s \cdot \rho$).

Unlike hydraulic properties the uncertainty range of thermal properties of sediments, where the general formation grain size and composition is known to some extent, is comparably small (figure 2.6). Another major difference with the hydraulic conductivity as a flow property is the negligible anisotropy present in the thermal material properties (Li et al., 2024). This makes the determination of the thermal properties of samples easier because the orientation of the sample does not have to be considered. When upscaling the thermal conductivity of sediments for modeling geothermal systems, Rühaak et al., 2015 showed, that the kind of upscaling approach only has a minor impact on the temperature distribution in the subsurface. The arithmetic mean of available conductivity data has proven to reflect the actual results well.

Depending on the class of the sediments present in a study area the thermal properties normally fall within ranges given in literature regarding typical values for each sediment class. The Dutch guidelines for underground storage (NVOE, 2006) for example give a thermal conductivity value of $2.4 W/mK$ for sand and $1.7 W/mK$ for clay. For the volumetric heat capacity a range of $2.2 - 2.9 MJ/m^3K$ is given for sand and $1.6 - 3.4 MJ/m^3K$ for clay. In figure 2.6 estimated ranges for sediments of different grain sizes are given. It can be seen that conductivity values between around $1 W/mK$ and $3.5 W/mK$ can be expected.

The actual thermal properties of individual samples are affected by a number of parameters, like the porosity, degree of saturation, the bulk density or the mineral composition of the soil (Łydżba et al., 2014). The thermal conductivity of soil is highly dependent on its degree of saturation. That relationship has been subject to multiple studies, for example Ore et al., 2024. Overall the soil thermal conductivity in fully saturated state is always significantly higher than in dry state. As we deal with the Maassluis formation, which is a confined aquifer in this study, all thermal property measurements will be carried out in fully saturated state to best reflect the subsurface situation present.

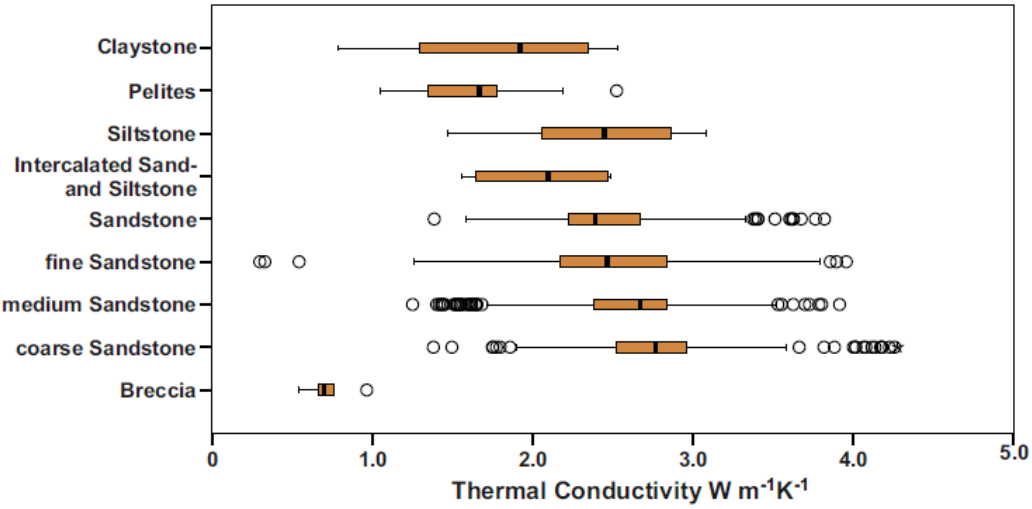

Figure 2.6: Thermal conductivities of different sediment classes (from Rühaak et al., 2015). The line inside the box represents the median, while the ends of the boxes are the first and third quartile.

Another aspect that has to be considered when dealing with aquifer storage at elevated injection temperatures is the temperature dependency of the thermal properties of sediments. While the difference in thermal conductivity between sediments at ambient and much larger temperatures is noticeable especially in non saturated soils, the effect decreases for fully saturated state, as experiments by Smits et al., 2013 show. They studied the thermal conductivities of sediments for varying saturation levels at temperatures between 30°C and 70°C and conclude that at full saturation temperature doesn't have a measurable effect on the thermal conductivity.

2.3.2. Hydraulic Properties

A major factor in the performance of ATES systems is the hydraulic conductivity of storage aquifer and sealing layers.

The hydraulic conductivity can vary over multiple orders of magnitude between different sediment types. It is also subject to a strong influence of anisotropy depending mainly on the layering within a stratified sedimentary aquifer. Bloemendal and Hartog, 2018 have looked at 204 (LT-)ATES systems in the Netherlands and found present horizontal hydraulic conductivities in the range of $5 - 45m/d$ for the aquifer. For HT systems values on the lower end of that can be desirable as that limits the occurrence of buoyancy flow.

The hydraulic conductivity in a sediment is dependent on the direction of flow, and therefore anisotropic. The anisotropy and heterogeneity of hydraulic conductivity at the scale of thermal energy storage systems can impact models and their resulting system performance and therefore needs to be carefully assessed for choosing the correct effective values for subsurface models that reflect the system. The heterogeneity in hydraulic conductivity fields can cause considerable uncertainty in the distribution of storage temperature plumes (Ferguson, 2007). On the other hand, both homogeneous and heterogeneous models have shown to realistically simulate the actual subsurface temperatures for ATES (Visser et al., 2015) According to Visser et al., 2015 and Bridger and Allen, 2014 the maximum thermal plume extent is underestimated for homogeneous models.

It therefore depends largely on the subsurface conditions and available data for each case studied, wether a heterogeneous modeling approach is beneficial. The studies mentioned here research LT-ATES systems where buoyancy flow is negligible. Therefore they show slightly different behavior from the HT system considered here or the models developed by Beernink, Barnhoorn, et al., 2022. Their research shows that homogeneous upscaled models are only applicable when layers varying on a

smaller (<m) scale are present. This difference will be discussed further later in chapter 5. In this study a homogeneous approach is chosen.

In layered aquifers the effective vertical anisotropy in hydraulic conductivity, meaning the ratio of horizontal (Kh) over vertical (Kv) conductivity, is very hard to determine and also scale dependent. The presence of thin (clay) layers with low vertical conductivity within larger sedimentary (sand) units influence Kv on the macroscale. When modeling sedimentary aquifers, that consist of a number of smaller horizontal layers with different properties, as one homogeneous layer, it will be anisotropic when the vertical hydraulic conductivity is considerably smaller than the horizontal hydraulic conductivity (Bakker and Bot, 2024). When no field derived estimate of the anisotropy is known a value of 10 is a good starting point for calibration. This means it needs to be adjusted accordingly when a model is calibrated. Based on that, and due to the lack of better field estimates, a base anisotropy value of 10 will also be used in the modeling efforts of this research.

The recovery efficiency is insensitive to hydraulic conductivity anisotropy for LT-ATES (<30°C), because no losses through buoyancy flow occur here. For HT systems the recovery efficiency increases with larger anisotropy. The effect is non-linear and decreases with growing anisotropy ratios (Beernink, Barnhoorn, et al., 2022).

2.3.3. Density and Porosity

The density and porosity of soils are additional parameters influencing the ability of an aquifer to store and transport heat as mentioned before. Therefore they are also of interest in this study to arrive at a complete dataset for the Maassluis formation sediments and as important parameters for model setup. Typical soil densities are within the range of $2.55 - 2.7 g/cm^3$, with a value of $2.65 g/cm^3$ therefore used commonly (Blake, 2008). For a selection of samples particle density ρ_p measurement are carried out using a gas pycnometer. That calculates the density based on the given sample mass m and volumes of particles and pores of the sample:

$$\rho_p = \frac{m}{V_{particles} + V_{closed-pores}} \tag{2.11}$$

From those results it is possible to determine the porosity Φ of the original sample using the following relationship:

$$\Phi = 1 - (\rho_b / \rho_p) \tag{2.12}$$

where ρ_b is the bulk density. The porosity can also be calculated using a method based on the difference between the saturated and the dry sample weight:

$$\Phi = \frac{m_{sat} - m_{dry}}{\rho_{water} \cdot V} \tag{2.13}$$

V is here the volume of the entire bulk sample.

2.4. Simulations

2.4.1. SEAWAT Model

The software package SEAWAT (Guo and Langevin, 2002) is used to simulate the combined groundwater flow and heat transport problems of the modeled HT-ATES systems.

SEAWAT combines for that purpose the hydrogeological MODFLOW model (Harbough, 2000) and MT3DMS (Zheng and Wang, 1999), a multi-species solute transport model.

For scripting and running the model in Python code, the FloPy implementation developed by Bakker et al., 2016 is used.

The simulation of heat transport in SEAWAT is based on the mathematical similarity between solute and heat transport. Conduction and convection in heat transport are analogous to diffusion and advection in solute transport. Therefore the solute transport formulation from MT3DMS is modified as follows to simulate heat transport in SEAWAT (Thorne et al., 2006):

$$\left(1+\frac{1-\phi}{\phi}\frac{\rho_s c_s}{\rho_f c_f}\right)\frac{\partial(\phi T)}{\partial t}=\nabla\cdot\left[\phi\left(\frac{\lambda_b}{\phi\rho_f c_f}+\alpha\frac{q}{\phi}\right)\cdot\nabla T\right]-\nabla\cdot(qT)-q_s' T_s \tag{2.14}$$

here ϕ is the effective porosity, ρ_s the density of the solid, c_s the specific heat capacity of the solid, α the dispersivity, q' is a source or sink and T_S the source temperature.

The Preconditioned Conjugate-Gradient (PCG2) solver by Hill, 1990 is used to solve the finite-difference groundwater flow equation and the standard implicit solver for the MT3DMS advection package.

2.4.1.1. Heat Transport in Model

To deal with the fact that the thermal front moves slower than the average flow velocity as the solids absorb heat, a thermal distribution coefficient K_{DT} is introduced in SEAWAT (Langevin, 2008a), which represents the thermal equilibrium between the fluid and the solid:

$$K_{DT}=\frac{c_s}{\rho_f c_f} \tag{2.15}$$

where ρ_f and c_f are the density and heat capacity of the fluid, respectively.

Following from that is the thermal retardation R, given as:

$$R=1+\frac{\rho_b}{\phi}K_{DT}\quad\text{with}\quad\rho_b=\rho_s(1-\phi) \tag{2.16}$$

with the bulk density ρ_b.

The thermal conduction term is implemented as the bulk thermal diffusivity D_T, which acts like a molecular diffusion coefficient in MT3DMS (Langevin, 2008a). How this is derived from the core measurements is outlined later in chapter 3.

$$D_T=\frac{\lambda_b}{\phi\rho_f c_f}\qquad\text{with}\qquad\lambda_b=\phi\lambda_f+(1-\phi)\lambda_s \tag{2.17}$$

λ_f and λ_s are the thermal conductivities of the fluid and solid phase, while λ_b is the bulk thermal conductivity of the sediment.

In the used molecular diffusion process in MT3DMS for representing heat transport, thermal conductivity is not temperature dependent. That is a limiting factor over larger temperature ranges and can influence the modeling outcome. This effect is quite low however as mentioned in before, and it is reasonable to neglect it and assume constant thermal properties for the temperature range simulated here (Langevin, 2008a).

2.4.1.2. Implementation of Variable Density and Viscosity

In newer versions, SEAWAT does account for variable density and viscosity though (Thorne et al., 2006). The relation of water viscosity μ_w and temperature T is given by this equation by Voss, 1984:

$$\mu_w(T)=2.394\cdot10^{-5}\cdot10^{\left(\frac{248.37}{T+133.15}\right)} \tag{2.18}$$

The density is linearly dependent on temperature in SEAWAT, using the reference density ρ_{ref} at ambient groundwater temperature and the minimum density ρ_{min} at the injection temperature (Beernink et al., 2024).

$$\rho_{ref}=1000-\frac{(T_{amb}-4)^2}{207} \tag{2.19}$$

$$\rho_{min} = 1000 - \frac{(T_{max} - 4)^2}{207} \tag{2.20}$$

The linear relation as it is used in SEAWAT then follows as $\rho_w(T)$:

$$\rho_w(T) = \frac{\rho_{ref} - \rho_{min}}{T_{amb} - T_{max}} \tag{2.21}$$

Both relations are shown in figure 2.7. There viscosity and density of water are displayed in relation to its temperature.

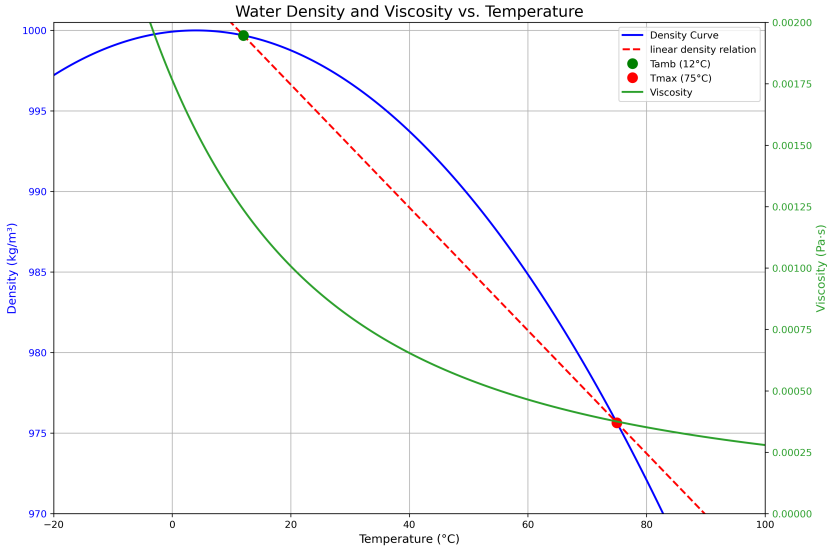

Figure 2.7: Change of viscosity and density of water with varying temperature. This visualizes the equations 2.18 for viscosity and the linear relation for varying density given in equation 2.21

SEAWAT was part of a benchmark study by Mindel et al., 2021, where it got compared to analytical and experimental results for modeling low enthalpy geothermal processes. The software executed all tests reliably, so it has been deemed as suitable to solve HT-ATES subsurface problems.

3

Methodology

3.1. Introduction

In the following sections the methodology for the laboratory measurements performed and for the setup of multiple numerical HT-ATES models is elaborated and described in detail. Also the available data is presented. A simplified flowchart for the laboratory procedure is displayed in the appendix A.1.

The samples are prepared and then measurements conducted with multiple devices which described in the first part. The goal for these procedures is the set-up of a property database for the Maassluis formation at the 4 wells cored. The measurements include hydraulic conductivity measurements on a core and plug scale, and thermal conductivity, diffusivity and heat capacity measurements on the plug scale. Additionally all plug samples are weighted in fully saturated and dried states, with a smaller fraction of them also subject to pycnometer density determination. An emphasis is put onto the DAPGEO-02 borehole, as there the most cores are available which leads to a more precise analysis of the results after data collection. The intention is to use these results and implement them in the later setup of a subsurface model to assess the impact of varying thermal properties.

In the second part the setup of a number of SEAWAT numerical underground models is presented. Model parameters are calculated and the grid discretization is outlined. A simple, 3 layer base case is introduced and an overview of the different scenarios that are consequently modeled is given. In these different scenarios the thermal properties of the aquifer and aquitard layers are varied, as well as the hydraulic conductivity in horizontal and vertical direction of the aquifer. Conclusively the output data that will be used for further analysis is shown.

3.2. Laboratory Testing

3.2.1. Available Cores & Data

The cores come from the 4 pilot boreholes in different locations in the Netherlands. Their locations are visualized in the figure 3.1 below. DAPGEO, Maasdijk and Rotterdam are relatively close together with no more than 26km between them. Leeuwarden on the other hand is located more than 150km away from the other locations.

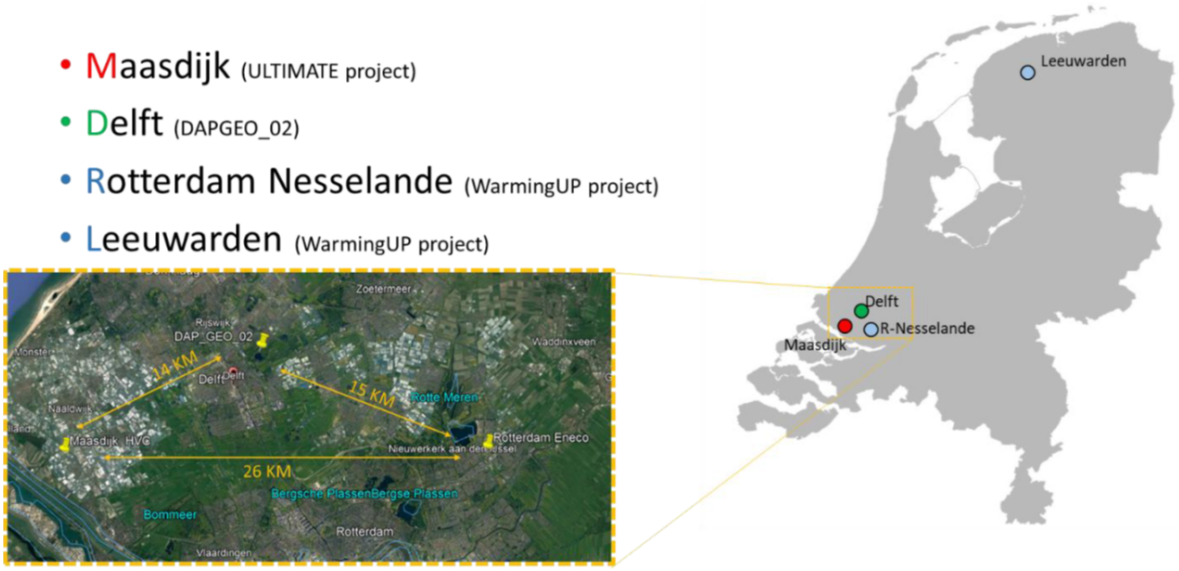

Figure 3.1: The locations of the 4 pilot wells within the Netherlands (from Beernink, unreleased)

Figure B.1 shows the well lithology logs with the depth of the Maassluis formation and promising sand bodies for ATES marked, based on their interpretation from during the drilling and logging process.

Also geophysical log data is available to different extent for the 4 wells. In this research Gamma Ray (GR) logs are used to potentially find correlations between measured properties and the GR readings at the corresponding depth the sample was taken from. For the DAPGEO well the (GR) log from the drilling campaign can be found in appendix B.3. A 50cm moving average visualization is chosen to even out noise, as the logging device performs measurements in 50cm intervals. The locations of the sampled cores within the borehole are marked within the GR plot. Gamma Ray logs available use API units as a measure of gamma radiation. Additionally, figure B.2 depicts the 50cm moving average Gamma Ray plots for all wells with the top and bottom of the Maassluis formation highlighted. It needs to be noted that the different locations cannot be compared to each other quantitatively, due to different logging systems used.

This data can be used to make potential correlations between GR data and thermal and hydraulic properties or spatially between the individual wells.

Overall the following samples could be taken from the 4 wells:

Table 3.1: Overview with number of core and plug samples and their depth range

borehole	cores samples	sample plugs	depth range [m bgl]
DAPGEO	8	43	115–226
Leeuwarden	2	6	255–284
Maasdijk	2	6	213–246
Rotterdam	3	13	93–184

3.2.1.1. Naming

The samples are named from a larger to smaller scale within the denotation. It starts with the borehole, followed by the core number and the plug, where a larger number connotes a larger depth. The two sides of a plug are named A and B, where side A always means the sharp side of the sample ring that was pushed into the sample.

3.2.2. Equipment

3.2.2.1. Thermal Properties using Hot Disk

To determine the three thermal properties thermal conductivity, diffusivity and heat capacity of each individual sample the Hot Disk Thermal Constants Analyser is used. It has the advantage of being non-destructive unlike the needle probe method for example, while also being able to measure a large range of thermal properties with high accuracy.

Working Principle

The device is using a measurement principle based on the so called Transient Plane Source (TPS) technique (Gustafsson, 1991). It uses a sensor in the shape of a double spiral (figure A.3). This spiral acts at the same time as a heat source to increase the sample temperature and as a thermometer to measure the increase of temperature over time. The spiral is embedded inside a Kapton cover to protect and electrically insulate it. This spiral is ideally placed between two halves of the sample. Alternatively a one-sided sample can also be used with an insulator on the other side, which is done here because of the unconsolidated sample material present. That is displayed exemplarily in figure 3.2. The styrofoam insulator is considered to be ideal.

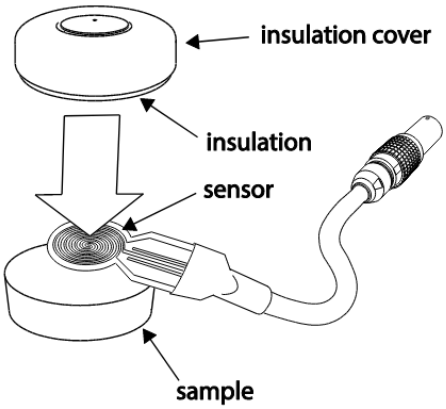

Figure 3.2: Sample setup for using a single sided sample (from Hot Disk AB, 2019)

Equation 3.1 describes the basic working principle of the TPS method. As the sensor heats up during a measurement, its electrical resistance $R(T)$ changes with that as well (Gustafsson, 1991):

$$R(T) = R_0[1 + \alpha\overline{\Delta T(\tau)}] \tag{3.1}$$

R_0 is the initial sensor resistance before heating, α is a temperature coefficient of resistivity and $\overline{\Delta T(\tau)}$ is the mean value of temperature change in the TPS element. Here $\tau = \sqrt{t/\theta}$, where t is the time since start of the transient measurement and θ is the so called characteristic time of the measurement. That is defined as $\theta = r^2/\alpha$ where r is the radius of the hot disk and α is the thermal diffusivity of the sample material.

Assuming zero contact resistance between sensor and sample material:

$$\overline{\Delta T(\tau)} = \frac{P_0}{\pi^{3/2} r\lambda} D(\tau) \tag{3.2}$$

Here P_0 is the total sensor power output, λ is the sample thermal conductivity and $D(\tau)$ is a dimensionless time-dependent function (Hot Disk AB, 2019).

By then plotting the temperature increase versus $D(\tau)$ a straight line is obtained with the slope being $\frac{P_0}{\pi^{3/2} r\lambda}$. As α is not known before, the final line is obtained iteratively. It therefore is possible to determine the conductivity as well as the diffusivity using just one transient recording Hot Disk AB, 2019).

The volumetric heat capacity is then calculated from the other two properties using the relation in equation 2.10. This is an advantage as the diffusivity can be used directly in the modeling software, where that is the input used for the calculation of the spread of heat in the storage aquifer (see chapter 3). While the transient plane source method has been used for testing saturated soils before (for example Yao and Likos, 2017) it is not widely applied and literature on sediment data obtained using that method is scarce.

Limitations

The Hot Disk is intended to be used for homogeneous samples. As in-situ samples are used in this study they show signs of heterogeneity and anisotropy. Because the temperature increase and therefore the measurements reach within the top 1 or 2cm of each sample the effect of heterogeneities within that are assumed to be negligible. In order to better reflect the difference even within one sample, both sides of each sample plug will be measured. One thing to be considered in that regard is the impact of heterogeneities (like small clay lenses) in very close proximity to the sensor. Here they can affect the results significantly. Because a certain pressure had to be applied to the styrofoam insulator to ensure proper contact between the sensor and the sample, some additional compaction may have affected the measurements. It also needs to be kept in mind that the idealized insulator will show a small degree of conduction in reality.

Alternative Ways of Determining Thermal Properties

Instead of directly measuring the thermal properties of sediments, which can be difficult depending on existing samples and boreholes in the research area, they can also be estimated using other methods. Different models exist for approximating and predicting thermal properties, and with that mostly the thermal conductivity, of saturated soils. Wang et al., 2021 reviewed different theoretical and (semi-)empirical models for predicting saturated soil thermal conductivity. While some of their reviewed theoretical models gave satisfactory results when applied to their dataset, they can only give estimates of thermal properties and lack the ability to reflect changes at smaller scale and finer resolution. Another option is the calculation of thermal properties using petrophysical well log data (for example Fuchs et al., 2015). Here relationships between changes in thermal properties of sediment and changes in well log properties are established to quantify the thermal properties. While this concept again can give good results it is limited by the resolution of the logging tools and does not properly reflect changes on smaller scales.

3.2.2.2. Core Scale Hydraulic Conductivity using a Falling Head Test

The hydraulic conductivity is first measured at the scale of the whole core. This is done using a self made apparatus using the Darcy principle and a falling head measurement. Water will be flowed through the fully saturated sediment, while it is still in its original liner. The rough schematic is shown in figure 3.3. A cylindrical water basin placed above the core is connected to a plastic cap at the bottom of the core, with a outflow tube connected to the top cap. Water is then flowed through the core while the head/pressure decrease is measured with a pressure gauge.

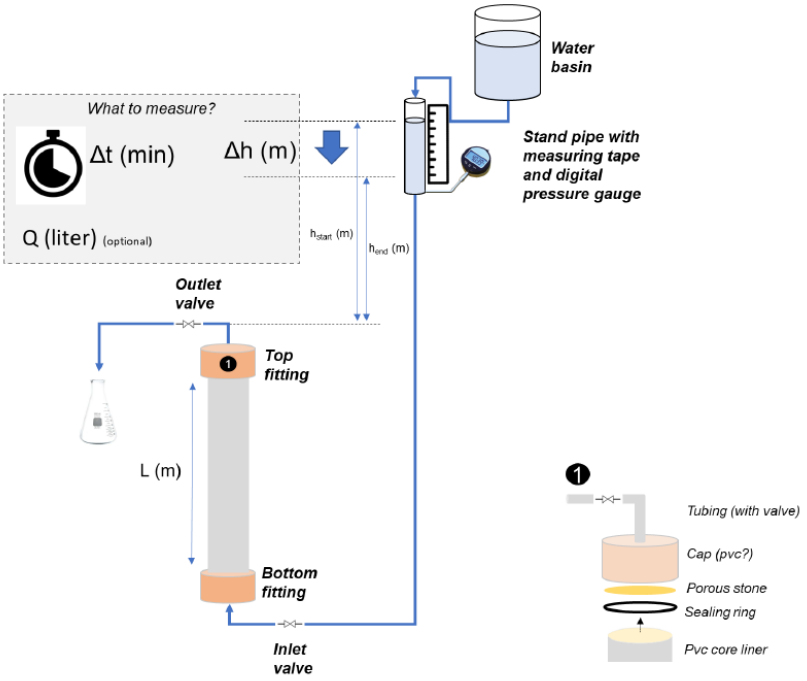

Figure 3.3: Basic working principle of the core scale falling head test (Illustration by Stijn Beernink, TU Delft)

The hydraulic conductivity through the core can then be calculated as:

$$k = \frac{a_{\text{in}} \times l}{A \times \Delta t} \times \ln\left(\frac{h_{t_1}}{h_{t_2}}\right) \tag{3.3}$$

with k the hydraulic conductivity of the sample, a_{in} the area of the inlet basin in m^2 and t the time for the head decrease. l describes the length of the sample in m and A the area of the sample in m^2. h_{t_1} is the starting head level of the inlet basin above the outlet, with h_{t_2} being the head level at the end of the measurement.

3.2.2.3. Plug Scale Hydraulic Conductivity with KSat Device

Additionally the hydraulic conductivity of smaller scale sample plugs taken from each core is measured with the METER KSat device. This device also uses a falling head measurement principle, with the simplified setup shown in figure 3.4.

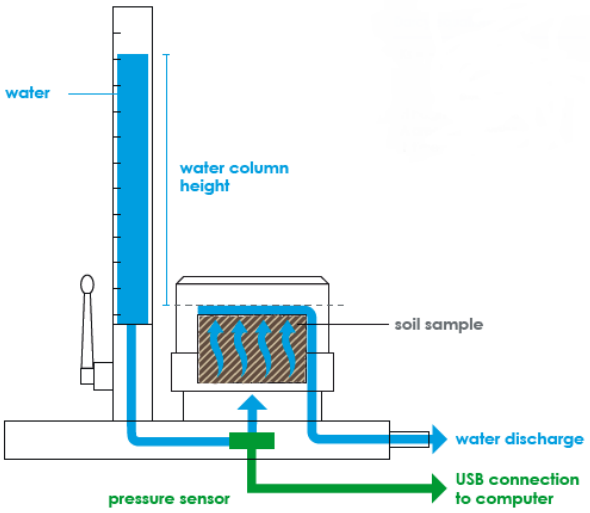

Figure 3.4: basic functioning of the KSat (from METER Group, 2012)

In its most basic principle the KSat works according to Darcy's Law (Darcy, 1856), with permeability K_s being:

$$K_s = \frac{LV}{HAt} \tag{3.4}$$

with L the sample length, V the volume of percolated water, H the height of the water column, A the area of the sample and t time. Also the volumetric flux q is:

$$q = -K_s \frac{H}{L} \tag{3.5}$$

and

$$q = \frac{A_{Bur}}{A_{Sample}} \cdot \frac{dH}{dt} \tag{3.6}$$

After equating the two equations 3.5 and 3.6, and integrating from $t = 0$ to t an exponential function can be fitted to the head timeseries observed ($H(t)$) to determine the coefficient b. Then the saturated hydraulic conductivity (KSat) is given by:

$$K_s = \frac{A_{Bur}}{A_{Sample}} \cdot L \cdot b \tag{3.7}$$

The KSat measurements get normalized for a specified reference temperature using equation 3.8:

$$\eta = 0.0007T^2 - 0.0531T + 1.764 \tag{3.8}$$

where η is the dynamic viscosity of water and T is the reference temperature.

Limitations

The KSat technique can give rise to a couple of problems with regards to the sediment fill in the sample rings. If the rings are not fully filled with sediment material, sediment could get flushed out, affecting the results and overestimating the hydraulic conductivity of the sediment. Although the sample rings have been handled with great care, another potential issue is (de)compaction during handling and the previously conducted hot disk measurements. Especially for clay samples full saturating could not be guaranteed due to time constraints, which might have had an influence on KSat measurements but will also affect the porosity measurements outlined in the next section.

3.2.3. Sampling

The cores used for this research were stored in sealed bags in a fridge at 7°C in the TU Delft Geoscience Department. These cores are in PVC pipes sealed with plastic caps and melted polymer. Up to 1.1m of sediment was recovered in the researched cores. As two different drilling and coring methods were used at the different pilot well locations, the cores from the DAPGEO-02 borehole have a diameter of 10cm while the cores from the other 3 locations have a diameter of 8cm. This leads to a slightly different approach in subsampling them, which is discussed later in this chapter. This also means that values for the Gamma Ray logs cannot be compared quantitatively due to the slightly different measuring approach in the different wells. The DAPGEO borehole was done with a flush drilling technique, while the other three boreholes were drilled with reverse circulation air lift drilling (Beernink, unreleased).

Before performing any measurements on the cores a thorough pre-selection had to be made. This selection is largely based on the available CT-scans (Vardon et al., 2023) that were taken of all cores after the cores were obtained. These scans gave a first insight into the probable content of each core and higher density sections or layers visible in the core showed likely clay rich sediments. The goal was to always get an undisturbed section from each core to do measurements which best reflected actual subsurface conditions with the least possible error introduced. Therefore every CT-scan needed to be evaluated regarding the expected sediment content and any disturbance which might be present due to the drilling or coring process. Because of the relatively high pressure at the coring depths of more than 100m for all but one core, it is not expected that the soil got compacted further as a result of the coring and subsampling process.

Several cores for all 4 boreholes are deemed unusable for further investigation during that process. This is mainly due to cores being not fully filled, or mostly filled with rubble as a result of the coring procedure. An example of that is shown in core MSD-03 in figure A.2a. Other cores were fully clay filled, which led to them being unusable for Kv measurements and therefore being excluded from the measuring campaign as well. Other reasons for not selecting certain cores were large, clearly visible cracks at the outside of the cores along the PVC pipes (like for example in core DAPGEO-02-C14 in figure A.2b), as this would have a large impact and lead to false hydraulic conductivity measurements. Here it was important to differentiate the orientation of cracks or low density layers. An orientation perpendicular to the later flow through the core during Kv measurements is expected to have no significant impact on the hydraulic conductivity, while the mentioned cracks parallel to the flow direction have a strong influence.

Generally the sediments expected in the cores are medium coarse to fine sand, silt and clay, with some shells present as based on the geology of the formation discussed in 2. In the table (A.2) an overview is given of all cores that were sampled and used for further measurements. This includes 8 cores from the well DAPGEO-02, 2 cores from LW, 2 cores from MSD and 3 cores from RD. Table A.1 shows the orientation of each sample plug taken from the cores.

Figure 3.5: Sawing off the top of a sediment core along the marking

From the CT-scans an interval is determined which is usable for measurements with the selected cores. Especially the rubble mostly cumulated at the top of the cores and non-filled parts have to be removed. The good interval is marked on each core before the top and bottom of each core are sawed off in the next step (figure 3.5), for which a band saw is used. The 2 sides of the remaining core are subsequently covered with PVC lids and taped sealed.

3.2.4. Laboratory Campaign

3.2.4.1. Core Scale Hydraulic Conductivity Measurements

The next step is performing a falling head tests over the entire core length. For this a self-made device in the TU Delft Geoscience lab is used, shown in image 3.6. The process is based on the falling head working principle shortly mentioned in chapter 2.

Figure 3.6: Kv falling head test setup

For this full saturation of the sediment cores is required so tap water is added to the sample until fully saturated before fixing the core in the test apparatus. Using sufficient water head level the pressure decrease across the core length as a result of the decreasing head height is measured. This is done for at least 5 minutes and repeated 2 times for lower conductive cores and 3 to 4 times for higher conductivity cores to average out multiple measurements. During the measurements samples of core fluid are also taken from each core for potential later analysis.

For overall four cores the cores were sawed into 2 sections after the first falling head test runs. That was done to check the influence of suspected smaller clay layers visible in the CT-scan. For example DAPGEO-02-C6 showed a very low conductivity of below the measurable cutoff of 0.1m/d, so a division of it into sections gave the possibility to measure the hydraulic conductivity of the core section that was not interveined by a clay layer.

Potential errors arise from the fact that the measurements were carried out at room temperature which fluctuated and not normalized for a specific temperature. As this was done for the KSat measurements, the core scale Kv results could show overestimated hydraulic conductivity values when compared to the KSat results, although that impact is expected to be marginal.

After successful completion of the falling head measurements the two core sides are again closed with a lid and then prepared for subsampling. This is done differently for the 10cm diameter cores from the DAPGEO-02 well and the 8cm diameter cores from the other three wells. For both variants the PVC pipes are cut with a table saw in a one-to-two ratio along the core length. The two lids are cut using a Dremel.

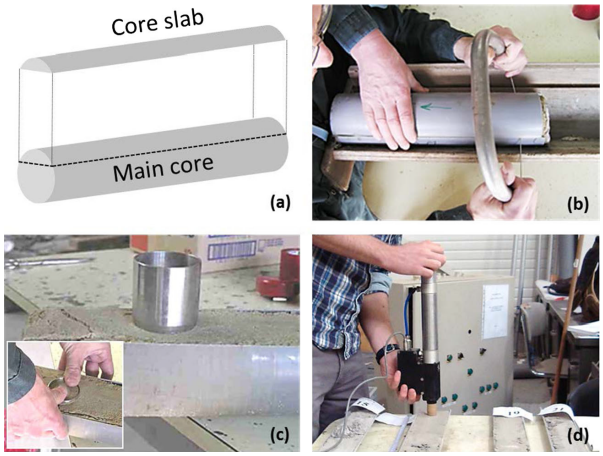

Figure 3.7: procedure of slicing open the core (image from Rogiers et al., 2014). Image (d) shows measurements with a air permeameter, which is not used here

The 10cm cores are then horizontally sliced with a wire saw, which gives a archiving half (AH) to be stored and used for further geological description and the bigger working half (WH) from which the sample plugs are taken. The slicing is done based on a process by Rogiers et al., 2014 shown in figure 3.7. Because the wet sediment is quite cohesive this works without significantly disturbing the sediment.

For the thinner cores from Maasdijk, Leeuwarden and Rotterdam only the PVC liner is cut with the table saw and Dremel before the smaller pipe part is taken off carefully. Here no archive half can be taken as the whole core diameter is needed to take samples with the available sample rings. A problem of this method is, that it cannot be avoided that some sediment sticks to the PVC when taking it off, potentially limiting where subsamples can be taken afterwards in undisturbed sediment.

For both diameter cores the slices are then photographed and a decision is made on where vertical and horizontal subsample plugs should be taken. The aim was to sample representative smaller scale parts of each core. Hereby plugs were taken from a certain distance from each other and different lithology where apparent to reflect the heterogeneity within the core. An example of that for one of the DAPGEO cores can be found in the appendix (A.4). It was practically only possible to take vertical subsamples from the top and bottom ends of each core (section). Therefore for most of the cores vertical samples were taken from both ends. The pictures of the cores in the appendix show the relative location and orientation of every plug in its core.

The sampling is done by pressing the 100ml rings (5cm diameter), with the slimmer cutting edge first, into the sediment by hand and then taking out the ring with as little disturbance as possible. Between 2 and 8 plugs are taken per core. A list of all plugs is shown in table A.1. Overall 68 different core plugs were taken, 30 of those are vertical, while 38 are of horizontal orientation.

The plugs rings are closed with lids and stored in labeled plastic bags. The cores are wrapped in plastic foil to reduce oxidation, labeled and stored for further examination in the future.

3.2.4.2. Hot Disk Thermal Property Measurements

After completion of sample plugs preparation from the four boreholes the in depth lab work on the plug scale samples is carried out. The measurements of thermal properties with the Hot Disk and of hydraulic conductivity with the KSat devices are performed in a climate room with constant room temperature of 18°C, where the sample plugs are photographed and fully resaturated. They are then stored until they reach thermal equilibrium with the ambient temperature before all measurements.

To the best of current knowledge the hot disk method has not extensively been applied in published research on fully saturated unconsolidated sediments. Therefore the best procedure and accuracy of

this measurement technique was unestablished prior to the experiments and had to be determined as the experiments were carried out.

The first device used is the Hot disk thermal property analyzer already discussed in chapter 2. In order to achieve accurate results it is essential that the samples are measured under fully saturated conditions. As the device is unable to measure the thermal properties throughout the whole sample but only within a certain probing depth of about 10 to 15mm, it is feasible to carry out measurements on both sides of the sample plug. Overall 3 measurements are performed on each side of every sample and then averaged out.

The measuring procedure is performed for each set of 3 measurements as follows: The lid of one side of the sample ring at thermal equilibrium is removed, while making sure that the other side is fully sealed and the sample remains saturated. The hot disk sensor is placed right in the middle on top of the sample surface. The styrofoam insulator with a diameter slightly smaller than that of the sample ring is placed on top and screwed on using the hot disk aperture to ensure full contact between sensor, sample and insulator. Now again at least 10 minutes of time is given to the whole setup to reach equilibrium. The whole setup can be seen in figure 3.8.

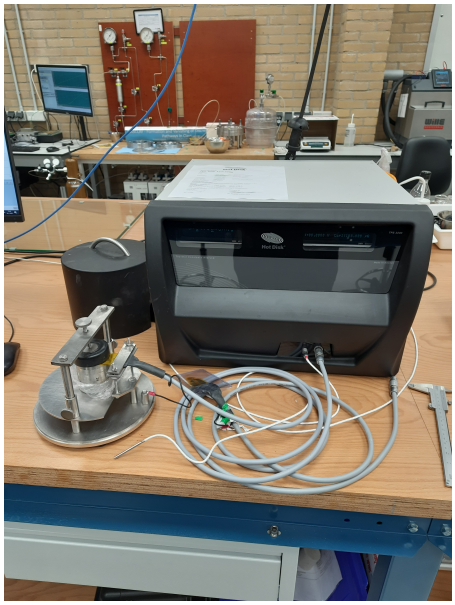

Figure 3.8: Hot disk device setup showing plug screwed in place

Then a set of 3 measurements is executed for that particular sample side. The device and measurement settings used can be found in the table A.3 in the appendix. If deemed necessary after one of the measurements, the settings (measuring time and/or power) are adjusted to keep hot disk parameters like the probing depth, total temperature increase and total to characteristic time within their required limits. After the measurement the outputs in the hot disk software are examined for any prominent divergence in output thermal property results, but also high residual errors or unusual shapes of the measured temperature increase transient curve. The measurements would then be repeated until 3 measurements which satisfy all conditions were recorded and the same is then done for the other side of the sample plug.

3.2.4.3. KSat Plug Scale Hydraulic Conductivity Measurements

After the hot disk measurements for each sample are completed successfully they are subject to hydraulic conductivity measurements with the KSat device in the next step. Detailed background on the KSat and its measurement principles is covered in chapter 2.

Before starting any measurements it's required to calibrate the KSat offset. This is done by leveling

the water to the exact height of the top of the measurement chamber and then using the calibration in the device software. For getting the sample ring ready in the measurement device one lid is taken off the sample ring again and the adapter for small 5cm sample rings provided with the KSat is put onto the lower side of the ring (see example in appendix A.6). For naming convention the lower side is always the side that was not pushed into the core when sampling (with the thicker ring). After again dripping water on top of the sediment to oversaturate it and to make sure there is no air trapped, the water saturated lower porous plate is put on. The sample is turned around and it is proceeded likewise with the upper side and the fitting upper porous plate. This whole part is then placed on top of the water bubble with the valve opened to avoid any pressure buildups potentially damaging the sensitive sensor. With low pressure head some water is flushed into the sensor to again avoid any air bubbles forming and the big blue lid is screwed on to fix the sample in place. Afterwards the measurements are started with 5cm of pressure head. Figure 3.9 shows the setup during a measurement run.

Figure 3.9: KSat device setup during measurement

Inside the software the device and sample parameters need to be set accordingly, paying attention to choose the 5cm ring size and porous upper plate setting. General settings used are shown in table A.4 in the appendix.

For higher conductive sandy samples three measurements are performed while for silty to clayey samples with very slow head decrease only 2 measurements are performed for time reasons. The pressure decrease is plotted automatically in the KSat software and a curve is fitted to it. The RMS error of the fitted curve is displayed and indicates potential issues with the measurements. Ideally this value is greater than 0.999 but in this study values above 0.99 were considered as sufficient. If this was not achieved the setup was checked for proper sealing and measurement runs were repeated.

It needs to be noted that the results of KSat measurements are automatically normalized to reflect the hydraulic conductivity at 10°C temperature. While this counters any possible fluctuations in room temperature between different KSat measurements it makes comparison to the Kv measurements more difficult. As these were not done in a climate-controlled room, fluctuations were bigger and the cores were not given time to reach temperature equilibrium within that room.

3.2.4.4. Sample Drying & Pycnometer Measurements

Following the hydraulic conductivity measurements, each sample is taken out of the ring and put into a sample bucket at full saturation. To get the actual sample volume, if the sample ring is not fully filled due to losses during handling of the plugs or potential compaction in the KSat, the missing fill height is

measured. An example picture of two dried samples can be found in appendix A.5. All the saturated samples are then weighted and kept in an oven at 105°C for 24 hours to reach their fully dried state. They are then again weighted to determine the dry weight. The dried samples are then stored in labeled plastic bags for any future research on them. Further a selection of 11 samples was made which are to be measured in a pycnometer to accurately determine their actual dry density (see list in the results 4). The selection was done in a way to reflect a range of samples from different well locations, different depths and different grain sizes. Only a small number of samples were selected due to time constraints and the duration of pycnometer measurements.

For the pycnometer measurements the samples are required to be present in a powdery state, so they had to be crushed where necessary after the drying. The powder is then filled into the medium sized sample container, like in figure 3.10, in which their weight is determined as a required parameter for the measurements. The container is placed in the measurement chamber which is then closed, their weight entered and the measurement run is performed.

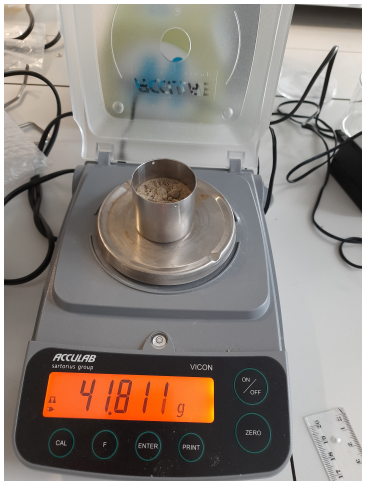

Figure 3.10: RD-05-P1 sample weighing for pycnometer measurement

The exact measuring parameters can be found in table A.5 in the appendix. For these samples an average of three measurements is taken.

After the laboratory measurements all sample bags are stored again in the TU Delft core storage room together with the cores the samples had been taken from.

3.2.5. Data Processing

The following table 3.2 summarizes all properties that were measured in the lab campaign:

Table 3.2: Overview of all properties that were measured in the lab and the scale of sample they were performed on

Property:	**Measured on:**
Falling head Kv	Core
Ksat hydraulic conductivity	Plug
Hot disk thermal cond. & diffusivity, Vol. heat capacity	Plug (2-sided)
Wet & dry weight, plug fill volume	Plug
Pycnometer density	Plug (few samples)

All results have been gathered in one database file - grouped per well. Apart from the results from the lab experiments performed, additionally gamma ray values from the logging campaigns are included in

the dataset for the depth of each core. Descriptions of each core and plug are also included. This is how the samples were described during the subsampling process after slicing open the cores. Additionally the description from the drilling cuttings and the lithological classification from each drilling report, based on the cuttings and logging data, are included. That database will likely be made available later in time.

The core plugs are assigned one of four basic lithological classes. This is done separately per plug side, so one plug can have two different classifications. In an international standard grain size classification is done according to ISO14688-1, 2017. There is clear boundaries for the distinction of each grain size class. However, in this research grain sizes are not measured and the classification is done by eye, to roughly group the samples into one of the four classes.

These classes are:

- **1: clay**
- **2: silt to very fine sand**
- **3: fine sand**
- **4: medium coarse sand**

The classification has been conducted based on the majority of the sediment at the surface of each plug side. While this method doesn't necessarily reflect the average lithology of each sample plug, it gives the most replicable data for the Hot Disk thermal property measurements which are the main focus of this research.

Porosity was calculated based on the density measured with the pycnometer for samples where this was determined. Otherwise porosity calculations are performed for all samples based on the weight using the difference between dry and wet weights, the sample volume inside the sample ring and the density of water.

In the results in chapter 4 emphasis is put onto the DAPGEO-02 borehole results. The larger amount of data makes it easier to visualize the data and therefore to draw conclusions or any visible trend from it. The other 3 boreholes are also shown briefly and compared, but for them the focus is on wether it is possible to see any correlations or spatial difference between the different locations.

The most important results of the lab measurements are the value ranges for thermal conductivity of aquitard and aquifer sediments respectively. These results are fed into the SEAWAT models and provide the basis for that section of this study. It needs to be noted that no cores were available from the sealing aquitard above the Maassluis formation. That means the actual properties of the sealing clay layer of the Waalre formation are unknown, but instead based on properties of clays measured in the Maassluis formation. This likely reflects the thermal properties of the Waalre sediments sufficiently well.

3.3. Simulations

To evaluate the impact of the varying measured thermal properties on the recovery efficiency as well as the thermal impact on adjacent layers of HT-ATES systems several underground models are setup and simulated. These models incorporate some of the thermal properties of the soils presented in chapter 4. The average values of thermal conductivity and the maximum and minimum values for the clay/aquitard and sand/aquifer are used to assess the impact resulting from their uncertainty.

3.3.1. Model Setup

With the use of equation 2.2 the thermal radius of a system with the storage properties used here was calculated to be 50m. This will be used as the extent of the heat bubbles for modeling cases 0 and 1 later on.

The subsurface layer model used represents dummy systems of the Maassluis formation and is made up of three distinct layers, one aquifer and two confining aquitards below and above. The aquifer representing Maassluis formation sands has a constant thickness of 50m throughout the model, the aquitards are 100m thick each and are assumed to be present as a sealing layer throughout the whole model. This setup is shown in the following figure 3.11:

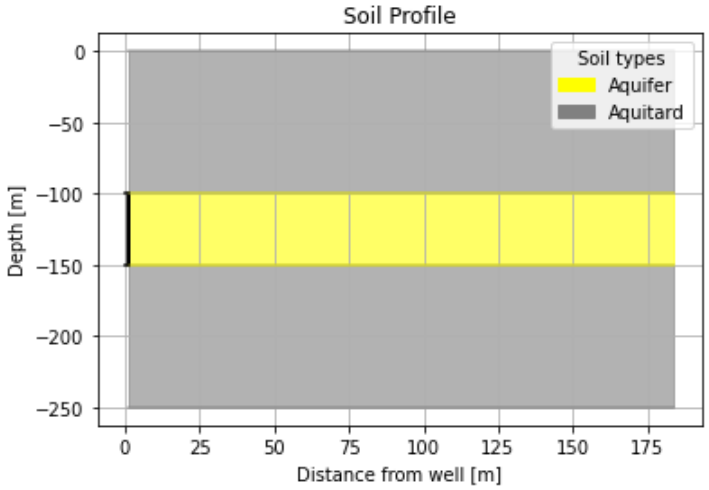

Figure 3.11: Simplified layer model used for simulations

Additionally the vertical extends, hydraulic conductivities and porosity of the layers for the base case are displayed in table 3.3. The ambient groundwater temperature is 12°C and the porosity of aquifer and aquitard is 0.35 in all models.

The following assumptions and simplifications are made for the models:

- The aquifer and aquitard layers are fully saturated and each layer is homogeneous.
- Injection and extraction volumes are equal over each yearly cycle. The injection temperature remains constant.
- The well penetrates the aquifer fully and is screened over its entire length.
- The thermal properties of the layers are isotropic, while the hydraulic conductivity is not.
- Density and viscosity of the water in the system are temperature dependent, while the thermal properties of it are not.
- No groundwater flow is present in the area.

Table 3.3: Dimensions and hydrogeological Properties of the model layers
** = conductivity values for base case*

Layer	Top [m]	Bot [m]	Kh [m/d]	Kv [m/d]	ϕ
1	0	-100	0.025	0.0025	0.35
2	-100	-150	7.5*	0.75*	0.35
3	-150	-250	0.025	0.0025	0.35

3.3.1.1. Parameter Calculation

Some model property calculations need to be made from the (average) lab results in order to reflect these parameters in the model.

The specific heat capacity of the solid fraction c_s can be calculated from the measured bulk volumetric heat capacity $C_{v,\text{bulk}}$, the solid density ρ_s, porosity ϕ and the water volumetric heat capacity $C_{v,\text{water}}$:

$$c_s = \frac{c_{v,\text{bulk}} - \phi\, c_{v,\text{water}}}{(1-\phi)\,\rho_s} \tag{3.9}$$

For this study a value of $710 J/kg/K$ is used, which is the specific heat capacity of quartz and approximated quite well by the average lab data.

The bulk density of modeled sediments ρ_b is calculated using the average measured (aquifer) solid density ρ_s of $2650 kg/m^3$, the porosity and density of water ρ_f:

$$\rho_b = \rho_s \cdot (1-\phi) + \rho_f \cdot \phi = 2072.5 kg/m^3 \tag{3.10}$$

To input the thermal diffusivity in the form of equation 2.17, the measured thermal conductivities are converted for SEAWAT application into aquifer $D_{T_{aq}}$ and aquitard $D_{T_{aqt}}$ diffusivity using the relations

$$D_{T_{aq}} = \lambda_{aq}/(\phi \cdot \rho_f \cdot C_f) \cdot 24 \cdot 3600 \tag{3.11}$$

and

$$D_{T_{aqt}} = \lambda_{aqt}/(\phi \cdot \rho_f \cdot C_f) \cdot 24 \cdot 3600 \tag{3.12}$$

where λ_{aq} is the thermal conductivity of the aquifer and λ_{aqt} the thermal conductivity of the aquitard. Only the fluid density and specific heat capacity are used because the solid part is dealt with separately by the thermal distribution coefficient K_{dist}, which accounts for thermal retardation:

$$K_{dist} = C_s/(\rho_f \cdot C_f) = 1.7e-4 \tag{3.13}$$

The solid specific heat capacity, thermal distribution coefficient and bulk density are kept constant throughout the model grid and time.

3.3.1.2. Grid and Time Discretization

In this study an axisymmetrical model grid is used to simulate the heat and fluid flow in the modeled ATES systems.

For a system with just one well modeled and homogeneous layer properties, the axisymmetric grid is a good option. This reduces computational efforts for the given system compared to 3-dimensional cartesian grids, as it reduces it to many layers and columns, but only one row (see figure 3.12), while still keeping high accuracy (Vandenbohede et al., 2014). The SEAWAT code is modified to account for the increase in flow area with growing distance away from the well in the center of the model and correcting for cell properties with increasing distance r from the well (Langevin, 2008b). In this case the flow into or out of the well is distributed evenly across all cells along the well screen length.

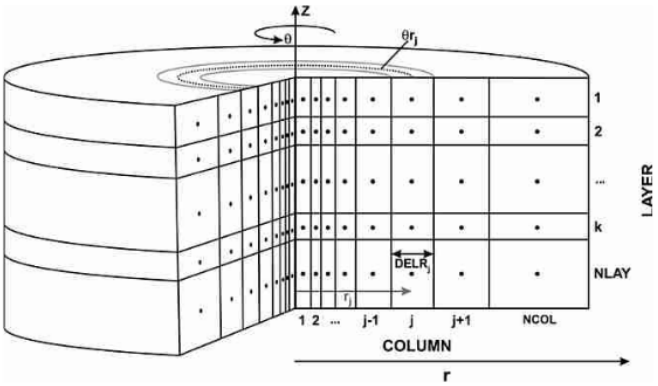

Figure 3.12: Schematic of an axially symmetric model grid (from Langevin, 2008b)

The axisymmetrical SEAWAT flow model has shown good agreement in test problems with analytical and other numerical solutions for solute (Langevin, 2008b) and heat transport (Vandenbohede et al., 2014).

Regarding the grid for models simulated here, grid cells have a vertical discretization of 0.5m and a horizontal width of 1m for the first 100 cells closest to the well (figure 3.13). Horizontally further away from that, the cell size grows logarithmically until the model boundary 500m away from the well.

Timesteps are 30 days (one month) long each, with every system simulated for a overall runtime of 20 years. While ATES system often have a longer lifetime this is enough to see relevant effects over time on system performance and thermal impact, as the differences between years become very small towards the end of that time period.

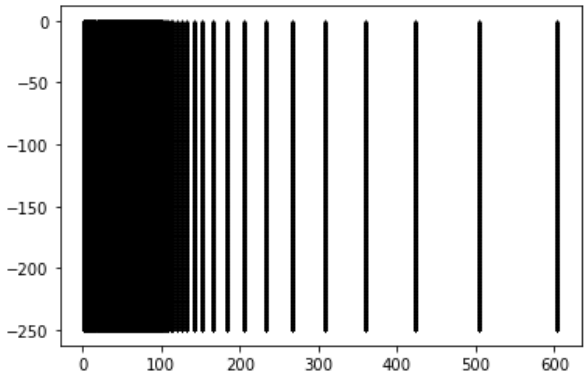

Figure 3.13: Horizontal discretization of the axisymmetric grid. In the closest 100m to the well one cell is 1m wide.

3.3.1.3. Model Parameters

An overview of fixed model parameters is given in the following table 3.4:

Table 3.4: Fixed parameters for all HT-ATES modeling scenarios

System Parameter	Value
Runtime [years]	20
Aquitard layer thickness [m]	100
Aquifer thickness [m]	50
Storage volume [m^3/year]	250000
Injection cycle	sine
Injection Temperature [°C]	75
Ambient Temperature [°C]	12
Porosity	0.35
Kv aquitard [m/d]	0.005
Kh aquitard [m/d]	0.025
Dispersivity [m]	0.25
Transv. dispersivity [m]	0.05
Trans. dispersivity [m]	0.005
Solid density [kg/m^3]	2650
Fluid density [kg/m^3]	1000
Spec. heat capacity solid [J/kg/K]	710
Spec. heat capacity fluid [J/kg/K]	4183
Therm. Distribution coeff.	1.70E-04

The varied thermal properties are presented in chapter 4, as a result of the laboratory measurements.

3.3.2. Base Case

The base model is designed to check for the sensitivity of varying thermal properties in different operating conditions. For that purpose the operational parameters and most of the hydrogeological properties have fixed values in the simulations to isolate the changes in thermal properties and evaluate only their impact. In some later model realizations the hydraulic properties are varied so assess the impact of the therefore changing flow on the impact of varied thermal properties.

The dummy system simulated here is based on a potential HT-ATES at the TU Delft campus to store the excess heat produced by the existing geothermal doublet. Therefore most of the parameters used in the model are derived from the Feasibility study for HT-ATES at the TU Delft campus (Bloemendal et al., 2020). The parameters in that study are based on the heat demand and availability from the geothermal doublet present that is used as the heat source. No cut off temperature is applied, water is injected at 75°C evenly through the well which is screened in the whole aquifer section. There is constant injection and extraction, with an overall volumetric balance over each year and storage cycle. The overall storage volume of $1,000,000m^3$ is required per year. Only one hot well is modeled. The volume that is required for storage as proposed by the feasibility study is in that case stored using 4 wells. In the models here therefore only one fourth ($250,000m^3$) of that storage volume per year is required. That volume is stored in a cyclic yearly pattern, following a cosine curve. The simulations start in summer, at the highest point of injection flow rate.

The simplification to only model one hot well is made, because the hot well is where the strong buoyancy flow occurs in HT-ATES systems. This also means that well interaction effects are ignored here. The feasibility study originally proposed design parameters for a HT-ATES system operating either in the Maassluis or the deeper Ommelanden formation. Here only the Maassluis formation is subject to discussion.

The hydraulic conductivity set for the models is based on values from the REGIS II dutch subsurface database synthetic borehole at the proposed location on the TU Delft campus (TNO–GDN, 2024). The reason for using these values, and not the ones measured in the laboratory experiments, is the scale dependency of the hydraulic conductivity. The range given in the horizontal hydraulic conductivity in REGIS for Maassluis aquifer sands is used to setup models which vary from the lower given value

of $5m/d$, to the middle value of $7.5m/d$ for the base case and the larger value of $10m/d$. For the sealing clay layer the vertical hydraulic conductivity range is given in REGIS II. Here a middle value of $0.0025m/d$ is used. The corresponding horizontal or vertical conductivity values are determined using the anisotropy factor. The hydraulic anisotropy is set to 10, which as mentioned in chapter 2 is a reasonable estimation. The actual value could vary quite a bit and is subject to calibration. As this is fixed here for all but one case, and the main research parameter are the thermal properties, it is good for comparison to leave it at that value which is also used in many other models.

At the locations in Rotterdam (F. Jansen, Oerlemans, et al., 2023) and Leeuwarden (F. Jansen, van Veen, et al., 2023) pumping tests were performed in the pilot wells. They gave results in the same order of magnitude as used for the dummy system here of around $10m/d$, confirming the values from the REGIS model.

3.3.3. Modeling Scenarios

The models are divided in 6 main cases, all shown in the framework table 3.6 Within each case a minimum of 5 scenarios with different thermal conductivities are modeled. This includes:

- average conductivity for aquifer and aquitard
- maximum aquifer and aquitard conductivity
- maximum aquifer, minimum aquitard conductivity
- minimum aquifer, maximum aquitard conductivity
- minimum aquifer and aquitard conductivity

The first two cases 0 and 1 do not include any injection/extraction or density-driven flow and therefore present solely conductive cases. These are used to assess the impact of varied thermal properties on that and represent a scenario with maximum conduction (case 0), where the heat bubble is applied as a boundary condition and therefore constantly conducts out heat at the injection temperature of 75°C. In case 1 on the other hand the model starts out with a 75°C warm bubble in the aquifer, there is no resupply of heat though.

Case 2 introduces the sine shaped yearly injection/extraction cycle. In case 3 density and viscosity effects are considered, leading to buoyancy flow. Case 4 simulates varied hydraulic properties of the aquifer (see table 3.5), but again without buoyancy flow. In case 5 varying hydraulic conductivities are simulated, this time with buoyancy flow enabled. Additionally here scenarios are run with an adjusted anisotropy ratio of 5 instead of 10 like in all other models.

Varied Hydraulic Properties	Kh [m/d]	Kv [m/d]
Hydraulic conductivity aquitard	0.025	0.0025
Standard values conductivity aquifer	7.5	0.75
Lower aquifer conductivity	5	0.5
Higher aquifer conductivity	10	1
Lower anisotropy ratio aquifer (5)	7.5	1.5

Table 3.5: Varied Aquifer Hydraulic Conductivity for Cases 4 and 5

3.3.3.1. Output Data

For each model monitoring data is saved for later analysis. For every scenario the underground temperature distribution is plotted after injection and after extraction for year 3, 5, 10 and 20 of the run. Also the injected and extracted volumes and temperatures are saved across the well screen to be able to calculate the recovery efficiency of the system.

When plotting temperature plumes, the state of maximum plume extend is usually plotted. This is the case after injection, just when extraction of the water starts again. Those points in time are marked on

the following figure 3.14. At these points in the cycle the plume size is at its maximum. That corresponds to the 4th month in the modeling cycle, while the point of the smallest thermal plume is after extraction in the 10th month.

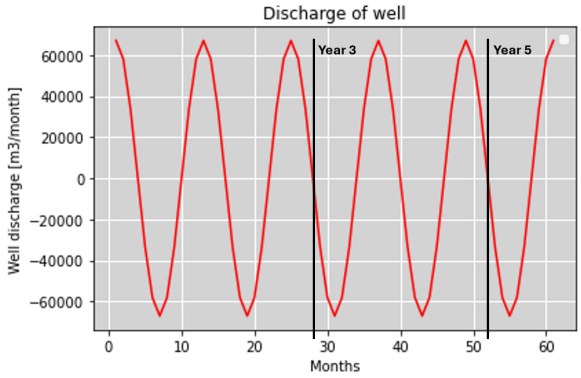

Figure 3.14: Discharge of the well over the first 5 years. Sampled points of maximum plume size after injection in cycle 3 and 5 are highlighted.

Along the well at location $r = 0m$ and at the calculated thermal radius of $R_{th} = 50m$ vertical monitoring lines are set up. At the top, right in the middle and at the bottom of the aquifer horizontal monitoring lines are set up. These location are also shown in figure 3.15 and can be used for plotting and analysis of the model results. These could give insights into the development of the thermal plumes of the different models and the extend of it into the confining layers.

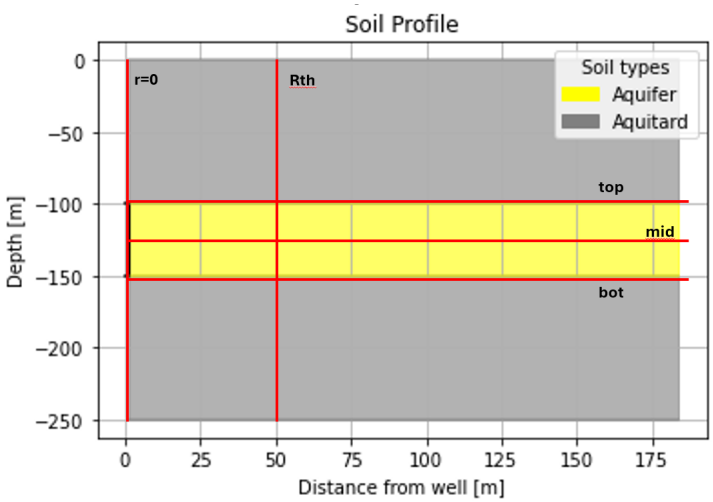

Figure 3.15: Positions of the monitoring lines within each model for later assessment of the impact of changing thermal properties

Table 3.6: Framework table of all modeling cases, and wether an injection/extraction cycle, buoyancy flow, or varied hydraulic conductivity are included (yes (Y) or no (N))

Case	Inj/Ext Cycle	Buoyancy Flow	Varying Hydraulic Conductivity	Models per Case	Description
0	N	N	N	5	Static cylinder (constant heat)
1	N	N	N	5	Static cylinder (one time heat input)
2	Y	N	N	5	
3	Y	Y	N	5	
4	Y	N	Y	10	Lower/higher hydraulic cond.
5	Y	Y	Y	15	Lower/higher hydraulic cond., lower anisotropy ratio

4

Results

The results are divided in the two main sections of this research. First the data that has been gathered following the lab measurements with descriptions of the sampled cores and properties measured is presented. Secondly the outcomes of the subsequently modeled HT-ATES systems are shown in regards to achieved recovery efficiencies and the impact of the resulting thermal plumes.

4.1. Results of Laboratory Work

Each sample has been described, classified into a grain size category and measured. From these results the distribution and range of properties for each of the classes and the different borehole locations can be concluded. This will give an overview of absolute values and their variability for hydraulic and thermal Maassluis sediment properties.

In the first section, the hydraulic and thermal properties of DAPGEO core and plug samples are presented. Correlations between those results and the respective classes assigned to each sample are carried out in section 4.2. There the results are also correlated with the other well locations.

4.1.1. Description and Classification of Samples

Overall the grain size ranges from clay to medium fine sand which aligns with what was expected from the cuttings and logging data gathered during the drilling. The respective well logs of the four locations can be found in the appendix B.1. For the DAPGEO borehole as the main research focus, the Gamma Ray plot in the appendix B.3 gives an overview of the depth and the GR readings of the individual cores sampled from within that borehole.

Shells are present in some parts of the Maassluis formation to a significant amount. They are mostly small fragments of up to 0.5cm in size. Rarely also some organic, potentially wooden, fragments can be seen in the samples. Clear coarsening or fining trends within single cores can not be observed. Some thicker clay layers of multiple centimeters occur. The clay is mostly only present in the form of little lenses or patches, that don't stretch out across the whole borehole width. The small size of the cores in horizontal direction makes it difficult to infer the spatial extent of these clay lenses but except for the thicker layers, visible at the core scale, they seem to be quite localized.

The general core description done in this work does not always align well with the cuttings based description. That is possible though, as the cuttings don't reflect a small scale in-situ description and can vary when there is thinner layers with different grain sizes in close proximity. The actual core descriptions are the more accurate lithology in that case. The various samples from within one core

generally show similar grain sizes with no abrupt changes. They do vary though even between the two sides of one sample plug, showing some smaller scale variability. Small clay lenses in the centimeter scale lead to for example one side of a plug being classified as clay, while the other side is classified as fine sand. The figure below highlights the distribution and variance of sample classes across a well.

Because the grain size classification in this study was done solely by visually assessing the sample plugs and choosing the most dominant grain size, the classification is not entirely accurate but rather should be seen as a good estimation to infer overall trends in the results across depths and wells. It is noteworthy that even though for example medium coarse sand is the dominant grain size, small patches of clay can have a large effect on the results, especially when they are located right underneath the sensor during the hot disk measurements.

4.1.2. Hydraulic Conductivity

In this section the results of the DAPGEO hydraulic measurement campaign are presented. This includes the core scale Kv measurements as well as the plug scale measurements using the KSat device. Table 4.1 shows the minimum, maximum and average hydraulic conductivities for the individual classes of all DAPGEO-02 samples, with classes 2, 3 and 4 grouped together as sand, or aquifer. Clay samples (class 1) give average hydraulic conductivities of 0.38m/d for the plug measurements, while for the sand samples the average conductivity is 4.48m/d

Table 4.1: DAPGEO hydraulic conductivity [m/d] statistics for aquitard and aquifer samples

	min	**max**	**avg**
aquitard (class 1)	0.01	1.36	**0.38**
aquifer (classes 2–4)	0.02	19.77	**4.48**

Most core plugs exhibit hydraulic conductivities below 4m/d as the distribution of results in figure 4.1 shows, although some highly conductive samples with conductivities between 12 and 20m/d are also present.

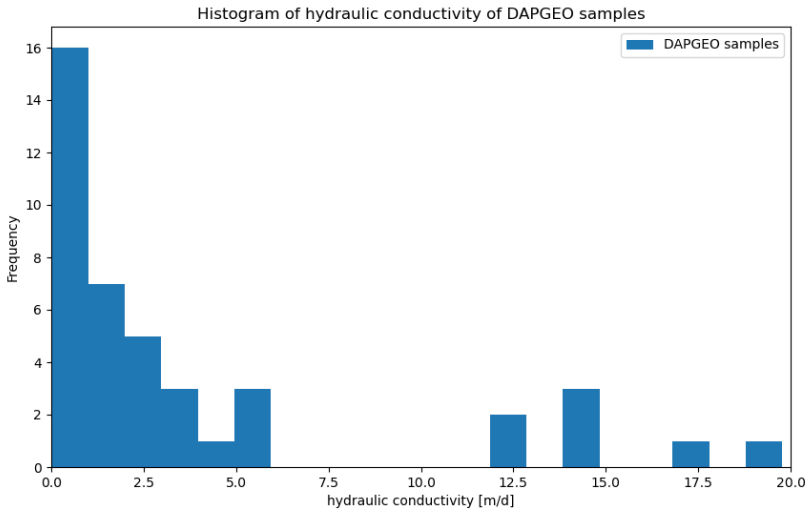

Figure 4.1: Distribution of hydraulic conductivity measurements on the plug scale for DAPGEO-02

The several box plots used in this study share the same general layout, where the horizontal line inside each box corresponds to the median. The boundaries of the boxes are the first and third quartile

respectively. The thin lines outside the boxes show the minimum and maximum value, while potential outliers (further away than 1.5 times the distance of inter-quartile range) are shown as single data points outside of that.

The box plots in figure 4.2 show the plug scale hydraulic conductivities of the DAPGEO sample, grouped by the individual cores they were taken from. It is evident that except for samples from two cores, the plugs all have hydraulic conductivities of 6m/d or lower and the higher hydraulic conductivity samples of 12m/d or more were taken from cores C3 and C4. A larger box plot and therefore value range indicates a higher heterogeneity within the core, with bigger differences in grain size and lithology.

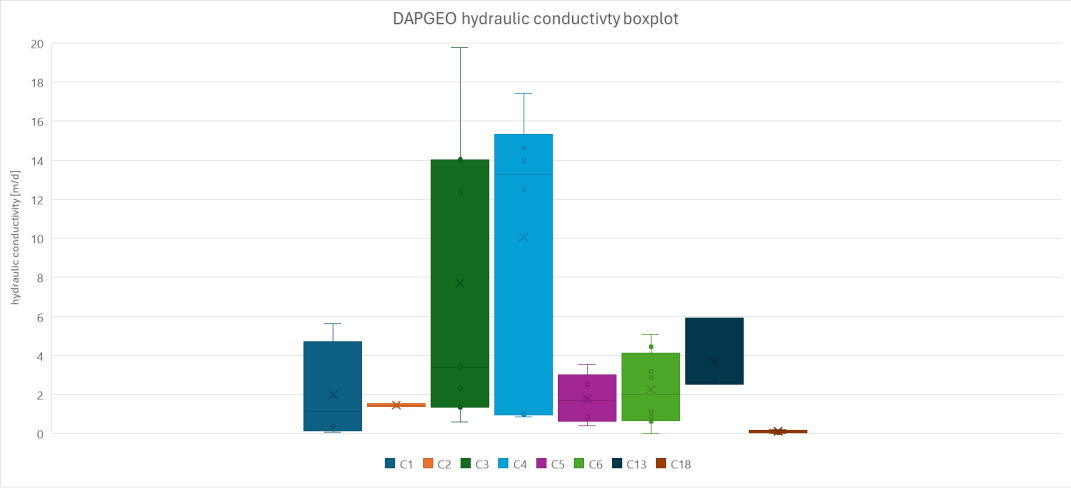

Figure 4.2: Box plots for plug scale hydraulic conductivity for samples from all DAPGEO cores

No relation exists between the depth from which a sample and the corresponding core was taken and its hydraulic conductivity. It is instead solely dependent on the variability of the sediment class between the different plug depths, further outlined in 4.2.

4.1.3. Thermal Properties

The thermal conductivities of DAPGEO samples that were measured in the lab range from below 1.3 up to more than 2.9W/mK (see figure 4.3). Thermal diffusivity values range from 0.42 to 1.24mm^2/s. The lower values were measured at the plug sides most rich in clay, which reflects in the distribution of aquitard samples in the distribution figure below. Similar to the results for hydraulic conductivity, there is no trend apparent with changing depth of the sampled cores, but again a clear depends on grain size/class.

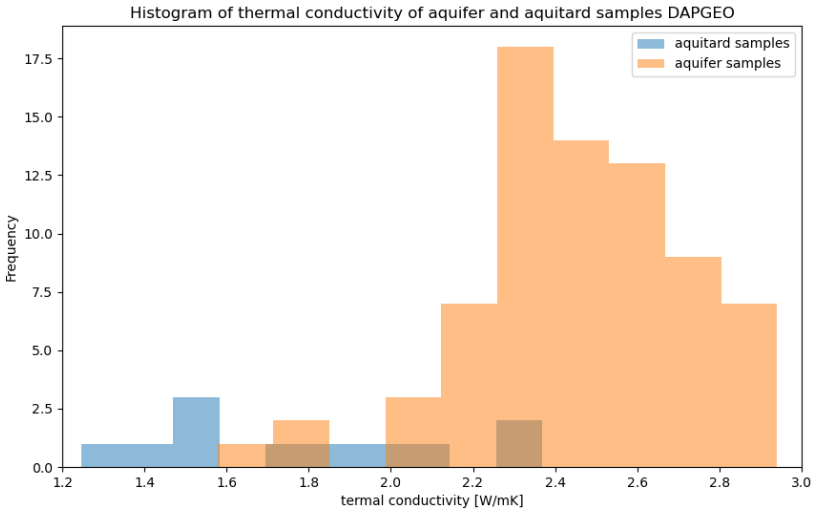

Figure 4.3: Distribution of measured thermal conductivity for DAPGEO plugs, seperated into aquifer and aquitard samples

When assessing the plug scale thermal conductivity within each core, core C4 stands out as the core with the highest average thermal conductivities, while cores C3 and C5 are also showing high average results of more than 2.5W/mK (figure 4.4). It can be noted that C3 and C4 also showed the highest hydraulic conductivities already. These correlations are looked on in more detail later in this chapter.

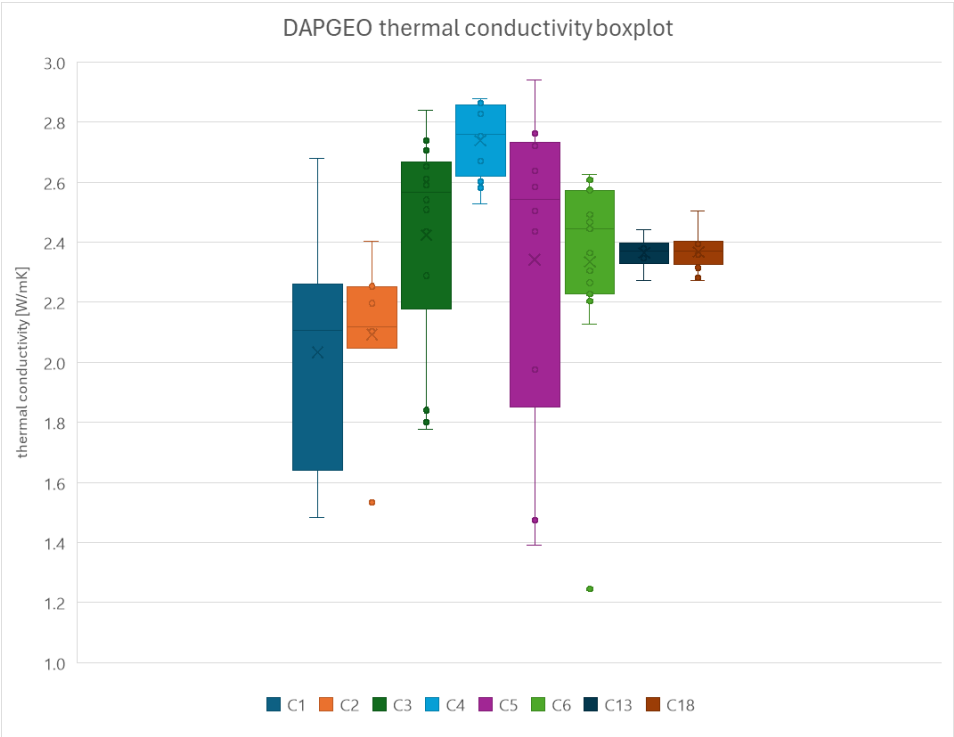

Figure 4.4: Box plot thermal conductivity for all plugs of DAPGEO

4.1.4. Anisotropy of Hydraulic and Thermal Conductivity

An important, but difficult parameter to determine for any subsurface modeling, is the anisotropy of hydraulic conductivity. As this is a scale dependent modeling parameter, it is hard to quantify based on plug scale lab measurements. Figure 4.5 compares all hydraulic conductivities measured from vertical and horizontal plugs of DAPGEO-02 cores and the cores themselves. It is visible that the difference is marginal on the plug scale, where average vertical hydraulic conductivity is 3.15m/d, while average horizontal conductivity is 4.54m/d. Based on that, the anisotropy factor K_h/K_v is 1.44 on the plug scale. When comparing that with the core scale K_v measured over whole cores, the scale dependency already becomes evident. There the average vertical hydraulic conductivity is 1.39m/d, which when compared to the horizontal hydraulic conductivity at plug scale, leads to a anisotropy ratio of 3.26. This is further discussed in chapter 5.

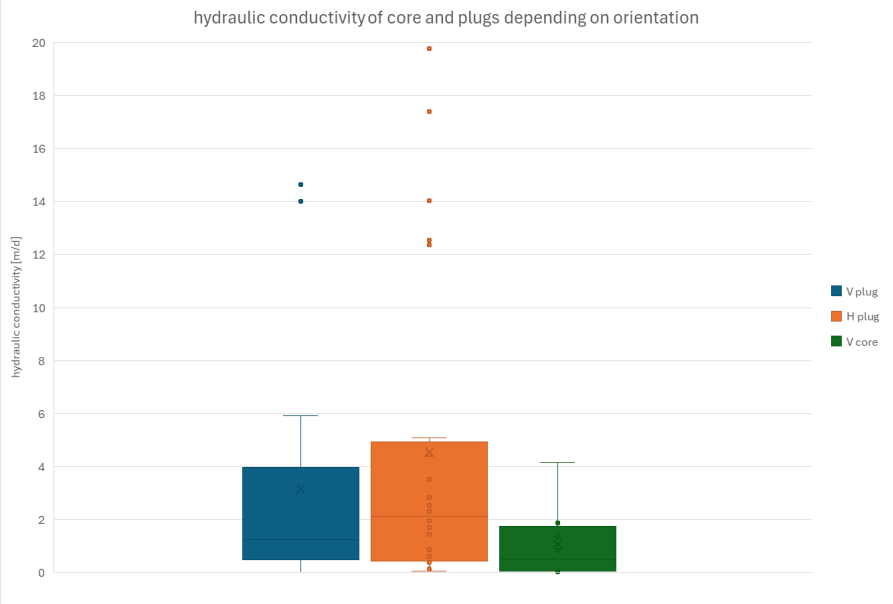

Figure 4.5: Hydraulic conductivity box plots for DAPGEO cores and all plugs depending on orientation

While the anisotropy of thermal properties is assumed to be negligible, it is briefly addressed here. Due to the nature of the Hot Disk measurement principle, the sample is assumed to be homogeneous inside the radius affected by the Hot Disk temperature increase, and therefore anisotropy within one measurement is not possible to quantify. Between the horizontal and vertical plugs taken from DAPGEO, it can be said that the orientation of the plug does therefore not affect thermal property results. As visible in figure 4.6 all three thermal properties determined from the Hot Disk are in the same range for vertical and horizontally taken core plugs. Nevertheless, this is the expected behavior because thermal properties are not known to show anisotropy in saturated soils.

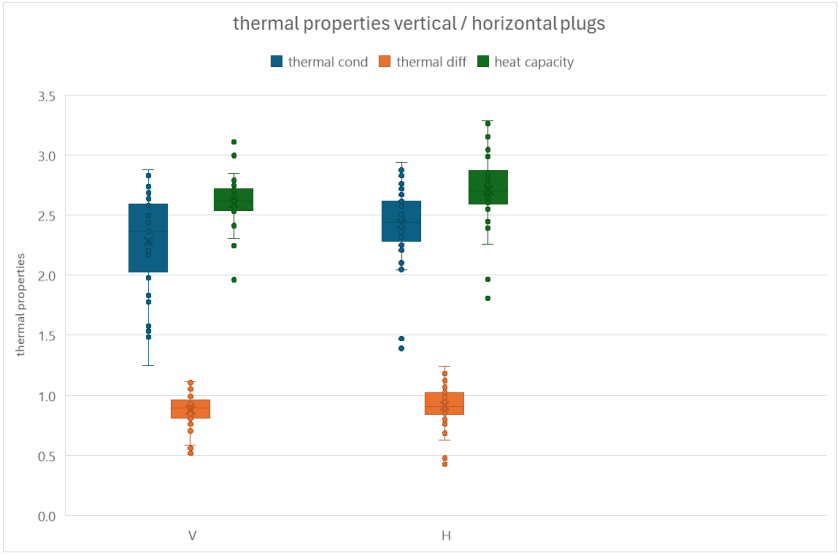

Figure 4.6: Distribution of DAPGEO thermal properties based on plug orientation

4.1.5. Density & Porosity Measurements

As brought up before, only the weight based porosity can be determined for all plugs. For the samples further used for pycnometer density measurements, average solid densities are 2.65 or 2.67g/cm^3, depending on the grain size class (table 4.2). Solid densities calculated from the difference between the wet and the dry sample weight and the sample volume in each sample plug, give a slightly lower average of 2.6g/cm^3 for all DAPGEO samples. The pycnometer measurements provide the more accurate results and should therefore be taken as a reference, including populating a subsurface model.

Table 4.2: Average density of aquitard and aquifer samples resulting from pycnometer measurements

	average density [g/cm^3]
aquitard samples	2.667
aquifer samples	2.650

Comparing the weight based porosity calculations with the density based ones for those samples that were analyzed in the pycnometer, it can be observed that lower weight based porosity values were calculated for most of the samples compared to the density based ones. The calculated porosities for both methods and separated into clay and sand samples can be found in table 4.3. Measured porosities range from about 33% to 47%, when calculated using the weight based method and from 36 to 45% using the density based pycnometer method. The exact reason cannot precisely be determined. Overall the issue could be inaccurate sample volume estimation from the fill level inside the sample rings. Porosities are generally quite high here, the most likely reason for that is decompaction due to all the handling of the samples and conducting measurements with them before determining the porosity. To account for that probable overestimation, in the model used the porosity was reduced to a value of 35% for the entire model domain as a valid approximation.

Table 4.3: Porosity comparison for pycnometer and wet-dry weight difference measurements [in %]

	Pycnometer		**Weight-Based**	
	Aquitard	**Aquifer**	**Aquitard**	**Aquifer**
MIN	36.6	35.8	32.8	31.7
MAX	45.3	41.7	46.9	46.9
AVG	**41.0**	**39.0**	**39.3**	**37.0**

In the shallower cores taken from the DAPGEO borehole, the porosities calculated indicate a slight trend of decrease for increasing core depths (figure 4.7). This could again be related to decompaction though, with the shallower samples showing that to a greater degree.

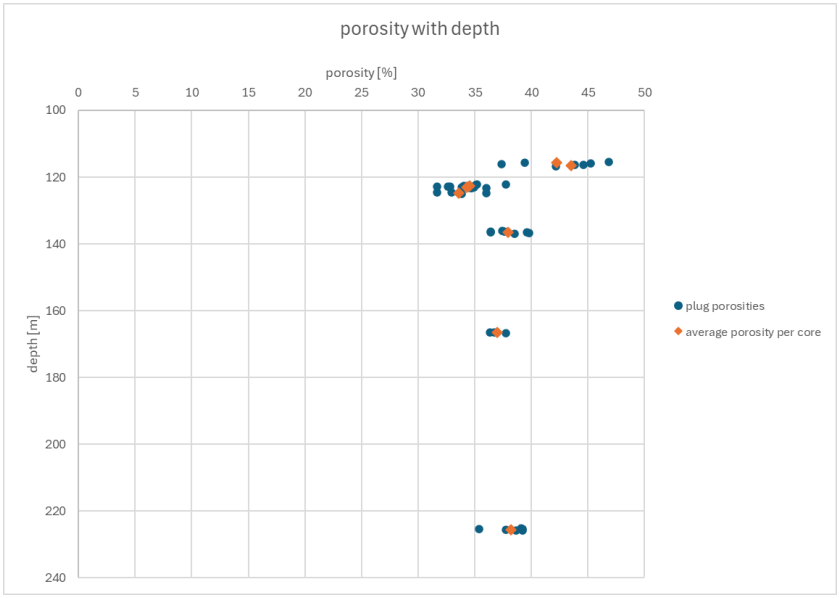

Figure 4.7: Weight based porosity for each plug with depth

Further analysis and correlations of results are discussed in the next section in detail.

4.2. Correlations of Results

4.2.1. Relation between Sediment Class and Results

Based on the classification given to each plug sample from clay to medium coarse sand, the resulting thermal and hydraulic properties can be correlated with their respective sediment classes. In figure 4.8 the distribution of values for the thermal conductivity of each sediment class is displayed. The smaller the grain size of the sediment class, the lower is the measured thermal conductivity. The clay in class 1 also possesses the largest spread in values, indicated by the size of its corresponding box, from $\approx 1.2 W/mK$ to $\approx 2.4 W/mK$. Class 2 sediments show some outliers, especially noticeable on the lower end of measured conductivities. These samples showed small grain sizes, reflecting in measured values close to those of clays from class 1. Fine to medium coarse sands in classes 3 and 4 give similar average thermal conductivities of around $2.6 W/mK$ with the highest measured values of about $2.9 W/mK$ found in these classes.

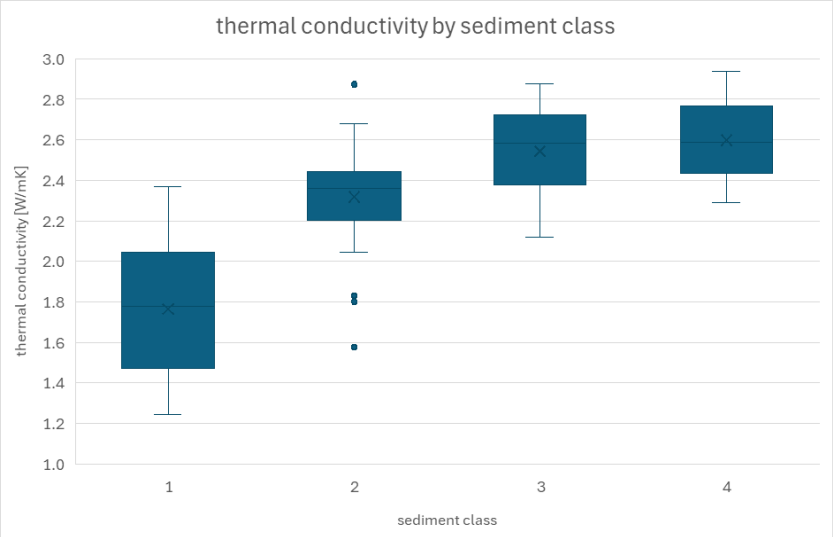

Figure 4.8: Thermal conductivity box plots for each of the 4 grain size classes in DAPGEO samples

Figure 4.9 shows the impact of the grain size classification on the DAPGEO plug hydraulic conductivity KSat results. Medium coarse sediments of class 4 show by far the highest hydraulic conductivities with a large spread of values between 2.5 and almost 20m/d. Overall, finer grain sizes do reflect in lower conductive samples, while also causing a decreasing spread of values, the smaller the grain size class. Clay samples of class 1 are the least conductive with values from 0.01m/d to 1.3m/d. It needs to be kept in mind here that the hydraulic conductivity is a scale dependent property, so the results for sample plugs can't result in a statement regarding larger scales.

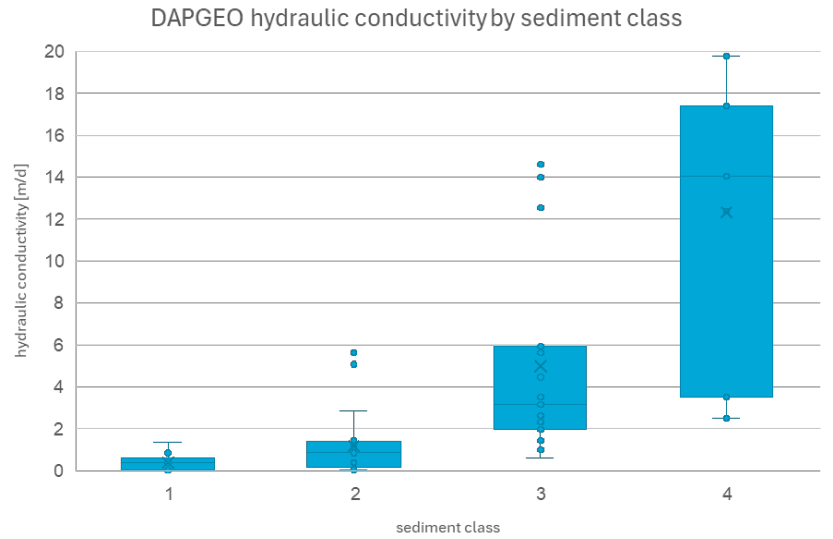

Figure 4.9: Hydraulic conductivity box plots for each of the 4 grain size classes in DAPGEO samples

The average values of the three thermal properties and the hydraulic conductivity measured per class is given in table 4.4. Minimum and maximum values for the thermal conductivity are given in table 4.5.

Table 4.4: Average thermal properties and hydraulic conductivity per class of DAPGEO sample plugs

class	conductivity [W/mK]	diffusivity [mm^2/s]	heat capacity[MJ/m^3K]	hydr. cond. [m/d]
1	1.77	0.68	2.68	0.38
2	2.32	0.89	2.64	1.19
3	2.54	0.95	2.69	4.99
4	2.60	0.99	2.65	12.34
total avg.	2.37	0.90	2.66	3.94

Table 4.5: DAPGEO Thermal Conductivity Maximum and Minimum by Class

thermal conductivity [W/mK]	min	max
class 1	1.25	2.37
class 2	1.58	2.87
class 3	2.12	2.88
class 4	2.29	2.94
overall	1.25	2.94

When looking at the porosity classification by sediment class (figure 4.10) it is apparent that the finer the sediment, the larger the porosity in this case. Clay samples show a large spread of values. This could be caused by the difficulty of handling clay sediments and potential swelling during the experiments and handling of the samples, predominantly present in clays. Therefore the results are likely exaggerated especially for the finer grained samples tested here.

Figure 4.10: Porosity of DAPGEO samples based on wet-dry weight difference for each of the 4 classes

4.2.2. Hydraulic vs. Thermal Properties

When comparing hydraulic conductivity with the measured thermal conductivity (figure 4.11) it is clear that there is a correlation between higher hydraulic and higher thermal conductivities. This is predominantly visible for hydraulic conductivities between 0 and 5m/d with no more clear increase in thermal

conductivity at larger hydraulic conductivity values of coarser class 3 and 4 samples. These results are expected, because clay is usually associated with lower hydraulic and thermal conductivities than samples with higher sand content. This is due to sands mainly being composed of quartz minerals which have a higher thermal conductivity than the minerals in clays. Also the larger grains lead to better fluid flow capabilities and better pathways for heat transfer. This is confirmed when looking at the different sediment classes highlighted by a different color in the plot. The low hydraulic conductivity samples are mostly clay and show the steepest increase in thermal conductivity with growing hydraulic conductivity. Larger differences between measurement trends for the two properties are present in some cores, for example DAPGEO-02-C18. There samples showed quite high thermal conductivity but very low hydraulic conductivity results. This is caused by the surfaces of samples showing sandy grain sizes leading to higher Hot Disk measurement results, while flow through the entire sample plug was not possible in the KSat measurements.

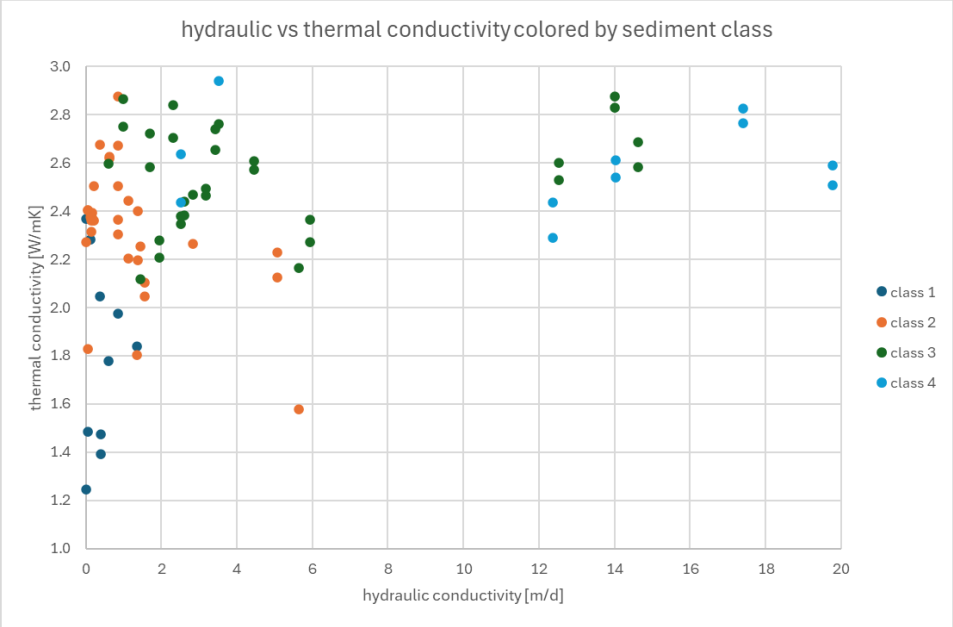

Figure 4.11: Thermal conductivity of plug samples versus their hydraulic conductivity colored by class

Figure 4.12 shows the relationship between the calculated porosity and measured thermal and hydraulic conductivity of the plug samples. There is a slight decreasing trend for thermal conductivity with increasing porosity. As already shown in 4.10, lower thermally conductive clays have a higher porosity so the trend is understandable. The same is true for the hydraulic conductivity, which generally decreases with increasing porosity.

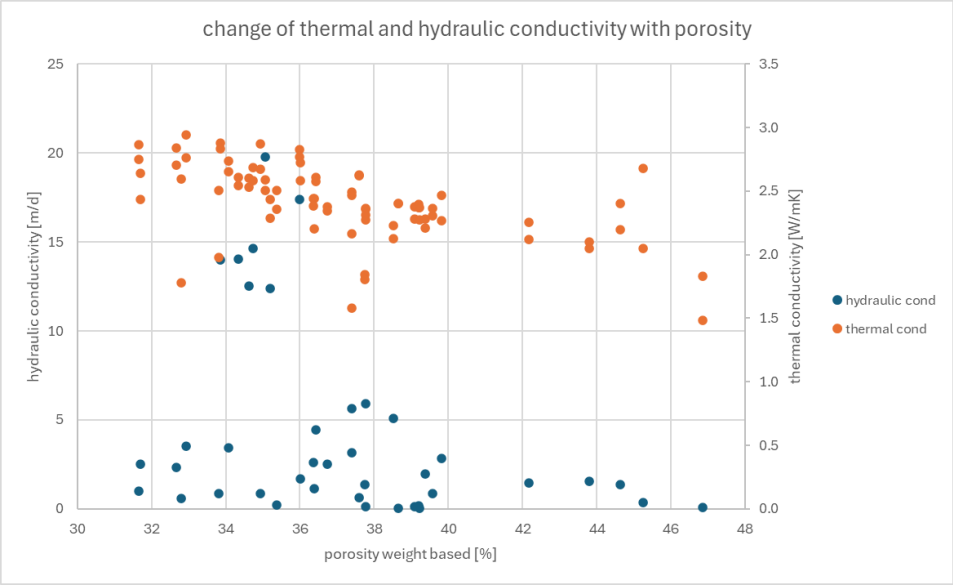

Figure 4.12: Changes of thermal and hydraulic conductivity of the DAPGEO plugs in respect to their porosity

4.2.3. Variability of Results within Well and across Locations

As a consequence of the heterogeneity of the subsurface and the uncertain distribution of different sediment types and therefore sediment properties within them, the results vary across multiple scales. This could be from scales as small as the centimeter scale within each 100ml sample plug, the decimeter scale within individual cores or at the scale of the entire well over several 10s of meters. Properties vary also throughout an entire sediment formation like the Maassluis, where data is available from the four well locations.

The distribution of sediment grain size classes present in the subsamples taken from each core is visualized in figure 4.13 for the DAPGEO cores in 4.13a and the cores from the other three wells Leeuwarden, Maasdijk and Rotterdam in 4.13b.

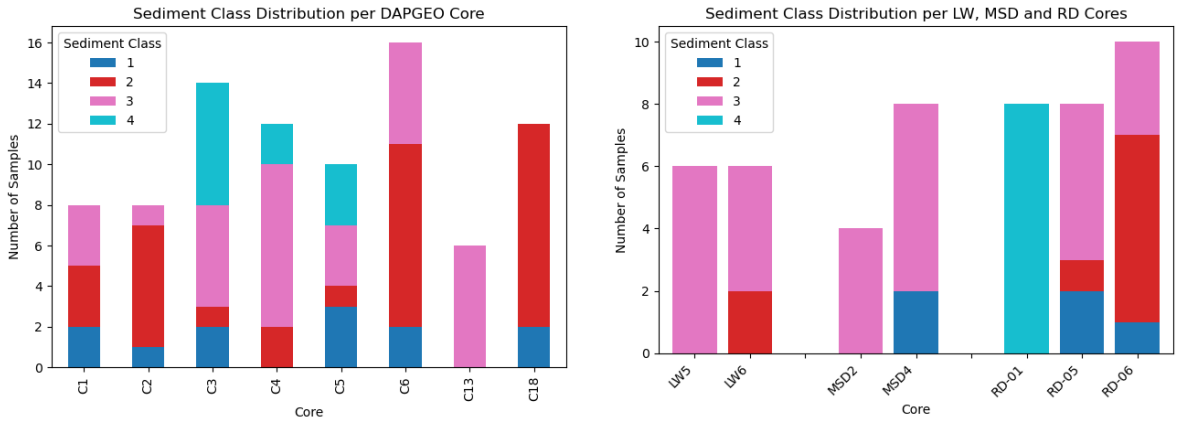

(a) Class distribution for DAPGEO cores

(b) Class distribution for LW, MSD and RD cores

Figure 4.13: The sediment class distribution for the cores taken from the 4 boreholes

Table 4.6 highlights that distribution of the individual classes in each of the 4 wells sampled. The LW

and MSD with only 6 available sample plugs each are limited in their statistical power though. Overall most samples are very fine to fine sands.

Table 4.6: Percentage distribution of classes per well

Class	DAPGEO	LW	MSD	RD
1	14.0%	0.0%	16.7%	11.5%
2	37.2%	16.7%	0.0%	26.9%
3	36.0%	83.3%	83.3%	30.8%
4	12.8%	0.0%	0.0%	30.8%

4.2.3.1. Variability of DAPGEO Results within the Cores and the Well

In an effort to assess that variability, results from within each core and throughout the whole DAPGEO well are analyzed. They can be compared to the well log available from the drilling campaign (B.1). The log gives a very rough description of sediment classes found in the well, not reflecting plug scale changes. Within the depth interval that the cores are taken from (except for C18), the well log indicates fine and medium coarse sands with some layers with higher shell content in between. This can be confirmed as the dominant grain sizes within the cores sampled. The intervals with more coarse sand in the well log between 120m and 125m depth also gave the samples with the largest hydraulic conductivities.

The figures 4.2 and 4.4 show the variability of thermal and hydraulic conductivity within each DAPGEO core. These results align well with the dominant grain sizes from the well log.

4.2.3.2. Comparison between DAPGEO and other Sample Locations

The cores sampled are again compared to the respective well logs. The dominant grain size given in the well logs again aligns with the descriptions and classifications given to the cores and plug samples of the 3 other wells from the lab study. Fine to medium sands are the dominant grain size classes, while some clay can be found in the two deeper Rotterdam cores.

Figures 4.14 and 4.15 show the distribution of hydraulic and thermal conductivity measured on the plug samples. Results are similar to those of the DAPGEO samples. Thermal conductivities mostly range from 2 to 3W/mK, with some lower values for clay rich samples. Hydraulic conductivities are all lower than 7m/d except for one outlier of more than 22m/d in the MSD, which is not plotted here.

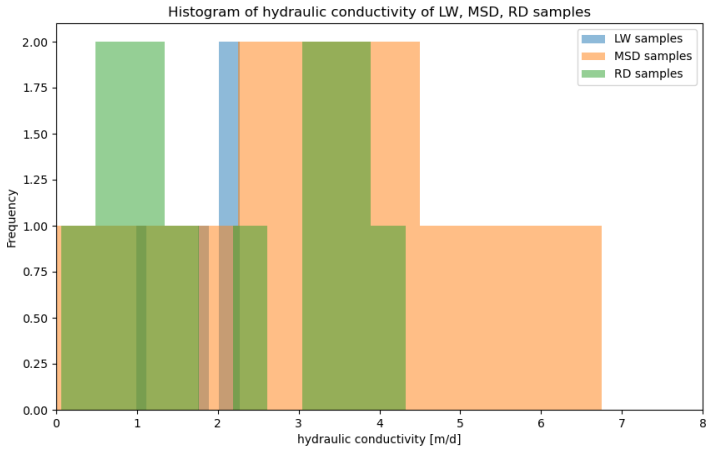

Figure 4.14: Overview of hydraulic conductivity measurements from the LW, MSD and RD wells

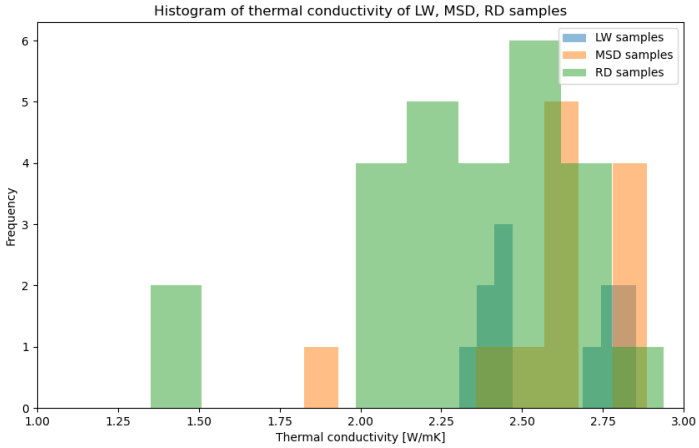

Figure 4.15: Overview of thermal conductivity measurements from the LW, MSD and RD wells

The distribution of results per core for hydraulic and thermal conductivity is displayed in figures 4.16 and 4.17. Because of the small number of samples the box for MSD4 displays this large variance for hydraulic conductivity due to an outlier. Samples from within the same core show slightly lower variability than it was the case for the DAPGEO well. The thermal conductivities are relatively high, with almost all values above 2W/mK, indicating little clay in the plug samples. The only exception is the RD-05 core, which contains clayey samples.

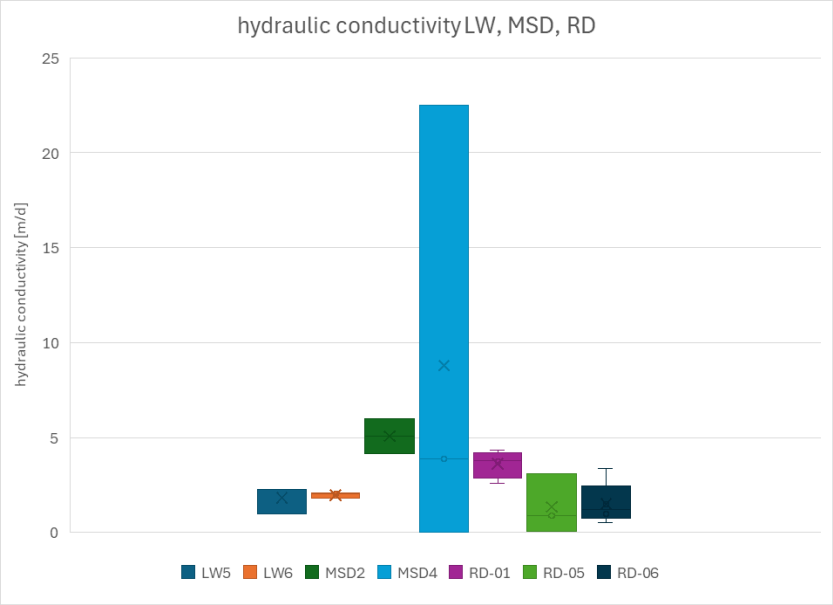

Figure 4.16: Hydraulic conductivities from the cores from the LW, MSD and RD wells

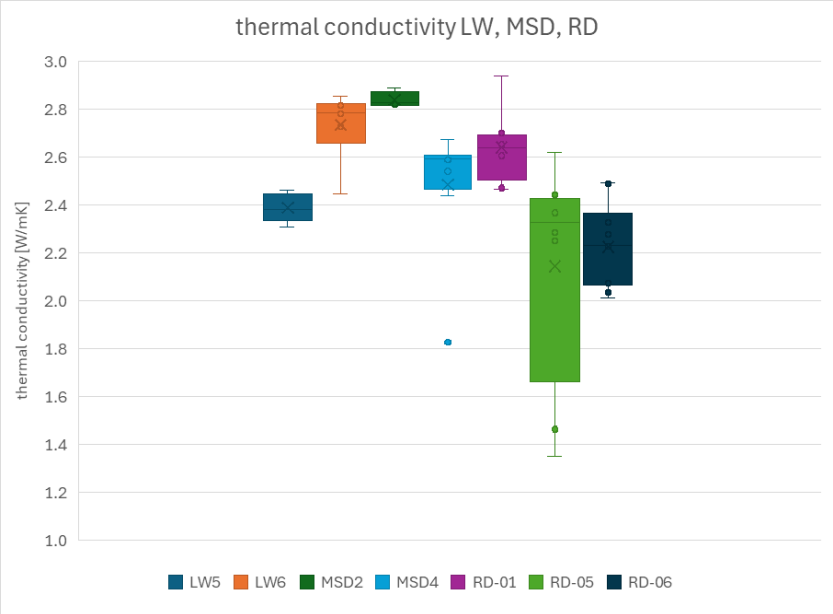

Figure 4.17: Thermal conductivities from the cores from the LW, MSD and RD wells

4.2.4. Correlations with Gamma Ray Readings

Gamma ray log measurements can provide an easy way to judge the presence of clay minerals in measured parameters using well logging data. Here the GR log of the DAPGEO well is used (B.3). Despite the large resolution of the GR that, at least at the plug scale, cannot depict the small scale variations that can be present between different plugs, it still shows hints at trends present, even on that scale. As visible in figure 4.18, higher Kv vertical core conductivities come along with lower GR readings averaged across the core's depth interval (4.18). Even though the sample number is small it can be concluded that the less conductive, clay rich cores show larger GR values, indicating the presence of clays, on the core scale. A similar trend to the Kv results with gamma ray can be seen in figure 4.19 for the hydraulic conductivity on a plug scale, albeit less pronounced than on the core scale. The more conductive plugs with 10m/d or above all give GR readings of 35 API or below. No trend is however visible for changes in thermal conductivity with changing GR values, at least for the number of samples available here.. The variance of these properties within a core is to large for the low resolution (50cm) of the logging tool.

In cores C2 and C6, where the GR readings decrease or increase quite significantly within the depth section of the core (figure B.3), the thermal and hydraulic conductivity values also don't reflect that increase or decrease in clay content within the core that would be expected based on the GR log.

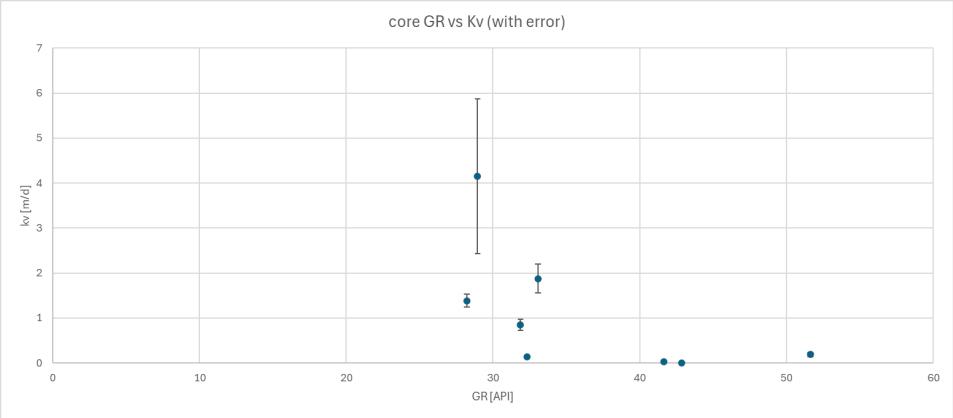

Figure 4.18: GR and core Kv values for each DAPGEO core correlated, including standard deviation for the Kv measurements

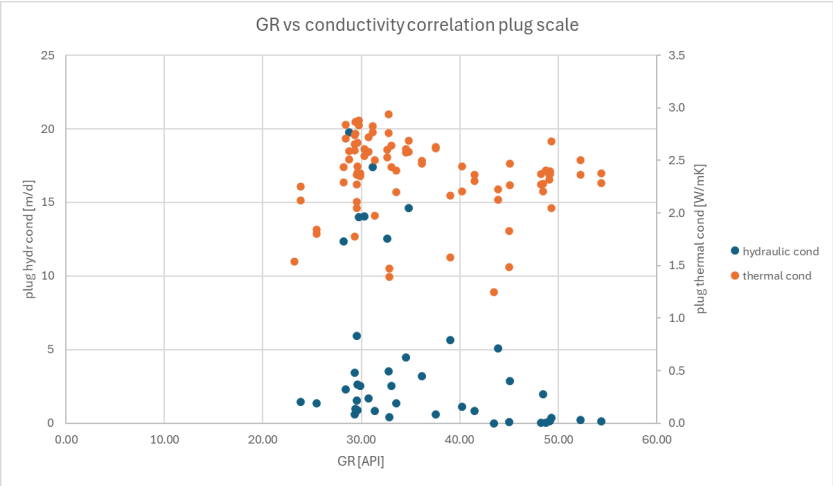

Figure 4.19: Correlation of the hydraulic and thermal conductivity to gamma ray values for each DAPGEO plug

4.2.5. Laboratory Results further utilized in Models

The average, maximum and minimum measured clay and sand thermal conductivities at the DAPGEO-02 well are used for the modeling. An overview of these values is given in table 4.7. For the use in SEAWAT, the diffusivity values need to be converted from mm^2/day to m^2/day as given in equation 3.11, therefore the values are also given in that unit in the table.

Table 4.7: Thermal properties consequently used in the SEAWAT models

	average	**min**	**max**
thermal conductivity aquifer [W/mK]	2.46	2.05	2.94
thermal conductivity aquitard [W/mK]	1.77	1.47	2.37
thermal diffusivity aquifer [m^2/day]	**0.1452**	**0.1208**	**0.1735**
thermal diffusivity aquitard [m^2/day]	**0.1045**	**0.0870**	**0.1397**

4.3. Results of Modeling Campaign

In this section the results of the numerical modeling campaign are presented. Shown first are the solely conductive reference cases and their resulting thermal plumes after the modeled system runtime of 20 years. Following that, the calculated recovery efficiencies resulting from the varied thermal and hydraulic properties in the various cases are shown in detail. Then the extends and impact of the thermal plumes for the different scenarios are featured.

As mentioned in chapter 3 the cases 0 and 1 are solely conductive. They are useful to see the extends of solely conductive thermal plumes over the simulation time. Case 0 starts of with a ”block” of heat in the aquifer extending out til the thermal radius (R_{th}) from the well. Figure 4.20 shows the thermal plume after 20 years for a model with the minimum sediment thermal conductivity measured in the lab and for a model with the maximum thermal conductivity measured. All of the temperature distribution plots contain the isotherm contours for 25°C and 50°C, as well as the isotherms for 13°C, which corresponds to 1K temperature difference to the ambient temperature and 74°C, which is 1K difference to the injection temperature.

The difference between the two conductivity cases is clear, as the 13°C isotherm line (1K above ambient temperature) extends out much further from the aquifer and into the aquitard in case (a) than it is the case for the other model in figure (b), where a warmer heat bubble remains in proximity to the well and the 25°C isotherm extends out slightly further, while the 13°C isotherm extends out less far into the aquifer compared to the other case.

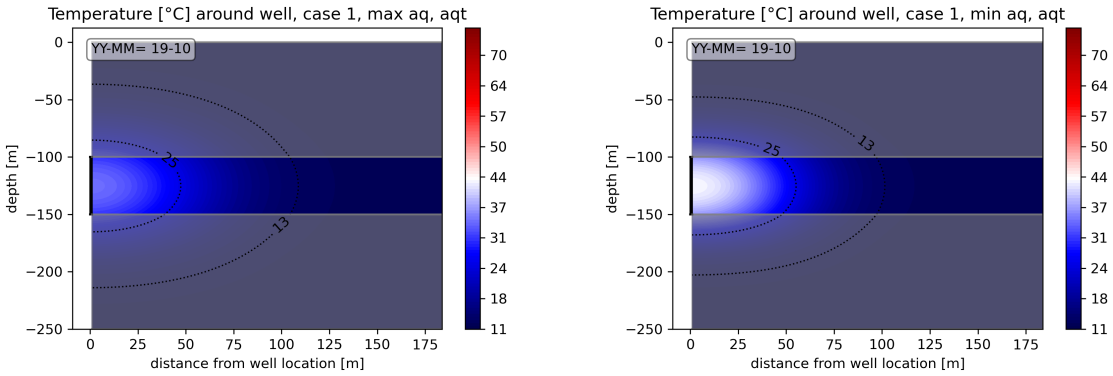

(a) With maximum thermal conductivity

(b) With minimum thermal conductivity

Figure 4.20: Thermal plume for the solely conductive heat bubble after 20 years

Figure 4.21 shows a similar scenario. Here the heat ”block” inside the aquifer is set as a constant temperature boundary condition, analogous to a constant heat supply. Here the isotherms for 13°C reach out further (into the aquitard) than in the previous case, although not significantly. These two cases act as ”worst case” and ”best case” scenarios for heat conduction in the system modeled here.

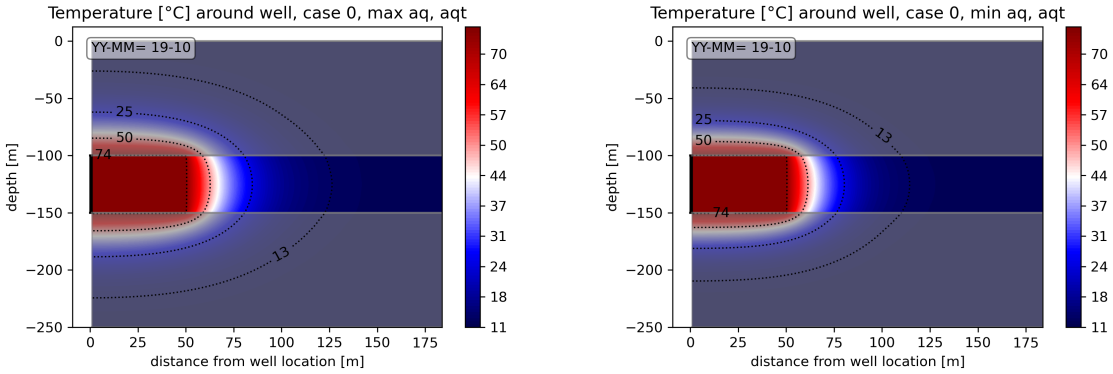

(a) With maximum thermal conductivity

(b) With minimum thermal conductivity

Figure 4.21: Thermal plume for the solely conductive heat bubble with constant heat input after 20 years

4.3.1. Recovery Efficiencies

For model cases 2 to 5, that include an injection-extraction cycle, the recovery efficiencies of the injected heat are of interest to assess system performance. This is done on a yearly cycle, utilizing equation 2.7.

A table including the recovery efficiencies calculated for all cases is attached in the appendix C.1. There the recovery efficiencies per year are shown for the 3rd, 5th, 10th and the 20th year of system operation. All models show an increase in system performance over time, with the growth slowing over time until the efficiencies approach a linear behavior after the full 20 years of simulation runtime. None of the models reach the linear state though, so the maximum recovery efficiency reachable by these models cannot be determined precisely.

The different recovery efficiencies at year 20 for the base case 3 with average hydraulic aquifer conductivity are given in table 4.8:

Table 4.8: Efficiency under different aquifer and aquitard thermal conductivities

Case	Efficiency
Average aquifer & aquitard	80.53%
Max aquifer & aquitard	80.41%
Max aquifer, min aquitard	80.88%
Min aquifer, max aquitard	80.09%
Min aquifer & aquitard	80.48%

The figure 4.22 below gives an overview of the recovery efficiency for every scenario at the 10th and the 20th year of the systems lifetime. This gives a clear picture regarding the performance of systems with varied thermal properties of aquifer and/or aquitard layers. When focusing on scenarios with the same thermal properties, cases with no buoyancy flow are best in regard to recovery efficiency, followed by models with low hydraulic conductivity in the aquifer. Also models with lower anisotropy of Kh/Kv=5 reveal similar performance as models with higher aquifer hydraulic conductivity Kh=10 and anisotropy ratio of 10 throughout all thermal properties. Looking solely at the recovery efficiency at the 20th cycle

the thermal conductivity changes seem to have a minor impact with differences of maximum $\approx 1\%$ across different scenarios.

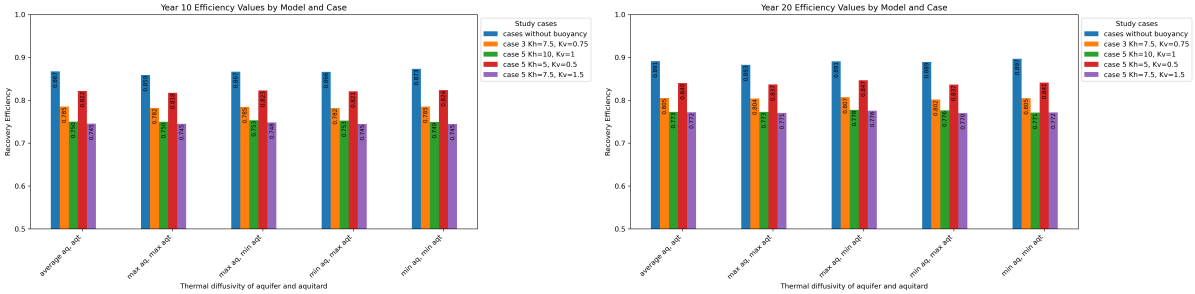

(a) for the 10th year **(b)** for the 20th year

Figure 4.22: Recovery efficiencies by thermal and hydraulic properties of model layers

The following figure 4.23 shows a comparison of the evolution of yearly recovery efficiency for cases 2 and 3 over time, comparing the used varied thermal properties per each case individually. As mentioned, the difference between the two cases is the implementation of temperature-variable density and viscosity in case 3, leading to the occurrence of buoyancy flow in the simulations of that case. Due to the losses introduced by that, the recovery efficiency is lower for all cases, down from almost 92% for the best scenario in case 2 to about 81% for the best scenario in case 3. It can be noted that the model that performed best in the case without buoyancy (minimum thermal properties), isn't the best performing scenario in case of buoyancy flow. There the scenario with high aquifer and low aquitard thermal conductivity performs best now in later years of system operation. This phenomena, as well as the change in best scenario after a couple of operation cycle is further discussed in chapter 5.

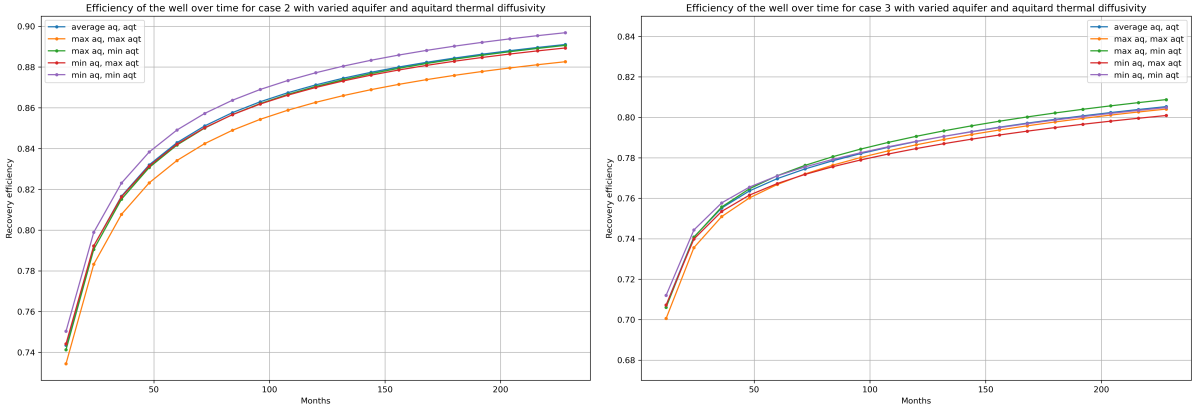

(a) Case 2, without variable density-viscosity effects **(b)** Case 3, including variable density-viscosity effects

Figure 4.23: Recovery efficiencies per year for different model realizations

When considering changes in hydraulic aquifer properties, lower hydraulic conductivity systems perform better for all thermal conductivity scenarios considered, when compared to their counterpart with larger hydraulic conductivity aquifers (see figure 4.24). The change from Kh=5 to Kh=10m/d reduces recovery efficiency at the 20th cycle by $\approx 7\%$. For both cases, a high aquifer thermal conductivity and a low aquitard thermal conductivity is favorable for the highest recovery efficiencies. Here again that change in best performing scenarios over time is observed, later discussed more in chapter 5.

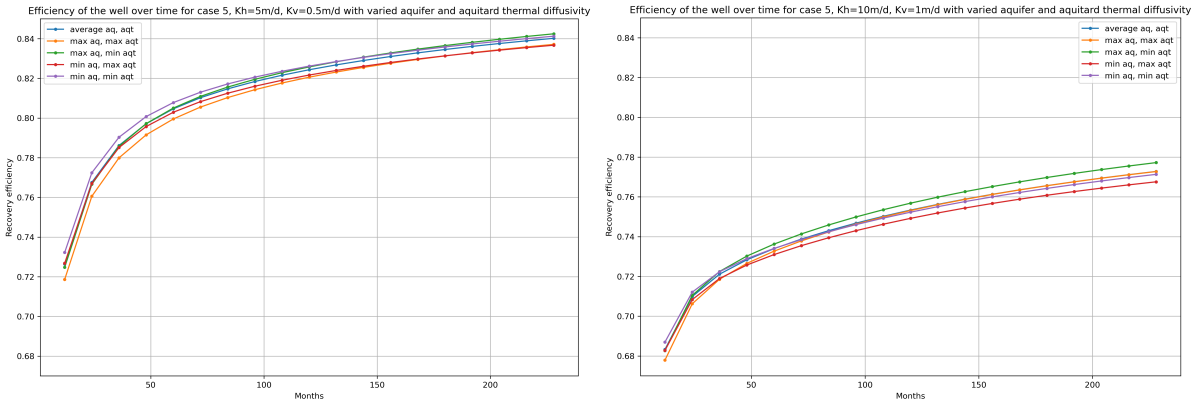

(a) Realization with lower aquifer hydraulic conductivity (Kh=5m/d, Kv=0.5m/d)

(b) Realization with higher aquifer hydraulic conductivity (Kh=10m/d, Kv=1m/d)

Figure 4.24: Recovery efficiencies per year for case 5 with varied hydraulic conductivity

The following two plots (figure 4.25) show the comparison of recovery efficiency over time for the 4 scenarios with changed hydraulic properties of the aquifer. The first figure shows that for maximum aquifer thermal conductivity and minimum aquitard conductivity, while its vice versa for the second plot. The four scenarios all exhibit lower efficiency in case (b) with low aquifer but high aquitard thermal conductivity, compared to their counterparts in case (a). While the scenario with lower aquifer anisotropy initially performs worse than the one with increased hydraulic conductivity, it reaches the same level as the latter one after about 16 cycles in both cases and stays at similar efficiency until the end of the simulation.

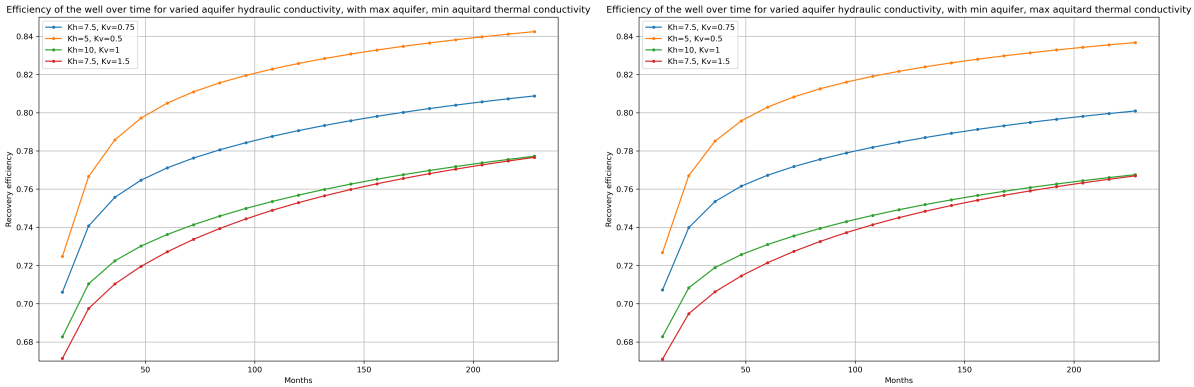

(a) Recovery efficiency across multiple cases for maximum aquifer and minimum aquitard thermal conductivity

(b) Recovery efficiency across multiple cases for minimum aquifer and maximum aquitard thermal conductivity

Figure 4.25: Recovery efficiency across multiple cases for minimum aquifer and maximum aquitard thermal conductivity

4.3.2. Thermal Impact

Another important aspect of HT-ATES systems next to the performance, quantified by the recovery efficiency, is the impact and spread of the thermal plume into surrounding layers and with that mostly the overlying aquitard and potential aquifer layers, due to the uplift of the thermal plume caused by buoyancy flow.

The monitoring lines displayed in figure 3.15 are used for the assessment of thermal impact, as well as

the temperature plume plots and the difference plots between model scenarios.

To display the thermal plume of the case with minimum and the case with maximum thermal conductivity without buoyancy flow as a consequence of temperature dependent density and viscosity as a comparison, these two can be found in appendix C.1. The calculated thermal radius R_{th} can be inferred from that nicely.

In the figure 4.26 below, the thermal plume of case 3, for the scenario with buoyancy flow and maximum aquifer and aquitard thermal conductivity is shown exemplarily. The plumes shown are at their maximum extend, meaning right after the injection cycle of the year shown (see figure 3.14).

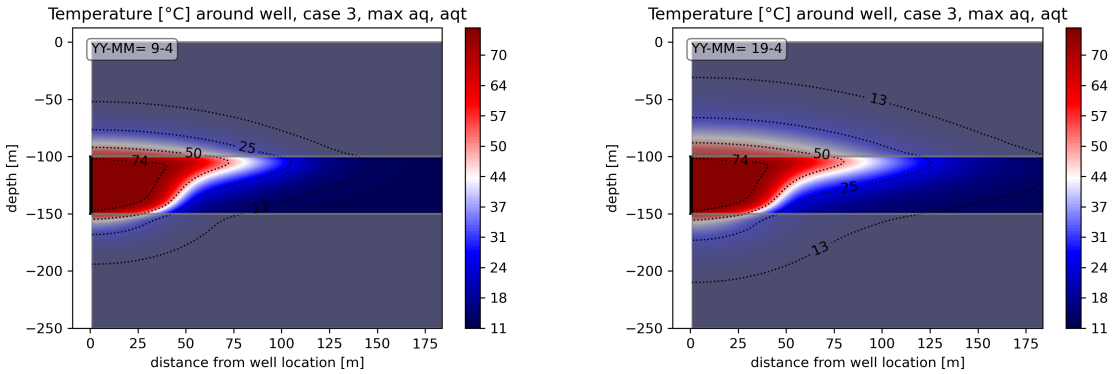

(a) after the 10th injection cycle

(b) after the 20th injection cycle

Figure 4.26: Thermal plumes of case 3, with maximum thermal conductivities after 2 injection cycles (10 and 20 years)

The next figure 4.27 shows the plumes at the same 2 system run times for the same case, but this time the model with the minimum thermal conductivity.

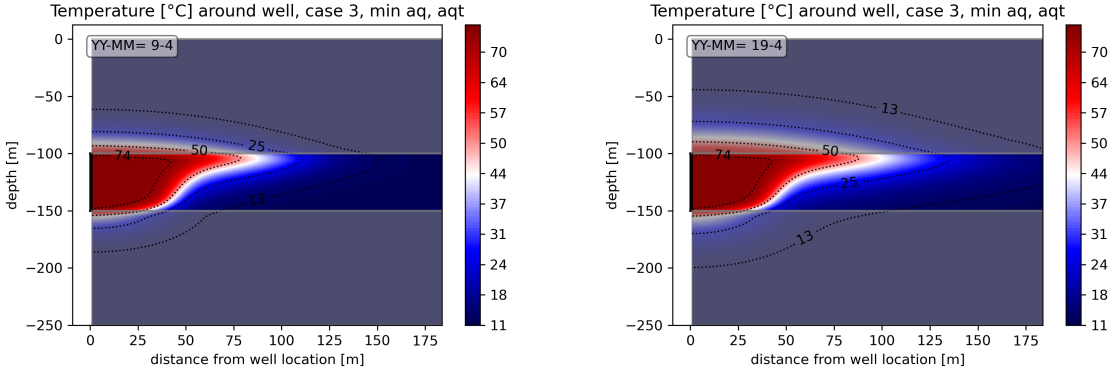

(a) after the 10th injection cycle

(b) after the 20th injection cycle

Figure 4.27: Thermal plumes of case 3, with minimum thermal conductivities after 2 different different injection cycles (10 and 20 years)

Additionally the state of the thermal plume after extraction, so at the timestep of smallest plume extend, can be of interest. This is displayed in appendix C.2. That is the heat bubble remaining inside the subsurface after extraction has taken place in year 20 of operation. It shows the remaining heat bubble inside the aquifer that has moved towards the top of the aquifer layer due to the occurring buoyancy flow and the heat lost towards the over- and underlying clay layer due to conduction. Because of the tilted thermal front, cold water is drawn from the lower part of the well screen, causing the lower recovery efficiencies of HT-ATES systems in comparison with low-temperature variants.

To assess the different thermal impact between the two scenarios of figures 4.26 and 4.27, a sensible option is to plot the temperature difference between the two at both timesteps:

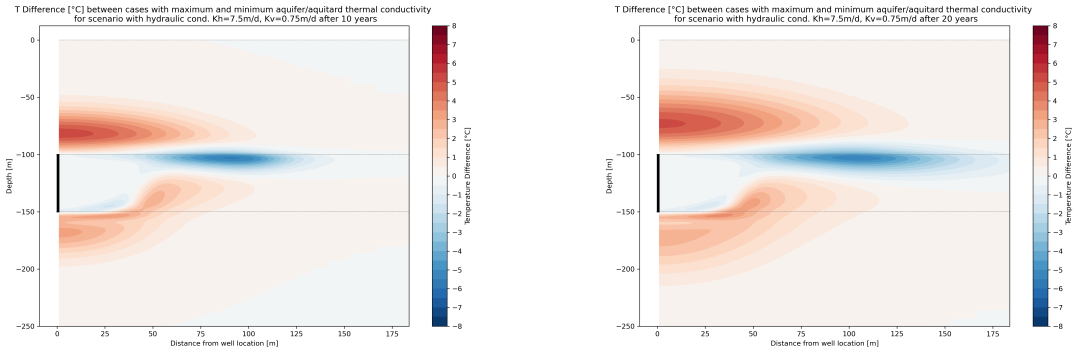

(a) after the 10th injection cycle

(b) after the 20th injection cycle

Figure 4.28: Difference in thermal plumes for two models of case 3 after 2 different injection cycles (10 and 20 years)

As the two figures 4.28 show, in this case the buoyancy flow and therefore the extend of the thermal plume at the top of the aquifer is larger for the model with lower thermal conductivity. Therefore away from the well at the top part of the aquifer the temperature difference is negative in this case, visible as the blue area in the plot. On the other hand the higher thermal conductivity leads to larger conductive losses into the sealing layers closer to the well for the maximum case, leading to positive values of temperature difference in that area, coloured in red. Overall the thermal plume grows over time, reflected in the larger extend of it after 20 compared to after 10 cycles in the plots.

This concept can also be applied to quantify the difference in thermal plumes for models with the same thermal properties but varied hydraulic conductivity (figure 4.29). The resulting temperature difference shows the impact of hydraulic conductivity on plume behaviour. The temperature front at the top of the aquifer reaches out further away from the well in the case (a) of higher hydraulic conductivity while as a consequence of the steeper tilt angle, less heat is stored at the lower part of the aquifer layer. The opposite can be observed in case (b) with lowered aquifer hydraulic conductivity. The subsurface temperature plots for the two cases with varied hydraulic conductivity can be found in appendix C.3 for reference. These plots show the strong impact of hydraulic conductivity on buoyancy flow of the heat plume, as compared to sediment thermal conductivity within expected value ranges.

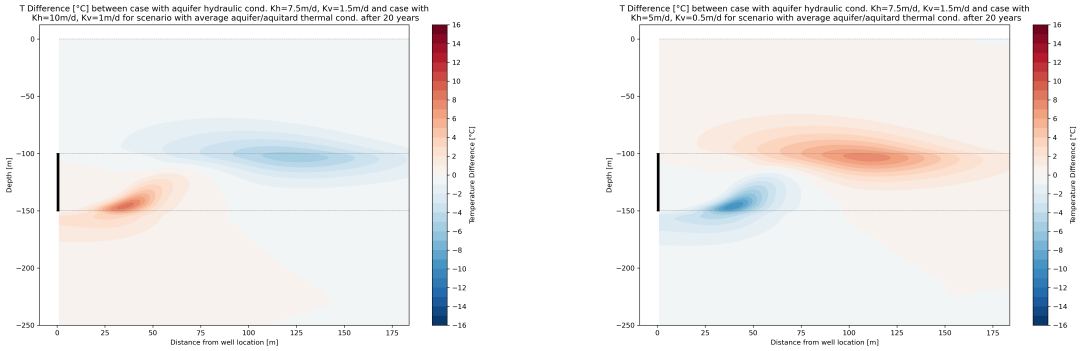

(a) Difference case 3 with Kh=7.5, Kv=0.75m/d and case 5 high, with Kh=10, Kv=1m/d

(b) Difference case 3 with Kh=7.5, Kv=0.75m/d and case 5 low, with Kh=5, Kv=0.5m/d

Figure 4.29: Difference in thermal plumes for two models with different hydraulic conductivities in the aquifer, and average thermal conductivity after 20 years

The thermal impact on the overburden layer and the plume extend can also be assessed using temperature plots along the monitoring lines. These are located vertically at the well and at the extend of the theoretical thermal radius (50m distance from well), and in horizontal direction at the top, in the middle and at the bottom of the aquifer layer (figure 3.15).

The most interesting aspect of the thermal impact of HT-ATES systems is certainly the range of the thermally influenced subsurface in the sedimentary layers located above the storage aquifer. Here the impact will be largest, caused by the upwards movement of the thermal plume as a consequence of buoyancy flow. Especially in aquifers located above the HT-ATES system's sealing clay layer, it is undesirable to induce increased temperatures. For that purpose the temperature of the sealing layer above the well screen is plotted in the following figure 4.30 for varied thermal properties of the base case 3:

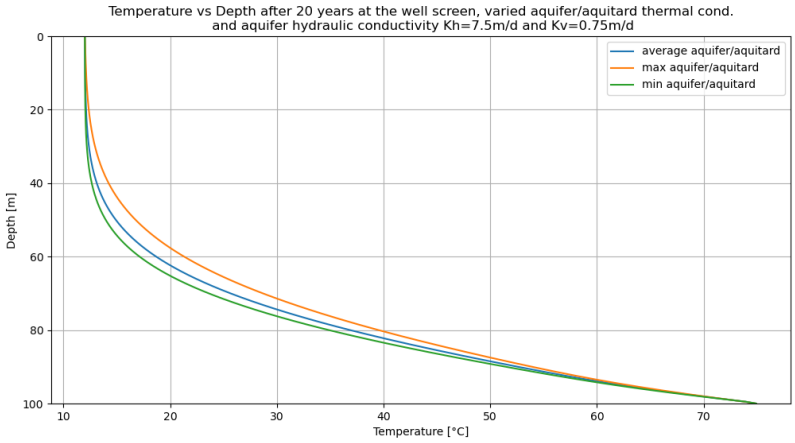

Figure 4.30: Thermal impact in overlying clay layer for different thermal properties of the base case

Here only the average, minimum and maximum thermal conductivity cases are shown. Because the thermal impact is almost entirely governed by the aquitard properties here and the difference of the 25°C isotherm location, chosen here for comparisons, varies only by few centimeters for cases with changed aquifer thermal conductivity, it is neglected here. The scenario with the highest thermal conductivity shows the furthest reach of the temperature plume towards the top of the model, caused by the increased conduction in that case. It reaches 3.71m further than for the average, and 5.99m further than for the minimum thermal conductivity scenarios. A very similar behaviour is observed at a distance of 50m from the well screen. The temperature boundary condition in place for the models used here causes the lines for all cases to converge at the top of the model at a depth of 0m. For scenarios with varied aquifer hydraulic conductivity the difference in thermal impact is very small, with less than 90cm of difference in the 25°C isotherm location between the cases with high and low hydraulic conductivity. The vertical thermal impact over time is additionally displayed in appendix C.4.

In horizontal direction the top of the aquifer is most interesting for HT-ATES systems. Caused by the uplift of the thermal plume over time, it will extend out the furthest from the well there, therefore showing the largest thermal impact in that place. For changed thermal properties, the case with minimum aquifer and aquitard thermal properties shows the largest temperature at distances of 50m or more away from the well screen (figure 4.31), while closer to the well the scenario with higher aquifer but low aquitard thermal conductivity results in the highest temperatures at the aquifer top. The reason for that behaviour is the stronger tilting of cases with lower aquifer thermal conductivity. At the same time, low aquitard thermal conductivity causes less conduction losses into the overburden for these cases.

Thermal impact along the top of the aquifer also depends on the hydraulic conductivity of the aquifer as evident from figure 4.32. The scenario with a lowered anisotropy ratio of 5 leads to the largest temperature there. For the three scenarios with an anisotropy of 10, the ones with higher hydraulic conductivity will lead to larger temperatures along the aquifer top. That shows the clear dependence

of that monitoring parameter on the vertical hydraulic conductivity which is highest in the scenario with an anisotropy of 5 (1.5m/d).

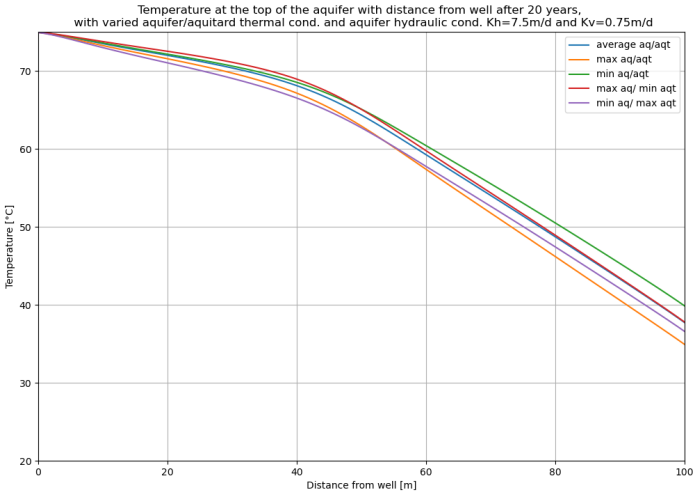

Figure 4.31: Thermal impact at the top of the aquifer with increasing distance from well for varied thermal properties

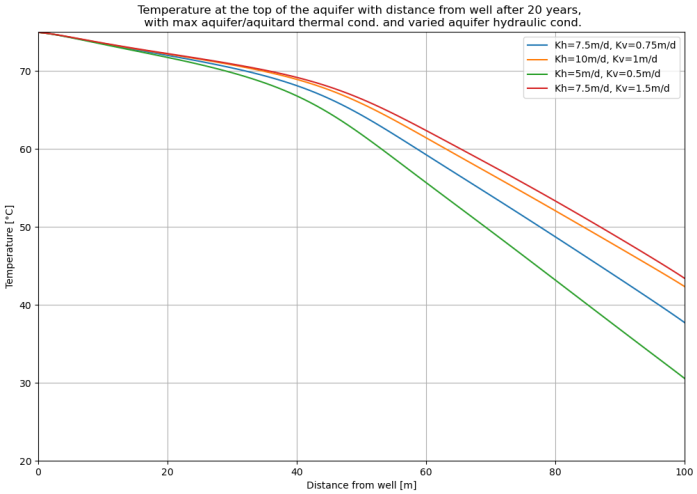

Figure 4.32: Thermal impact at the top of the aquifer with increasing distance from well for varied hydraulic conductivity

4.3.3. Specific Case Study: Aquifer Thermal Conductivity Influence

To really highlight the impact of changed thermal conductivity of the aquifer, a specific case is picked to focus on in more detail. For that, case 3 (the base case) with average hydraulic conductivity for the aquifer of $K_h = 7.5m/d$ and $K_V = 0.75m/d$ is chosen. Within that case two scenarios are compared with the same aquitard thermal conductivity, so the difference in modeling results can be attributed solely to the change from maximum to minimum aquifer thermal conductivity in the models compared.

Recovery efficiencies for the two scenarios are very similar with 80.9% for the case with maximum and

80.5% for the case with minimum thermal conductivity after 20 years. In early years of system runtime however, the case with minimum thermal conductivity performs slightly better at 74.4% compared to 74.1% for the higher conductive case (see figure 4.23 (b) for this). Higher aquifer thermal conductivity makes the heat bubble spread out quicker and therefore increases conduction losses in early years. Nevertheless the small overall differences in efficiency indicate the minor impact of (aquifer) thermal conductivity on the overall performance of HT-ATES systems.

Figure 4.33 shows the thermal plumes for both scenarios after 20 years. The case with lower aquifer thermal conductivity (b) exhibits a more strongly tilted thermal front. This causes the heat plume to reach further into the aquifer at the upper part of the aquifer, creating a larger area where conduction losses to the overlying clay layer occur.

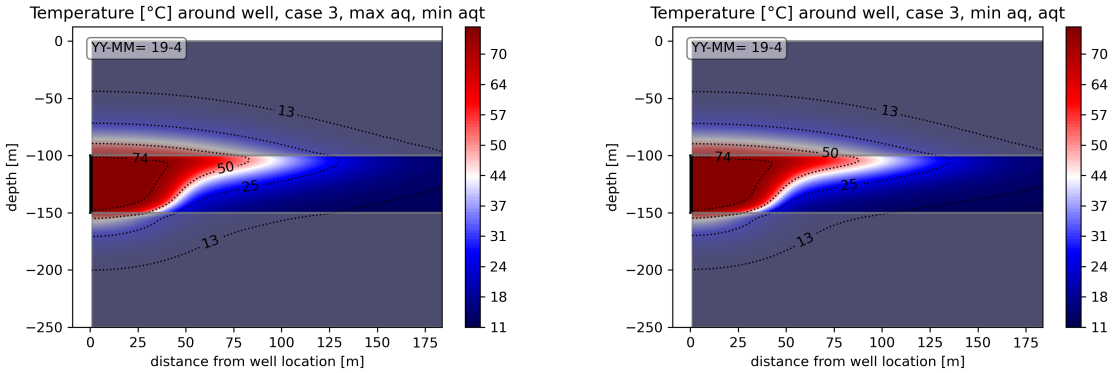

(a) Case with maximum aquifer and minimum aquitard thermal cond.

(b) Case with minimum aquifer and minimum aquitard thermal cond.

Figure 4.33: Base case comparison for varied aquifer thermal conductivity after 20 years of runtime

The thermal impact into the overburden is equal at the location of the well screen for the two scenarios because in both models the aquitard thermal conductivity is kept the same. The 25°C isotherm above the aquifer is located at a depth of about 71m. Regarding the vertical temperature distribution 50m away from the well screen after 20 years, figure C.5 shows it for the state after extraction (a) and after injection (b). While no temperature difference is again apparent for the overburden, both figures indicate a slightly higher temperature at the top of the aquifer at this position for the scenario with low thermal aquifer conductivity, due to the further thermal outreach following stronger tilting. The lower half of the aquifer is warmer in case of the scenario with high thermal conductivity though. At the very bottom and in the upper 30m of the underlying clay layer, this effect is most pronounced at the state of smallest thermal plume extend, right after extraction. This indicates a larger fraction of heat remaining in the lower sections of the aquifer, evidently caused by the less pronounced tilting for the higher conductive scenario.

The impact difference of the two scenarios at the horizontal monitoring line at the top of the aquifer is shown in figure 4.34:

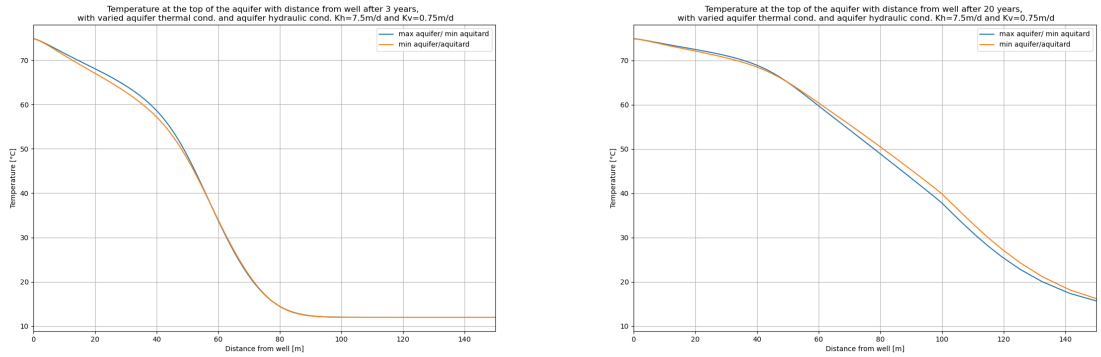

(a) Temperature with distance from well after year 3 **(b)** Temperature with distance from well after year 20

Figure 4.34: Comparison of the horizontal thermal impact at the top of the aquifer after year 3 and year 20, for different aquifer thermal cond.

In figure (a) after 3 years of system runtime, the higher conductive case leads to higher temperatures at the closest 50m to the well compared to the other scenario. After 20 years (b) the difference close to the well becomes less pronounced, however at greater distance than those 50m, the lower conductive scenario shows higher temperatures than the other scenario with maximum thermal conductivity. This change of the plume over time again comes down to the impact of buoyancy flow differences, with the lower thermal conductive aquifer leading to stronger tilting. The slight bend at 100m distance from the well is caused by the grid discretization of the model. The first 100m have cells of constant 1m width, while with further distance than that, the cell width starts to increase logarithmically.

When again comparing subsurface temperature difference plots, as done in figure 4.35 after 10 and 20 years of simulation time, the difference between the two cases shows again, as well as their change with time. The more pronounced tilting of the minimum aquifer thermal conductivity case leads to a negative temperature difference at the aquifer top, with that difference plume growing outwards from the well over time. The temperature difference at the aquifer bottom is negative, also growing outwards over time. The largest temperature differences present in the subsurface between the two scenarios range from -2.96°C to 4.28°C after 20 years.

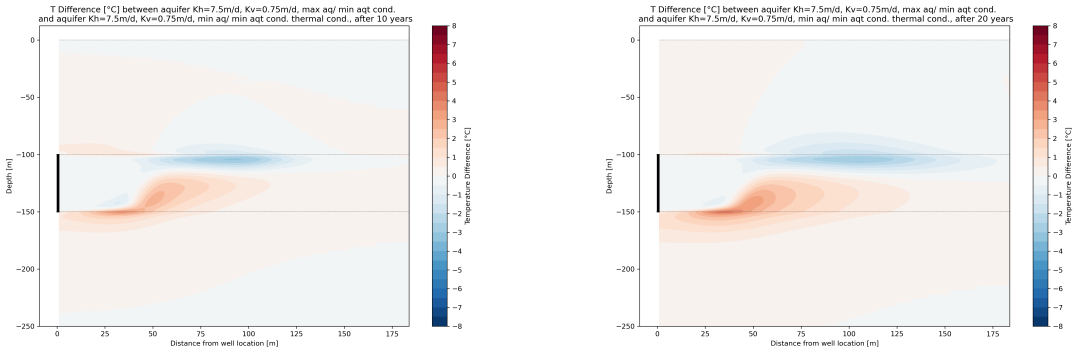

(a) Subsurface temperature difference after 10 years **(b)** Subsurface temperature difference after 20 years

Figure 4.35: Temperature difference for scenarios with maximum and minimum aquifer thermal conductivity after 10 & 20 years

5

Discussion

5.1. Lab study of Maassluis sediments

As mentioned in chapter 2, the results can be compared to expected ranges for Dutch sediments given in the NVOE guidelines (NVOE, 2006). It is clear that the thermal conductivity ranges for sand measured between $2.05 W/mK$ and $2.94 W/mK$ fall within the literature range. That is given with $2.2 - 2.9 W/mK$ for water saturated pure sands and can be lower for sands with increased clay content. The ranges for hydraulic conductivity vary much more greatly. This is also reflected in the results on a plug scale. Ranges from as little as 0.01m/d to >20m/d are measured for the available Maassluis sediments of varied grain size.

The anisotropy of subsurface properties is a main uncertainty of all research on core samples. While the anisotropy of thermal properties is assumed to be negligible, the anisotropy of hydraulic conductivity within an aquifer on ATES system scale is of major interest. Due to its scale dependency it cannot be determined at the scale required for a HT-ATES model based on measurements but instead literature data needs to be used for that. At the centimeter plug scale thin clay layers in the order of centimeters hinder conduction regardless of their orientation. This means that a small lens of clay will have a significant influence on the hydraulic conductivity of that subsample by multiple orders of magnitude independent of the orientation in which the plug was subsampled from the core. Stratification of the aquifer at larger scales of several meters or more can therefore not be evaluated from the lab data. These large scale heterogeneities of horizontally extended (clay) layers are critical for later performance of HT-ATES systems.

As a quick overview of anisotropy present in the core and plug samples used here, the arithmetic mean was used for Kh/Kv estimation. In larger scales where anisotropy is clearly present the geometric mean is a more accurate way of determining the anisotropy ratio.

For using the heterogeneous thermal properties in a simplified subsurface model, they need to either be used to populate the model on a small scale or they need to be upscaled, which is discussed in more detail in the next section.

The porosity of 35% that is assumed here for the aquifer and aquitard layers is based on the calculated values based on sample weight and volume measurements in combination with the commonly used 30% according to NVOE, 2006. It cannot be guaranteed that the clay samples were fully saturated during weight measurements and through handling the samples during the measurements they might have further decompacted. Therefore values are probably slightly overestimated, most notably for clay samples. To account for that, porosity is allocated an overall value of 35% for all layers. This is a reasonable approximation but can have an impact of storage capabilities of modeled aquifers and therefore an impact on system performance.

The specific heat capacity is calculated based on the measured volumetric heat capacity and calculated

density and porosity values. Because these calculated are error-prone, the specific heat capacity of the solid grains that will be used in the model is set to that of quartz at 710J/kg/K. Because porosities are overestimated here, the actual heat capacities calculated for the lab data are lower at around 690J/kg/K.

5.1.1. Correlation of Properties

Based on the lab measurements it can be said that depth has no influence on the resulting thermal and hydraulic conductivities, at least for the shallow layers studied here of less than 300m depth. Instead the results are largely dependent on the grain size or sediment class. The smaller particle size and different mineralogical composition of clays mean they are worse thermal conductor than sands. Similarly the structure of clays make them less capable of conducting fluid flow. Hydraulic and thermal conductivities can also be correlated with each other. For smaller grain sizes (especially clay rich samples) they have a clear linear trend. Increasing hydraulically conductive clay samples (so increasing sand content) grow in thermal conductivity towards values common for sand. When grain sizes and therefore hydraulic conductivities get even bigger (class 3 and 4) this trend reduces as thermal conductivities for sandy sediments stay within the expected range of about 2.2 to 2.9W/mK. This means that thermal conductivity values could be inferred from hydraulic conductivity measurements with satisfying accuracy.

The distribution of the different grain size classes is quite varied within individual up to 1m long cores. Variability can be between values for clays and sands for thermal properties across the core, while individual sample plugs show hydraulic conductivities ranging from few centimeters to several meters per day. For modeling purposes the thermal properties can be upscaled per well using the arithmetic mean if the value at that scale is of interest. For the hydraulic conductivity the scale dependency is significant, so these measurements are only meaningful when used at the scale they are measured at.

Statements that can be made about the lab results regarding the four individual well locations in the Netherlands, are limited by the comparably low number of cores that could be used from the Leeuwarden, Maasdijk and Rotterdam boreholes.

Measured thermal and hydraulic conductivities overall are similar between cores of the different locations. The well log sediment classification of the four boreholes reflect the average properties for each core sufficiently well based on the sediment classes found within the cores.

Gamma Ray readings show correlations with the core scale hydraulic conductivity Kv, where low conductivities are linked to larger GR values. This means that on larger scales GR logs can be used to derive approximate clay/sand contents of the subsurface. The GR results cannot reflect changes on small (plug) scale changes though, due to their measurement resolution.

To summarize, the following statements can be made:

- The measured thermal properties in samples from the Maassluis formation give results all within literature ranges for Dutch sediments for the different grain sizes encountered. Clay samples result in lower thermal conductivity in the range of $1.35W/mK$ to $2.37W/mK$, while for sands the values range from $2.05W/mK$ to $2.94W/mK$. Hydraulic conductivities are also measured but their significance for modeling work is stated to be low due to the scale dependency of that parameter.
- From the grain size classification of the samples it becomes apparent that the measured thermal and hydraulic conductivities are strongly correlated to grain size.
- Overall the uncertainty range of thermal properties is small compared to other uncertainties, especially vertical and horizontal hydraulic conductivity, in the subsurface at aquifer storage scale.

5.2. Modeling Outcome

The modeling outcomes are assessed with respect to different aspects. First the recovery efficiency of the overall system as affected by varied thermal conductivities for the aquifer and sealing aquitards modeled, and with varied vertical and horizontal hydraulic conductivity of the aquifer. Second the thermal impact of the temperature plume on the overburden clay above the storage aquifer, as well as the impact along the aquifer away from the modeled well. Next to that other noticeable findings related to the modeled systems and the impact of varied thermal properties are also discussed.

All the results discussed here are valid for the specific storage system simulated and might not be representative for systems with different storage geometries.

When creating subsurface models, one aspect that can be crucial is the scale at which heterogeneities are implemented in the model. Depending on the scale of data available, either from laboratory or well measurements, the scale at which varying subsurface properties are known will not be that accurately reflected in the model, as upscaling procedures are implemented. The simplified models simulated here are upscaled to a single homogeneous storage aquifer and two homogeneous sealing aquitards. For that the arithmetic mean and minimum and maximum measured values of samples at the plug scale are used. Because of the relatively small uncertainty range of sediment thermal properties its contribution to uncertainty is small compared to other properties like the hydraulic conductivity and its anisotropy. Past studies (eg. Rühaak et al., 2015 or Bridger and Allen, 2014) confirm that assumption, therefore the use of a homogeneous model is justified in this case. One factor that does have a significant effect on HT-ATES systems as compared to LT systems is the possible stratification of the storage aquifer with horizontally continuous, impermeable clay layers. These layers would strongly impact how buoyancy uplift occurs within the aquifer and can not be reflected in upscaled models by using a larger conductivity anisotropy ratio. While that is an important factor to keep in mind it is not assumed to be the case in the models here. The laboratory measurements at the core and plug scale confirmed don't give any information on the continuity of thin horizontal clay layers as these information can't be inferred from cores of 10cm diameter. Beernink, Barnhoorn, et al., 2022 proved that for vertically stratified aquifers with relatively small scale and equally distributed layers, results are equal to homogeneous simulations and averaging is therefore appropriate for upscaling.

Smaller clay patches from within the main target aquifer were not classified as part of the aquifer layer, meaning overall average thermal conductivity within the averaged aquifer could potentially be overestimated. The scenarios modeled here mostly consist of worst-/best-case scenarios with maximum and minimum measured properties anyway. In the case of this study the possibility to include small scale heterogeneities is additionally limited by the axisymmetrical approach used. Smaller locally confined clay lenses cannot be included in those models and would require a 3D modeling approach, resulting in the loss of the advantages of the axisymmetric approach regarding simplicity and computational performance.

Changes of dispersivity throughout the model have also a (limited) impact, the dispersivity is kept static here. For the dispersivity of 0.5 used here, additional losses from dispersion are very low anyway and considered negligible (Gelhar and Collins, 1971).

Overall the interaction of changing various sedimentary, storage or operational parameters on the overall changes in HT-ATES system behaviour is highly complex. Only interaction between changes in hydraulic aquifer parameters and thermal parameters of aquifer and aquitard are studied here.

5.2.1. Recovery Efficiency

The recovery efficiency of a HT-ATES system is dependent on the thermal and hydraulic conductivity of the sediments, but the impact of solely changing thermal properties is limited regarding recovery efficiencies.

The models of case 2 without buoyancy flow show no difference in recovery efficiency, despite changing the hydraulic properties of the aquifer. This can be explained by equation 2.3, showing that the

heat losses without buoyancy flow are independent of hydraulic conductivity. When not considering buoyancy, the case with minimum aquifer/aquitard thermal conductivity results in the best recovery efficiency, as for this case only conduction losses into the aquifer and aquitard are relevant which are smallest for that case. The case with maximum conductivities for clay and sand layers performs worst. Cases with temperature dependence of density and viscosity overall achieve lower efficiencies due to additional losses by free convection or buoyancy flow.

An interesting observation that was made with respect to the recovery efficiencies of modeled systems is the change of system performance over time relative to each other for the 5 scenarios with different thermal properties modeled. Regardless of hydraulic properties of the aquifer, the system performing best in later years of 20 years system operation is the case with largest aquifer and lowest aquitard thermal conductivity. The hydraulic conductivity influences this by determining after how many years the respective changes of highest performing cases happen. In the scenarios with larger vertical hydraulic conductivity (Kv=1.5m/d) the maximum aquifer / minimum aquitard thermal conductivity model is already the best performing one after just 4 years, while in case of the scenario with lowest hydraulic conductivity (0.5m/d) that is the case only after 14 years.

These changes can be explained by the impact of aquifer thermal conductivity on the occurrence of buoyancy flow. A higher aquifer thermal conductivity will lead to less buoyancy flow in the long run of the system, causing higher recovery efficiencies. For higher vertical hydraulic conductivity that effect is in place after a shorter time already. High aquitard thermal conductivity causes losses into the sealing layers through conduction, therefore a lower conductivity is favourable for system performance here. In early years of system operation plume uplift through buoyancy flow is not yet that distinct. This causes cases with low aquifer thermal conductivity to perform better, because the spread of the thermal plume as a consequence of conduction, and therefore loss into the formation, is smaller. Once buoyancy flow takes over as the predominant loss mechanism after a couple years with increasing thermal front tilting this advantage become negligible.

The first cycles losses due to dispersion and diffusion are higher compared to later years, as the surroundings have not warmed up yet. This causes the recovery efficiency to increase with every year.

The geometry of the heat bubble is very important for system performance, unoptimized shapes could lead to increased production of cold water at the aquifer bottom due to tilting and higher conduction losses. According to equation 2.5 the A/V ratio of the stored heat bubble in the modeled scenarios is in the recommended lower range (ratio of 1 here) for HT storage conditions. This ensures that the thermal conductivity impact of the aquifer is low, even for the maximum thermal conductivities measured. The storage geometry of the system will control the impact of buoyancy (Beernink et al., 2024). This is not relevant for the modeling in this study, where the geometry is kept constant throughout the scenarios.

In summary it is clear that the thermal conductivity of the sediments of the Maassluis formation do not have a considerable impact on the total recovery efficiency of HT-ATES systems in the specific cases studied here for a 50m thick aquifer with yearly storage volumes of $250,000m^3$. When only the thermal properties are varied, differences in yearly recovery efficiency are 1% or less in every scenario modeled. These include extreme values of the maximum and minimum measured thermal conductivities measured, so in reality differences based solely on uncertain thermal properties are expected to be even smaller than that. High aquifer thermal conduction is favourable for higher system performance, while aquitard thermal conduction should be low for better performance. The largest sensitivity of thermal recovery was shown to be towards the vertical hydraulic conductivity for fixed storage parameters. Therefore the findings of this study confirm findings from other research (for example Heldt et al., 2024).

Using the minimum and maximum hydraulic conductivities from literature data expected for Maassluis sediments (5 to 10m/d) on a larger scale, models were run to address the impact of these changes on recovery efficiency. Additionally, scenarios with Kh/Kv ratios of 10 and 5 were simulated. Results show that the impact of vertical hydraulic conductivity is most significant for the recovery efficiency of HT-ATES. Between the cases modeled recovery efficiencies differ by as much as 7% in the 20th yearly operation cycle.

5.2.2. Thermal Impact

Conductive transport of heat upwards into the overlying layer may cause problems not only by decreasing the performance of the storage system but also environmental in nature. A temperature increase in aquifers used for drinking water should be avoided. Additionally other ATES systems in proximity may be affected by the system, potentially decreasing their performance. To prevent that from happening the thermal impact is critical as this influences the extends of the heat plume in horizontal and vertical directions.

Because no statement about the expected heat spread and therefore thermal impact can be made based on the recovery efficiencies (Beernink et al., 2020), the thermal impact needs to be considered using numerical modeling. The vertical thermal impact is influenced by the layer structure above the aquifer and its properties, while the horizontal impact is governed by the strength of plume uplift in the aquifer.

The thermal radius R_th good estimate for horizontal heat spread (depending on storage size and parameters), but will be larger at the top part of the aquifer when buoyancy is significant.

The plume uplift and its shape are strongly influenced by the tilting of the thermal front. As outlined in chapter 2 the depends on the aquifer thickness, its hydraulic conductivity and heat capacity, as well as the density and viscosity differences and the injection/extraction cycle. Within the aquifer the volume of heat that is lost as a result of tilting, is the volume that reaches beyond the thermal front (Beernink et al., 2024). This is strongly dependent on the vertical hydraulic conductivity inside the aquifer, with higher conductivities resulting in increased tilting and therefore losses. Overestimating the anisotropy factor and therefore using to low vertical conductivity leads to underestimated uplift of hot water (Hellström et al., 1988). Therefore the efficiency of the system could be overestimated by using high anisotropy ratios and vice versa for low anisotropy ratios. Stronger tilting additionally leads to a larger contact area of the heat plume with the overburden clay. This in consequence increases the area in which conduction losses into the overburden occur, further decreasing performance. Because a residual heat plume stays behind in the aquifer even after extraction due to the buoyancy uplift (figure C.2), the overburden clay is continuously being heated, whereas that is not the case for the clay below the aquifer. Another factor influencing the tilting indirectly is the aquifer thermal conductivity, which can be seen in the thermal plume shapes in for example figure 4.26 and 4.27. Higher aquifer thermal conductivity causes a less sharp temperature front, decreasing the temperature and density gradients in the aquifer. This larger mixing zone will decrease the plume tilt and therefore also limit tilting losses. This mixing zone grows with more storage cycles, but this grow decreases over time (Gao et al., 2024).

In general significantly more losses occur from free convection than from conduction into the overlying aquitard.

A comparison of the influence of varied thermal properties on the impact of the heat plume is done using the 25°C contour in vertical direction at the well screen and in horizontal direction at the top of the aquifer. These parameters are assessed after 20 years, at their maximum extend for the modeling time frame. Here the difference of the contour location in vertical direction is a 6m further reach into the overburden for the base case 3 with maximum thermal conductivities compared to the case with minimum conductivities. In case of the horizontal impact, the 25°C contour reaches out 7.7m further away from the well for the case with minimum thermal conductivities compared to the case with maximum conductivities. As mentioned in chapter 4, when considering the heat spread into the sealing aquitard, the thermal properties of the aquifer are negligible. The 25°C isotherm that is evaluated in the models here will vary only in the order of few centimeters between cases with the same aquitard but varied aquifer thermal conductivity.

Summarizing the key findings of this section, it is shown that the thermal impact in the sealing layer above the aquifer is controlled almost entirely by the thermal conductivity of the clay layer because heat transfer inside of it is solely conductive. The extends of the thermal plume in horizontal direction are governed by the occurrence of buoyancy flow uplift and tilting. This is primarily controlled by the vertical hydraulic conductivity, where a large value is adverse. Thermal conductivity impacts it to a lower degree. Higher thermal conductivity in the aquifer will increase the size of the mixing zone at the temperature front and therefore lower the degree of tilting.

5.3. Limitations

Uncertainties in the results of the lab measurements arise from the measurement limitations mentioned in chapter 3. Generally the results don't give any indications to large errors. The biggest limitation with respect to the sampling is the availability of cores for the LW, MSD and RD wells. The low number makes it difficult to spatially correlate the wells and only a rough estimation can be made. The second relevant limitation is the scale at which measurements can be conducted. This is of course a general problem of core samples and leads to a large uncertainty of the horizontal extend of sediment layers found in the cores.

In reality the lifetime of a ATES systems is usually specified being longer than the 20 year horizon for which the simulations were run here. The curves for recovery efficiency over time (4.23) indicate that the recovery efficiencies approach a constant linear level over time and almost reach that state after the 20 year simulations. This means that the system performance while remaining unknown, is not expected to change drastically over longer runtimes. For the impact of the system on overlying layers and potential aquifers situated above the sealing layer the situation is different. Heat will constantly spread into the sealing layer via conduction. Depending on the thickness of the sealing layer present temperature increase in layers above that could exceed limits. As an example, case 3 of this study shows a temperature of 25°C (increase of 13K) at the well screen up to 34.45m into the overburden aquitard for the maximum measured aquifer and aquitard thermal conductivity. If that is of concern the thermal conductivity of the sealing layer matters for long term operation to ensure safe systems that do not negatively influence other aquifers that for example host other ATES systems or are used as a drinking water source.

It is important to mention that what was shown in this modeling study might not necessarily hold true for systems varying from the one here in terms of geometry and storage volumes and therefore varying shapes of the expected heat bubble in the storage aquifer.

Regarding the discretization of the model grid with cells of 1m width and 0.5m height in well proximity, and length of simulation timesteps of 1 month each, no numerical errors can be seen in any of the results as a direct consequence of a to coarse model. Therefore it is concluded that the chosen discretization is fine enough and there wouldn't have been any benefit from further fining it.

Overall the aquitard in the models here is quite simplified as one thick layer. The real life situation is in similar systems likely to be highly more complex, an example for that is the actual well log profile for the DAPGEO well (see B.1), leading to more site specific impacts on for example other aquifers located above the systems used for ATES systems or other purposes.

Several parts of the HT-ATES system are neglected or assumed as constant for all scenarios, which means their impact on system performance cannot be quantified here. This includes the level of salinity present in the ambient groundwater, or unbalanced or otherwise changed injection-extraction schemes. For example storage phases without any pumping can change the occurrence of heat loss mechanisms. During storage, convection losses will be minimized in relation to conductive losses occurring during those periods. Also only the hot well of a doublet is simulated. Here the relevant processes following from high temperature storage like buoyancy flow are more pronounced compared to the colder well, but especially an interaction between the hot and the colder heat plume has to be avoided in actual two well systems. The scenarios here are also idealized in terms of groundwater flow, which is not considered here. That makes the results more adaptable to general cases, but it can have a negative impact on recovery efficiency as the advective transport will move some of the stored heat away from the well (Bloemendal and Hartog, 2018). The injection volume and temperature, as well as the aquifer thickness are fixed for all cases. As discussed earlier, these parameters will influence the shape of the developing thermal plume and therefore have a major impact on system performance regardless of thermal or hydraulic sediment properties.

The results shown here are valid for the dominant heat loss process in these cases (conduction and free convection). Additional strong advective losses caused by ground water flow are not considered, so the outcomes might be largely different for scenarios involving large ground water flow velocities. Generally the impact of different loss fractions needs to be quantified for each potential HT-ATES individually

because of the amount of parameters affecting performance of these systems. The results are very dependent on the storage dimensions and conditions of the aquifer and its (buoyancy) flow field. The general findings of this study still are applicable to all HT-ATES systems. Although their impact is small, large thermal conductivities for the storage aquifer and small ones for the sealing clays are favourable for system performance. Low vertical hydraulic conductivities or larger anisotropy ratios are preferred to minimize buoyancy and subsequent losses for storage geometries similar to the one modeled here.

5.4. Outlook & Recommendations

For future work on these Maassluis samples building up on the laboratory measurements performed here, it is recommended to perform further sedimentological research like grain size analysis and a generally more accurate lithological description of the sediments themselves and any structures within them on a core and plug scale. Additionally geochemical analysis should be performed to gain knowledge of the mineralogical composition of the sampled sediments.

To improve model calibration, it is crucial to collect further field-scale data on subsurface temperatures and other relevant parameters, for example aquifer scale hydraulic conductivity. For that a Thermal Response Test (TRT) is recommended to gather in-situ temperature data to combine with lab data, aiding in the calibration of models. To further calibrate the model with regard to Kh/Kv ratio as a major uncertainty with big influence on HT-ATES, more field data is required. Well log matching using prediction models could prove to be a sufficient method for the approximation of thermal properties, especially when no cores from a borehole are available. While in this study Gamma Ray logs did not correlate well with the small scale measurements, it can be an accurate enough method at larger scales.

As discussed earlier in this chapter, although likely not greatly beneficial, a geostatistically populated model with finer grid discretization could be researched, particularly when more complex subsurface characteristics are expected. The effect of these more accurate smaller detail models is not known and it's subject to further research if this has significant effect on either recovery efficiency or the thermal impact on confining layers compared to models with averaged thermal properties and hydraulic conductivity upscaled using the anisotropy.

Van Lopik et al., 2016 make use of a salinity contrast of the injected water compared to the ambient groundwater to compensate for buoyancy flow. Although salinity was not considered in this study, this could be a viable option to counter buoyancy losses and it shows potential for further modeling efforts.

The actual impact of the real life system should be studied once operational in the case of the HT-ATES project at TU Delft. For example by utilizing a DTS fiber optic cable monitoring network in wells around the system, the temperature distribution in the underground can be measured and gives conclusions regarding the accuracy of the model used.

6

Conclusion

Extended laboratory and modeling efforts were conducted in order to answer the research questions posed in chapter 1 of this report regarding the impact of thermal and hydraulic sediment conductivity on the performance of a HT-ATES system targeting the Maassluis formation in the Netherlands.

Using cores of up to 1m length taken from four different boreholes in the Netherlands, sedimentary samples ranging from sand to clay were analyzed. From the 15 cores studied overall, 68 smaller scale plug samples were taken. The goal of the laboratory campaign was the population of a Maassluis subsurface database and gathering resulting thermal properties to use in a HT-ATES model. The cores were subject to a falling head hydraulic conductivity (Kv) before being sliced open along their entire length. Thereafter the cores were photographed and described. Subsamples were then taken using 100ml sample rings from different parts of each core. On these fully saturated samples hydraulic conductivity measurements using the KSat apparatus and thermal property measurements using the Hot Disk analyzer were carried out, before the samples were weighted and dried to determine their density and porosity, with some samples subject to pycnometer measurements.

Results indicate thermal conductivities are within literature ranges. Clay samples range from $1.35W/mK$ to $2.37W/mK$, while sandy samples give values between $2.05W/mK$ and $2.94W/mK$. Within the individual cores of each of the four wells the plug samples show quite a high variability with samples from all grain size classes present in some of the cores. As the horizontal extends of smaller scale features like clay lenses can not be inferred from the small diameter sediment cores available, judgments on heterogeneity could not be made in regards to stratification of the formation, in particular large scale clay layers.

The results of thermal and hydraulic conductivity clearly correlate with the grain size classification. Throughout the cores, clay rich samples exhibit lower thermal and hydraulic conductivities.

Correlations between the four wells have proven to be difficult, caused by the low number of sampled cores for the Leeuwarden, Maasdijk and Rotterdam cores. On a plug scale no relationship between Gamma Ray log readings and thermal and hydraulic properties was found, while on a larger core scale, the vertical hydraulic conductivity could be correlated with GR readings.

The range of measured thermal conductivities for sand and clay samples were used in the subsequent setup of a 3-layer axisymmetric SEAWAT numerical subsurface model. This model was aimed at assessing the impact of varying thermal and hydraulic conductivities on a potential HT-ATES system at the location of the TU Delft campus, the Netherlands. For that case a model with a homogeneous aquifer of constant 50m thickness, confined by two 100m thick clay layers, was constructed and simulated with cases without and with a yearly injection-extraction cycle of $250,000m^3$ water, as well as cases without and with buoyancy flow modeled. Additionally to a case with the average thermal conductivities of Maassluis sands and clays, cases with the minimum and maximum values measured for each were considered.

Horizontal hydraulic conductivity of the aquifer has been varied between a the base case with 7.5m/d,

a low (5m/d) and a high (10m/d) case. Next to these with a constant Kh/Kv ratio of 10, a model with $Kh = 7.5m/d$ and lowered anisotropy ratio of 5 was also subject of this study.

The results show very limited influence of varied thermal properties on recovery efficiencies (<1% absolute difference) of the modeled HT-ATES. Varied hydraulic properties on the other hand show a much larger influence of up to 7% difference in recovery efficiency. There especially the vertical hydraulic conductivity and consequently the anisotropy ratio used in the model had large impacts on the performance.

Depending on the thermal properties of the aquifer and the aquitards, conduction and buoyancy flow contribute to a varying degree to the heat losses in the system. These two loss processes mainly also determine the thermal impact of the various scenarios modeled into the sealing layers and along the aquifer with distance from the well.

The spread of heat into the overlying clay layer is for the most part determined by the thermal conductivity of the clay. Higher conductivities will cause increased distance and degree of heat spreading. Heat spread along the top of the aquifer is influenced mainly by the vertical hydraulic conductivity, with a higher one leading to increased buoyancy flow and tilting of the thermal front. Horizontal aquifer hydraulic conductivity and thermal properties play a smaller role in the spreading of the heat plume away from the well.

Overall it can be concluded that the influence of thermal properties on a theoretical HT-ATES system targeting the Maassluis formation in the Netherlands, is relatively small when using the range of measured values in numerical models. These values can be upscaled arithmetically in homogeneous numerical models, while still resulting in accurate prediction of HT-ATES system performance.

When the influence of HT-ATES systems on for example drinking water aquifers or other storage systems located in sediment bodies above the researched system is of interest, attention should be paid on accurately implementing the properties of the overburden. That model can then be used to assess conductive heat spread throughout that sealing layer and its effect on relevant layers located above it.

References

Bakker, M., Post, V., Langevin, C. D., Hughes, J. D., White, J. T., Starn, J. J., & Fienen, M. N. (2016). Scripting MODFLOW Model Development Using Python and FloPy. *Ground water*, *54*(5), 733–739. https://doi.org/10.1111/gwat.12413
Journal Article.

Bakker, M., & Bot, B. (2024). The Effective Vertical Anisotropy of Layered Aquifers. *Ground water*. https://doi.org/10.1111/gwat.13432
Journal Article.

Beernink, S., Oerlemans, P., Zwamborn, M., Schout, G., Koenen, M., Pauw, P., Doornenbal, P., Valstar, J., Bloemendal, M., & Jansen, F. (2022). *Data-acquisitie voor karakterisering van de ondergrond voor HTO: meetprogramma voor pilotlocaties WINDOW* (Technical Report). KWR.

Beernink, S. (unreleased). Core analysis for HT-ATES research: Methods and procedures.

Beernink, S., Barnhoorn, A., Vardon, P. J., Bloemendal, M., & Hartog, N. (2022). Impact of vertical layering and the uncertainty and anisotropy of hydraulic conductivity on HT-ATES performance. *European Geothermal Congress 2022*.

Beernink, S., Bloemendal, M., & Hertog, N. (2020). C2: Prestaties en thermische effecten van ondergrondse warmteopslagsystemen. *WINDOW Project*.

Beernink, S., Hartog, N., Vardon, P. J., & Bloemendal, M. (2024). Heat losses in ATES systems: The impact of processes, storage geometry and temperature. *Geothermics*, *117*, 102889. https://doi.org/10.1016/j.geothermics.2023.102889

Blake, G. R. (2008). Particle density. In W. Chesworth (Ed.), *Encyclopedia of soil science* (pp. 504–505). Springer Netherlands. https://doi.org/10.1007/978-1-4020-3995-9_406

Bloemendal, M., et al. (2020). Feasibility study: HT-ATES at the TU Delft campus. TU Delft/ENGIE.

Bloemendal, M., et al. (2021). A Techno-Economic Evaluation of High Temperature Thermal Aquifer Storage (HT-ATES) for Use with the Geothermal Well on the TU Delft Campus. *Proceedings World Geothermal Congress 2020+1 Reykjavik, Iceland*.

Bloemendal, M., & Hartog, N. (2018). Analysis of the impact of storage conditions on the thermal recovery efficiency of low-temperature ATES systems. *Geothermics*, *71*, 306–319. https://doi.org/10.1016/j.geothermics.2017.10.009

Bridger, D. W., & Allen, D. M. (2014). Influence of geologic layering on heat transport and storage in an aquifer thermal energy storage system. *Hydrogeology Journal*, *22*(1), 233–250. https://doi.org/10.1007/s10040-013-1049-1

Darcy, H. (1856). *Les fontaines publiques de la ville de Dijon: exposition et application des principes à suivre et des formules à employer dans les questions de distribution d'eau* (Vol. 1). Victor dalmont.

Dinkelman, D. (2022). High temperature aquifer thermal energy storage performance in Middenmeer, the Netherlands: Thermal monitoring and model calibration. *European Geothermal Congress 2022*.

Dinkelman, D., & van Bergen, F. (2022). Evaluation of the country-wide potential for High-Temperature Aquifer Thermal Energy Storage (HT-ATES) in the Netherlands. *European Geothermal Congress 2022*.

Doppert, J. W. C., Ruegg, G. H. J., Van Staalduinen, C. J., Zagwijn, W. H., & Zandstra, J. G. (1975). Formaties van het kwartair en boven-tertiair in nederland. In W. H. Zagwijn & C. J. Van Staalduinen (Eds.), *Toelichting bij geologische overzichtskaarten van nederland* (pp. 11–56). Rijks Geologische Dienst.

Doughty, C., Hellström, G., Tsang, C.-F., & Claesson, J. (1982). A dimensionless parameter approach to the thermal behavior of an aquifer thermal energy storage system. *Water Resources Research*, *18*(3), 571–587.

Drijver, B., Bakema, G., & Oerlemans, P. (2019). State of the Art of HT-ATES in The Netherlands. *European Geothermal Congress: Proceedings, Den Haag, Netherlands*.

Ferguson, G. (2007). Heterogeneity and thermal modeling of ground water. *Ground water*, *45*(4), 485–90. https://doi.org/10.1111/j.1745-6584.2007.00323.x

Fleuchaus, P., Godschalk, B., Stober, I., & Blum, P. (2018). Worldwide application of aquifer thermal energy storage – A review. *Renewable and Sustainable Energy Reviews*, *94*, 861–876. https://doi.org/10.1016/j.rser.2018.06.057

Fourier, J. B. J. (1888). *Théorie analytique de la chaleur* (Vol. 1). Gauthier-Villars.

Fuchs, S., Balling, N., & Förster, A. (2015). Calculation of thermal conductivity, thermal diffusivity and specific heat capacity of sedimentary rocks using petrophysical well logs. *Geophysical Journal International*, *203*(3), 1977–2000. https://doi.org/10.1093/gji/ggv403

Gao, H., Zhou, D., Tatomir, A., Li, K., Ganzer, L., Jaeger, P., Brenner, G., & Sauter, M. (2024). Estimation of Recovery Efficiency in High□Temperature Aquifer Thermal Energy Storage Considering Buoyancy Flow. *Water Resources Research*, *60*(11), e2024WR037491. https://doi.org/10.1029/2024WR037491

Gelhar, L. W., & Collins, M. A. (1971). General Analysis of Longitudinal Dispersion in Nonuniform Flow. *Water Resources Research*.

Guglielmetti, L. (2021). HEATSTORE Screening of the national potential for UTES. *HEATSTORE Project*.

Guo, W., & Langevin, C. D. (2002). User's Guido to SEAWAT: A Computer Program For Simulation of Three-Dimensional Variable-Density Ground-Water Flow. *Techniques of Water-Resources Investigations Book 6*.

Gustafsson, S. E. (1991). Transient plane source techniques for thermal conductivity and thermal diffusivity measurements of solid materials. *Review of Scientific Instruments*, *62*(3), 797–804. https://doi.org/10.1063/1.1142087

Gutierrez-Neri, M., Buik, N., Drijver, B., & Godschalk, B. (2011). Analysis of recovery efficiency in a high-temperature energy storage system. *Nationaal Congres Bodemenergie*.

Harbough, A. W. (2000). MODFLOW-2000, the U.S. Geological Survey Modular Ground-Water Model - User Guide to Modularization Concepts and the Ground-Water Flow Process. *Open-File Report*. https://doi.org/10.3133/ofr200092

Hartog, N., Bloemendal, J., Slingerland, E., & van Wijk, A. (2016). *Duurzame warmte gaat ondergronds. Warmteopslag heeft meerwaarde voor warmtenetten: Welke kansen biedt de ondergrond?* (Visie) (Geschreven voor NetbeheerNL). KWR, Greenvis.

Heldt, S., Beyer, C., & Bauer, S. (2024). Uncertainty assessment of thermal recovery and subsurface temperature changes induced by high-temperature aquifer thermal energy storage (HT-ATES): A case study. *Geothermics*, *122*, 103086. https://doi.org/10.1016/j.geothermics.2024.103086 PII: S0375650524001755.

Hellström, G., Tsang, C.-F., & Claesson, J. (1988). Buoyancy flow at a two-fluid interface in a porous medium: Analytical studies. *Water Resources Research*, *24*(4), 493–506.

Hill, M. C. (1990). Preconditioned Conjugate-Gradient 2 (PCG2), A Computer Program for Solving Ground-Water Flow Equations. *Water-Resources Investigations Report*. https://doi.org/10.3133/wri904048

Hot Disk AB. (2019). Hot Disk Thermal Constants Analyser Instruction Manual.

Huizer, J., & Weerts, H. (2003). Formatie van Maassluis. *Beschrijving lithostratigrafische eenheid*, (Nederlands Instituut voor Toegepaste Geowetenschappen TNO).

ISO14688-1. (2017). Iso 14688-1:2017 – geotechnical investigation and testing – identification and classification of soil – part 1: Identification and description [Available from ISO]. *International Organization for Standardization (ISO)*. https://www.iso.org/standard/66652.html

Jansen, F., Oerlemans, P., Schout, G., Beernink, S., & Doornenbal, P. (2023). Resultaten Proefboring Hoge Temperatuuropslag Rotterdam Nesselande. *WarmingUP Project*.

Jansen, F., van Veen, J., Oerlemans, P., Drijver, B., Bakx, E., Doornenbal, P., & Schout, G. (2023). Resultaten proefboring Hoge temperatuuropslag Leeuwarden. *WarmingUP Project*.

Jansen, H., Huizer, J., Dijkmans, J., Mesdag, C., & van Hinte, J. E. (2004). The geometry and stratigraphic position of the Maassluis Formation (western Netherlands and southeastern North Sea). *Netherlands Journal of Geosciences - Geologie en Mijnbouw*, *83*(2), 93–99. https://doi.org/10.1017/S0016774600020060

Kallesøe, A. J., & Vangkilde-Pedersen, T. (2019). HEATSTORE Underground Thermal Energy Storage (UTES) – state-of-the-art, example cases and lessons learned. *HEATSTORE Project*.

Langevin, C. D. (2008a). *Seawat version 4: A computer program for simulation of multi-species solute and heat transport* [Series: Techniques and Methods]. U.S. Geological Survey.

Langevin, C. D. (2008b). Modeling axisymmetric flow and transport. *Ground water*, *46*(4), 579–90. https://doi.org/10.1111/j.1745-6584.2008.00445.x

Li, K.-Q., Chen, Q.-M., & Chen, G. (2024). Scale dependency of anisotropic thermal conductivity of heterogeneous geomaterials. *Bulletin of Engineering Geology and the Environment*, *83*(3). https://doi.org/10.1007/s10064-024-03571-7

Łydżba, D., Rajczakowska, M., Różański, A., & Stefaniuk, D. (2014). Influence of the Moisture Content and Temperature on the Thermal Properties of Soils: Laboratory Investigation and Theoretical Analysis. *Procedia Engineering*, *91*, 298–303. https://doi.org/10.1016/j.proeng.2014.12.064

METER Group. (2012). KSat Operation Manual.

Mindel, J. E., Alt-Epping, P., Landes, A. A. L., Beernink, S., Birdsell, D. T., Bloemendal, M., Hamm, V., Lopez, S., Maragna, C., Nielsen, C. M., Olivella, S., Perreaux, M., Saaltink, M. W., Saar, M. O., van den Heuvel, D., Vidal, R., & Driesner, T. (2021). Benchmark study of simulators for thermo-hydraulic modelling of low enthalpy geothermal processes. *Geothermics*, *96*, 102130. https://doi.org/10.1016/j.geothermics.2021.102130

Noorbergen, L. J., Lourens, L. J., Munsterman, D. K., & Verreussel, R. (2015). Stable isotope stratigraphy of the early Quaternary of borehole Noordwijk, southern North Sea. *Quaternary International*, *386*, 148–157. https://doi.org/10.1016/j.quaint.2015.02.045

NVOE. (2006). Werkwijzen en richtlijnen ondergrondse energieopslag.

Ore, T., Ghanbarian, B., Bohne, K., & Wessolek, G. (2024). Saturation Dependence of Thermal Conductivity of Soils: Classification and Estimations. *International Journal of Thermophysics*, *45*(6). https://doi.org/10.1007/s10765-024-03375-7

Provincie Zuid-Holland. (2015). *Bodem en Ondergrond 2016-2020*. Gedeputeerde Staten van de provincie Zuid-Holland.

RHC. (2013). *Strategic research and innovation agenda for renewable heating and cooling – European technology platform on renewable heating and cooling*. Publications Office of the European Union.

Rogiers, B., Winters, P., Huysmans, M., Beerten, K., Mallants, D., Gedeon, M., Batelaan, O., & Dassargues, A. (2014). High-resolution saturated hydraulic conductivity logging of borehole cores using air permeability measurements. *Hydrogeology Journal*, *22*(6), 1345–1358. https://doi.org/10.1007/s10040-014-1144-y

Rühaak, W., Guadagnini, A., Geiger, S., Bär, K., Gu, Y., Aretz, A., Homuth, S., & Sass, I. (2015). Upscaling thermal conductivities of sedimentary formations for geothermal exploration. *Geothermics*, *58*, 49–61. https://doi.org/10.1016/j.geothermics.2015.08.004

Schout, G., Drijver, B., Gutierrez-Neri, M., & Schotting, R. (2014). Analysis of recovery efficiency in high-temperature aquifer thermal energy storage: A Rayleigh-based method. *Hydrogeology Journal*, *22*(1), 281–291. https://doi.org/10.1007/s10040-013-1050-8

Schout, G., Drijver, B., & Schotting, R. (2016). The influence of the injection temperature on the recovery efficiency of high temperature aquifer thermal energy storage: Comment on Jeon et al., 2015. *Energy*, *103*, 107–109. https://doi.org/10.1016/j.energy.2016.02.122

Sheldon, H. A., Wilkins, A., & Green, C. P. (2021). Recovery efficiency in high-temperature aquifer thermal energy storage systems. *Geothermics*, *96*, 102173. https://doi.org/10.1016/j.geothermics.2021.102173

Smits, K. M., Sakaki, T., Howington, S. E., Peters, J. F., & Illangasekare, T. H. (2013). Temperature Dependence of Thermal Properties of Sands across a Wide Range of Temperatures (30–70°C). *Vadose Zone Journal*, *12*(1). https://doi.org/10.2136/vzj2012.0033

Thorne, D., Langevin, C. D., & Sukop, M. C. (2006). Addition of simultaneous heat and solute transport and variable fluid viscosity to SEAWAT. *Computers & Geosciences*, *32*(10), 1758–1768. https://doi.org/10.1016/j.cageo.2006.04.005

TNO–GDN. (2024). BRO REGIS II v2.2.2 [TNO - Geological Survey of the Netherlands, https://www.dinoloket.nl/en/subsurface-models/map; visited 2025-01-08].

TNO-GDN. (2024). Maassluis formation [Accessed on October 18, 2024]. https://www.dinoloket.nl/en/stratigraphic-nomenclature/maassluis-formation

UN. (2015). Adoption of the paris agreement. united nations, framework convention on climate change, paris.

Van Lopik, J. H., Hartog, N., & Zaadnoordijk, W. J. (2016). The use of salinity contrast for density difference compensation to improve the thermal recovery efficiency in high-temperature aquifer thermal energy storage systems. *Hydrogeology Journal*, *24*(5), 1255–1271. https://doi.org/10.1007/s10040-016-1366-2

Vandenbohede, A., Louwyck, A., & Vlamynck, N. (2014). SEAWAT-based simulation of axisymmetric heat transport. *Ground water*, *52*(6), 908–15. https://doi.org/10.1111/gwat.12137

Vardon, P. J., Dieudonné, A.-C., Abels, H. A., Beernink, S., Meijvogel-de Koning, E., et al. (2023). Geothermal project on tu delft campus - dapgeo-02 core ct-scan data [dataset]. https://doi.org/10.4121/21528819.v2

Visser, P. W., Kooi, H., & Stuyfzand, P. J. (2015). The thermal impact of aquifer thermal energy storage (ATES) systems: A case study in the Netherlands, combining monitoring and modeling. *Hydrogeology Journal*, *23*(3), 507–532. https://doi.org/10.1007/s10040-014-1224-z

Voss, C. I. (1984). *A finite-element simulation model for saturated-unsaturated, fluid-density-dependent ground-water flow with energy transport or chemically-reactive single-species solute transport* (tech. rep.). U.S. Geological Survey. https://doi.org/10.3133/wri844369

Wang, J., He, H., Li, M., Dyck, M., Si, B., & Lv, J. (2021). A review and evaluation of thermal conductivity models of saturated soils. *Archives of Agronomy and Soil Science*, *67*(7), 974–986. https://doi.org/10.1080/03650340.2020.1771315

Wesselink, M., Liu, W., Koornneef, J., & van den Broek, M. (2018). Conceptual market potential framework of high temperature aquifer thermal energy storage - A case study in the Netherlands. *Energy*, *147*, 477–489. https://doi.org/10.1016/j.energy.2018.01.072

Yao, J., & Likos, W. J. (2017). Transient Plane and Line Source Methods for Soil Thermal Conductivity. *Geotechnical Testing Journal*, *40*(5), 858–870. https://doi.org/10.1520/GTJ20160333

Zheng, C., & Wang, P. P. (1999). MT3DMS: A Modular Three-Dimensional Multispecies Transport Model for Simulation of Advection, Dispersion, and Chemical Reactions of Contaminants in Groundwater Systems; Documentation and User's Guide. *U.S. Army Corps of Engineers Contract Report SERDP-99-1*.

Zwamborn, M. (2022). HT-ATES systems in district heating networks, a Dutch benchmark study. *European Geothermal Congress 2022*.

A

Appendix Methods

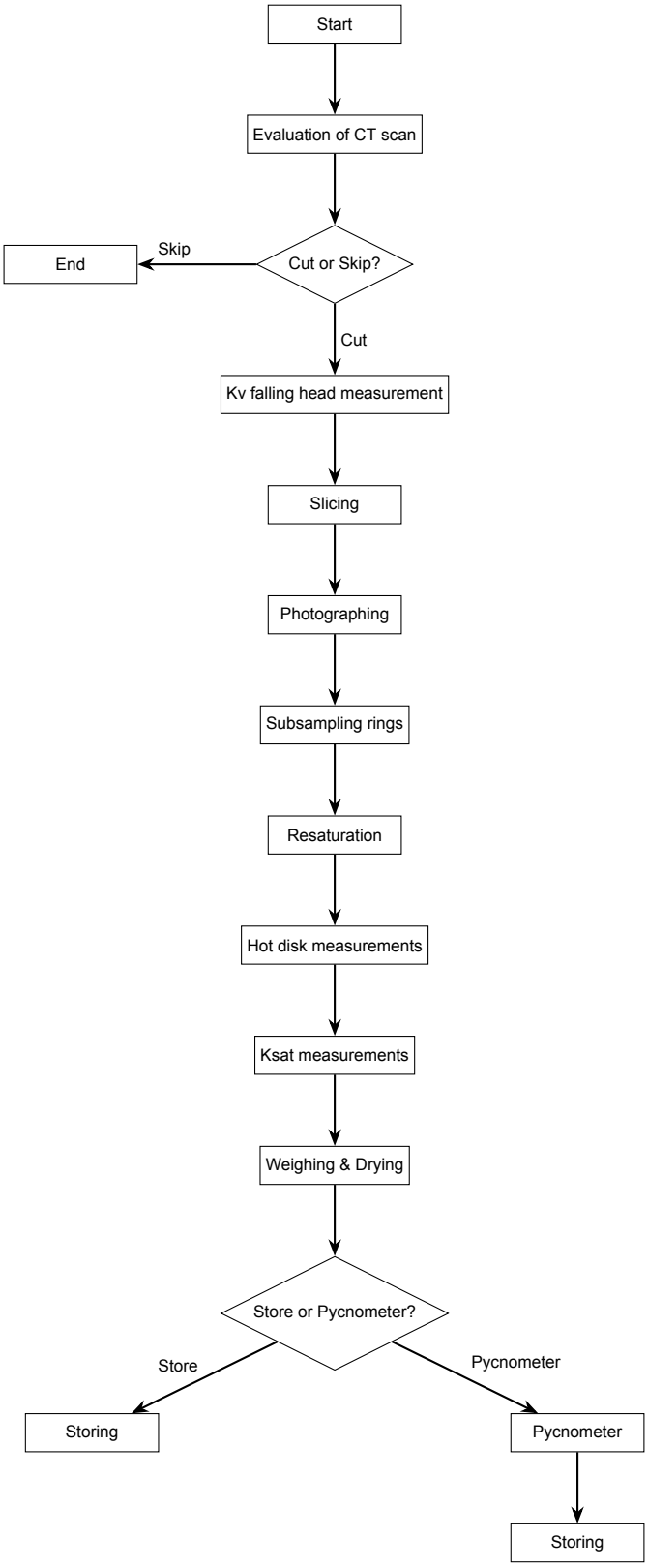

Figure A.1: Flowchart of the sample process

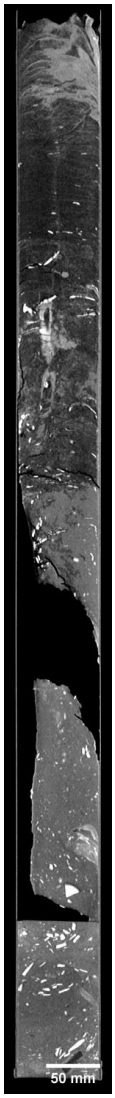

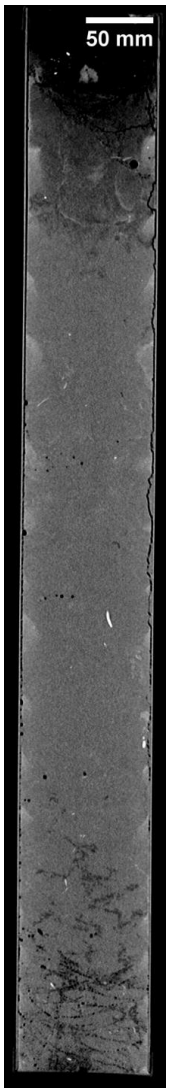

(a) not fully filled core MSD-03 **(b)** core DAPGEO-02-C14 with visible cracks

Figure A.2: CT-scans of unsuitable cores

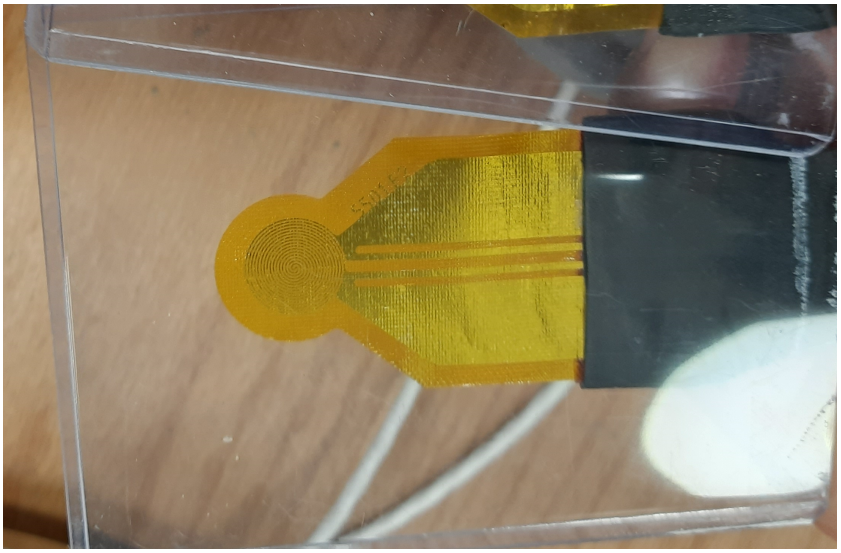

Figure A.3: The Kapton insulated Hot Disk sensor, with the double spiral visible

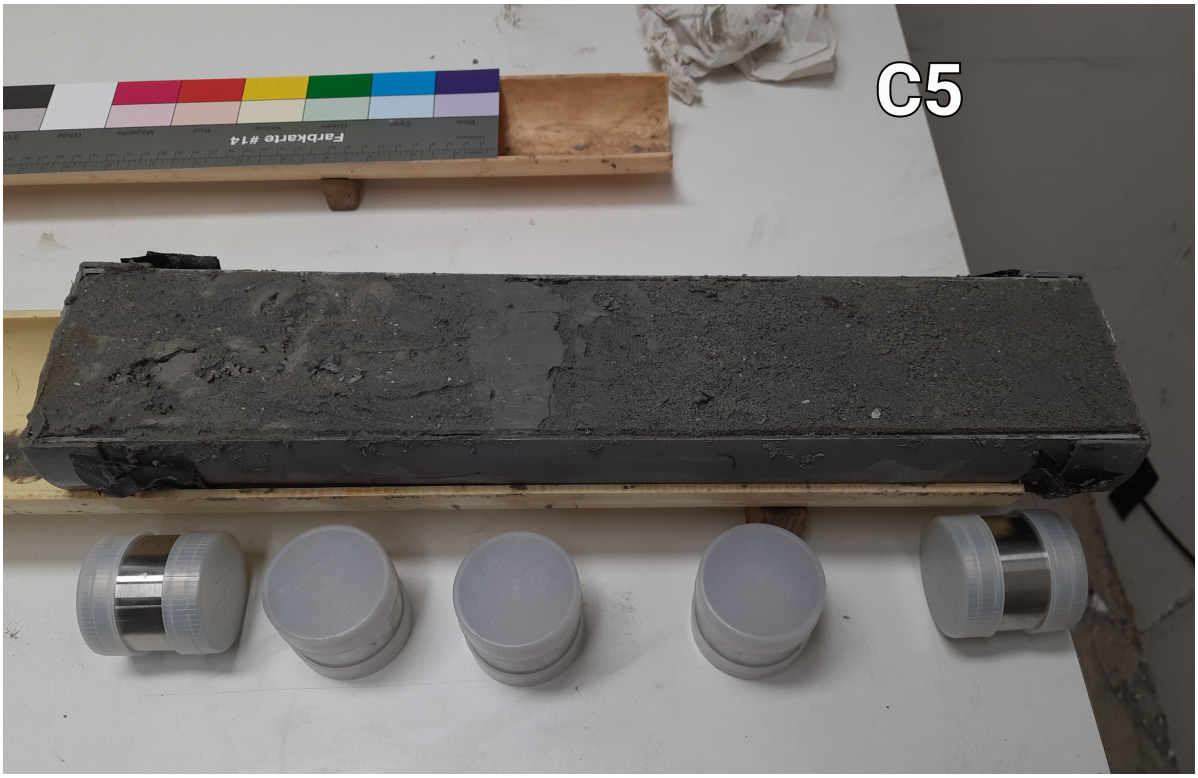

Figure A.4: DAPGEO-02-C5 before plug sampling with the sample rings positioned at planned sampling location and orientation

Figure A.5: Two of the plug samples in their dried state

Figure A.6: A saturated sand sample ring in the adapter for the KSat device

Table A.1: Naming and Orientation of all 68 sample plugs taken from the 4 wells (V: vertical, H: horizontal)

Core	Plug	Orientation	Core	Plug	Orientation
Delft			**Leeuwarden**		
DAPGEO-02-C1	DAPGEO-02-C1-P1	V	LW-05	LW-05-P1	V
	DAPGEO-02-C1-P2	H		LW-05-P2	H
	DAPGEO-02-C1-P3	H		LW-05-P3	V
	DAPGEO-02-C1-P4	V	LW-06	LW-06-P1	V
DAPGEO-02-C2	DAPGEO-02-C2-P1	V		LW-06-P2	H
	DAPGEO-02-C2-P2	H		LW-06-P3	V
	DAPGEO-02-C2-P3	H			
	DAPGEO-02-C2-P4	V			
DAPGEO-02-C3	DAPGEO-02-C3-P1	V	**Maasdjik**		
	DAPGEO-02-C3-P2	H	MSD-02	MSD-02-P1	V
	DAPGEO-02-C3-P3	H		MSD-02-P2	H
	DAPGEO-02-C3-P5	V	MSD-04	MSD-04-P1	V
	DAPGEO-02-C3-P7	H		MSD-04-P2	H
	DAPGEO-02-C3-P7	V		MSD-04-P3	H
DAPGEO-02-C4	DAPGEO-02-C4-P1	V		MSD-04-P4	V
	DAPGEO-02-C4-P2	H			
	DAPGEO-02-C4-P4	H	**Rotterdam**		
	DAPGEO-02-C4-P6	V	RD-01-Wz1	RD-01-P1	H
DAPGEO-02-C5	DAPGEO-02-C5-P1	V		RD-01-P2	V
	DAPGEO-02-C5-P2	H		RD-01-P3	H
	DAPGEO-02-C5-P3	H		RD-01-P4	V
	DAPGEO-02-C5-P4	V	RD-05-Mz2	RD-05-P1	H
	DAPGEO-02-C5-P5	V		RD-05-P2	V
DAPGEO-02-C6	DAPGEO-02-C6-P1	V		RD-05-P3	H
	DAPGEO-02-C6-P2	H		RD-05-P4	V
	DAPGEO-02-C6-P4	V	RD-06-Mz3	RD-06-P1	V
	DAPGEO-02-C6-P5	V		RD-06-P2	H
	DAPGEO-02-C6-P6	H		RD-06-P3	H
	DAPGEO-02-C6-P7	H		RD-06-P4	H
	DAPGEO-02-C6-P8	V		RD-06-P5	V
DAPGEO-02-C13	DAPGEO-02-C13-P1	V			
	DAPGEO-02-C13-P2	H			
	DAPGEO-02-C13-P3	V			
DAPGEO-02-C18	DAPGEO-02-C18-P1	V			
	DAPGEO-02-C18-P2	H			
	DAPGEO-02-C18-P3	H			
	DAPGEO-02-C18-P4	V			
	DAPGEO-02-C18-P5	H			
	DAPGEO-02-C18-P6	V			

Table A.2: Overview of sampled cores from all four boreholes

Cores sampled	depth of core (top) [m]	recovered core length [m]	sampled length [m]
Delft borehole			
DAPGEO-02-C1	115.2	1.06	0.75
DAPGEO-02-C2	115.98	1.025	0.735
DAPGEO-02-C3	122	0.99	0.8
DAPGEO-02-C4	122.7	0.81	0.523
DAPGEO-02-C5	124	1.1	0.455
DAPGEO-02-C6	136	1.1	0.805
DAPGEO-02-C13	166	0.72	0.33
DAPGEO-02-C18	225	0.96	0.665
Leeuwarden borehole			
LW-05	255	1	0.49
LW-06	284	1	0.32
Maasdijk borehole			
MSD-02	213	0.52	0.19
MSD-04	245	1	0.375
Rotterdam borehole			
RD-01-Wz1	93	1	0.65
RD-05-Mz2	170	1	0.8
RD-06-Mz3	183	1	0.8

A.1. Settings Lab devices

Table A.3: Hot Disk Measurement Settings

HOT DISK	
Disk Type	Kapton 5501
Temp. drift rec.	true
Calc. settings	FineTuned, Time corr, default heat cap., perfect insulation
Available Probing Depth	18mm
Total/Char.Time	between 0.3 and 1
Diff Temp	below 100ym
Temp. Incr.	between 2 and 5K
Outp. power.	varying (sample dependent)
Meas. time	varying (sample dependent)

Table A.4: Ksat Measurement Parameters

KSAT	
Mode	Falling Head
Sample rate [s]	Auto
Crown type	Filter Plate Crown
OPERATION PARAMETERS	
H_end_abs [cm]	0.5
H_end_rel [-]	0.25
dH_min [cm]	0.1
dH_ini [cm]	1
GEOMETRY PARAMETERS	
A_bur1 [cm^2]	4.524
A_cap_in [cm^2]	0.075
A_sample [cm^2]	19.6
L_bur [cm]	22.5
L_sample [cm]	5.01
L_plate_Bottom [cm]	0.8
L_plate_Top [cm]	0.3
EVALUATION PARAMETERS	
T_ref [°C]	10
K_plate [cm/d]	14000
Use Auto-Offset	TRUE
Max Auto-Offset [cm]	1
Trigger Auto-Offset [cm]	1

Table A.5: Measurement parameters for the pycnometer

Anton Paar Ultrapyc 5000	
max 5 measurements, 3 averaged	
Measurement Settings	
Gas Type:	Helium
Target Pressure:	10.0000 psi
Flow Direction Mode:	Reference First
Equilibration Mode:	Pressure
Temperature Control:	On
Target Temperature:	20.000 °C
Flow Mode:	Fine Powder
Cell Size:	Medium
Preparation Mode:	Pulse
End Mode Criteria:	Better than 0.05%

B

Appendix Results

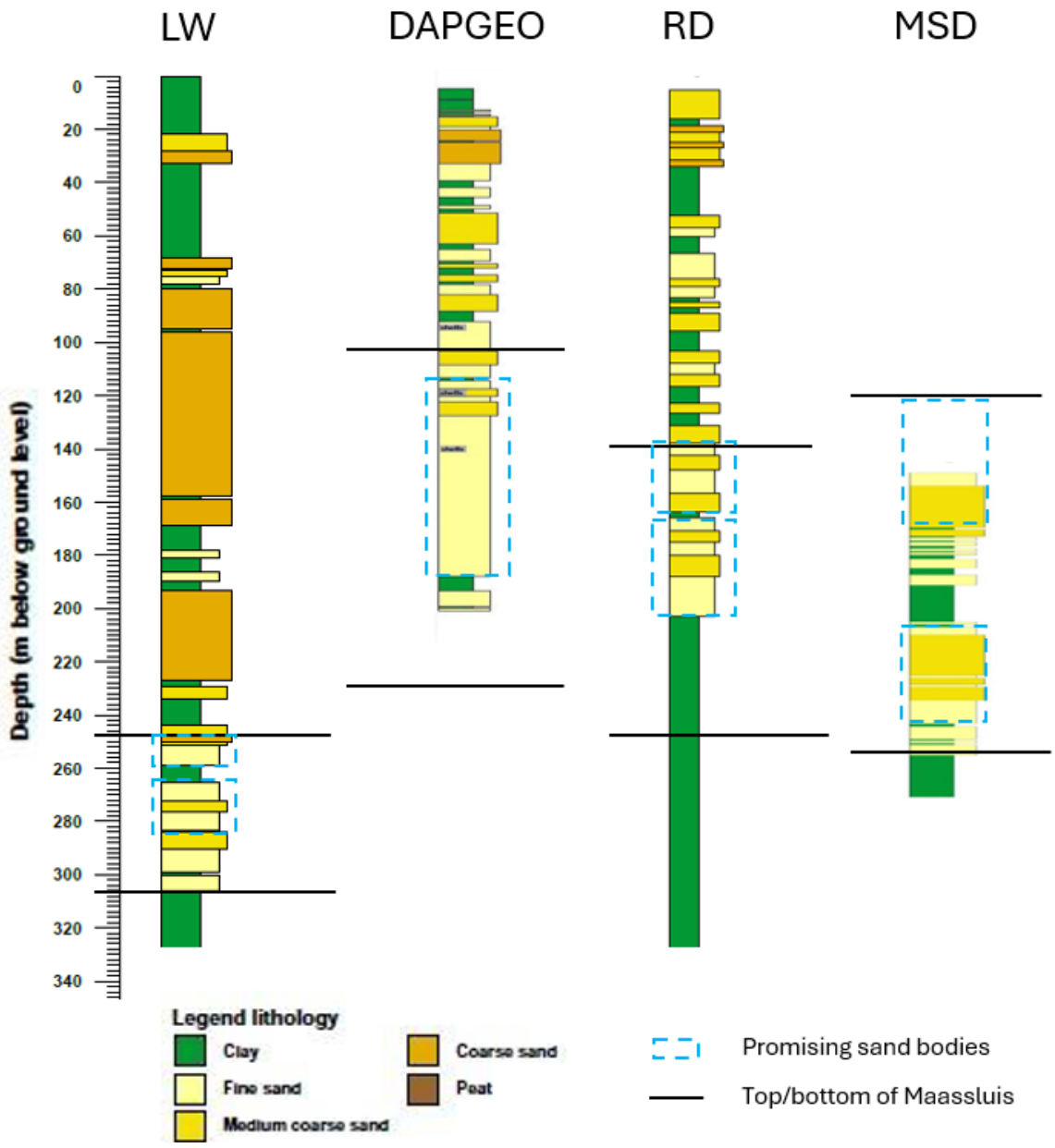

Figure B.1: The location of the Maassluis and promising sand bodies marked within the well logs of all locations, as taken from the drilling reports

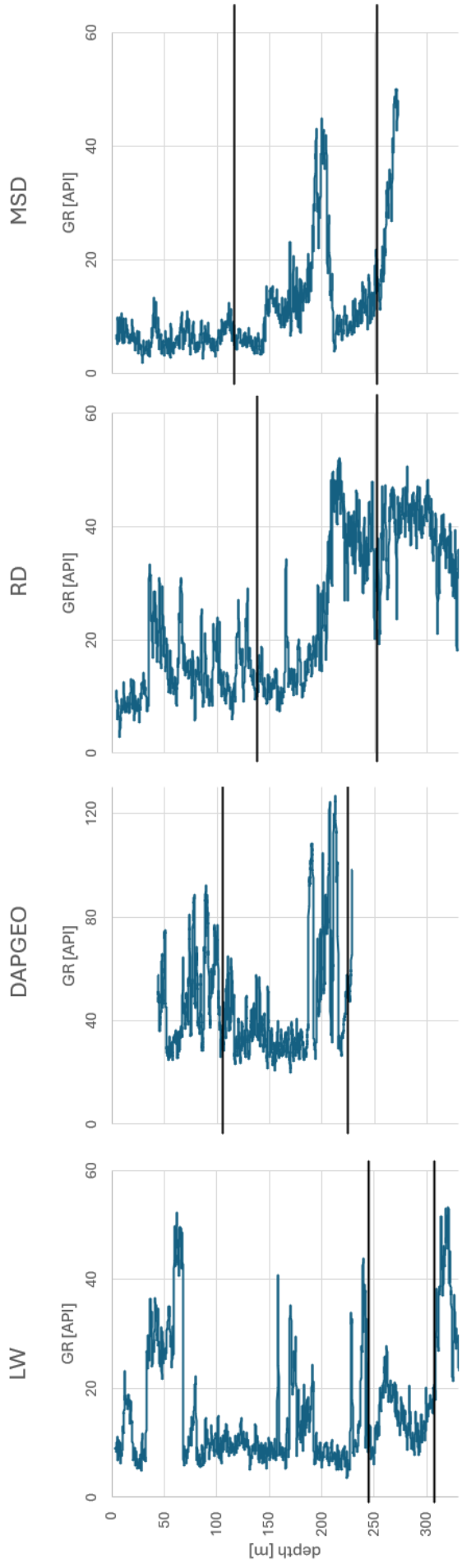

Figure B.2: Gamma Ray logs for the 4 wells, with top and bottom of the Maassluis formation marked

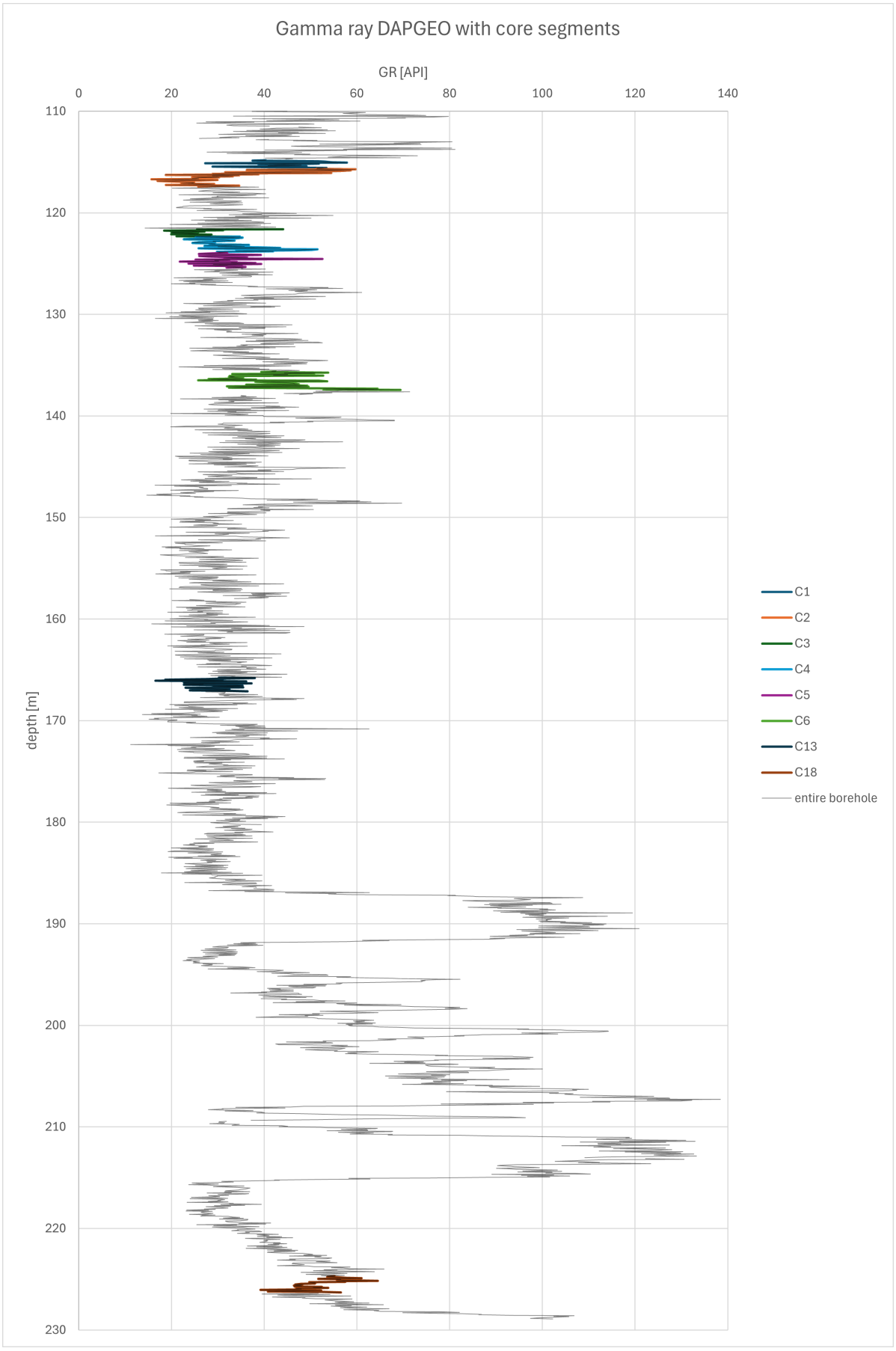

Figure B.3: Gamma ray 50cm moving average of the DAPGEO borehole with the segments from which the 8 cores were taken highlighted

C

Appendix Models

Table C.1: Recovery Efficiencies for the Different Cases and Models simulated after various number of yearly cycles

Model	Year 3	Year 5	Year 10	Year 20
Case 2 / Cases 4				
average aq, aqt	0.7923	0.8320	0.8674	0.8911
max aq, max aqt	0.7832	0.8232	0.8588	0.8826
max aq, min aqt	0.7905	0.8307	0.8666	0.8912
min aq, max aqt	0.7923	0.8314	0.8662	0.8906
min aq, min aqt	0.7989	0.8383	0.8734	0.8969
Case 3				
average aq, aqt	0.7409	0.7636	0.7852	0.8053
max aq, max aqt	0.7356	0.7602	0.7834	0.8041
max aq, min aqt	0.7407	0.7647	0.7870	0.8088
min aq, max aqt	0.7398	0.7615	0.7819	0.8009
min aq, min aqt	0.7443	0.7655	0.7854	0.8048
Case 5 High Cond				
average aq, aqt	0.7099	0.7283	0.7502	0.7728
max aq, max aqt	0.7062	0.7265	0.7499	0.7727
max aq, min aqt	0.7105	0.7302	0.7535	0.7772
min aq, max aqt	0.7083	0.7257	0.7462	0.7676
min aq, min aqt	0.7121	0.7289	0.7493	0.7731
Case 5 Low Cond				
average aq, aqt	0.7675	0.7971	0.8216	0.8402
max aq, max aqt	0.7606	0.7915	0.8172	0.8391
max aq, min aqt	0.7666	0.7972	0.8227	0.8424
min aq, max aqt	0.7670	0.7957	0.8187	0.8367
min aq, min aqt	0.7724	0.8007	0.8236	0.8412
Case 5 Lower Anisotropy				
average aq, aqt	0.6966	0.7174	0.7454	0.7722
max aq, max aqt	0.6934	0.7159	0.7450	0.7717
max aq, min aqt	0.6975	0.7195	0.7490	0.7777
min aq, max aqt	0.6948	0.7145	0.7414	0.7692
min aq, min aqt	0.6984	0.7177	0.7464	0.7731

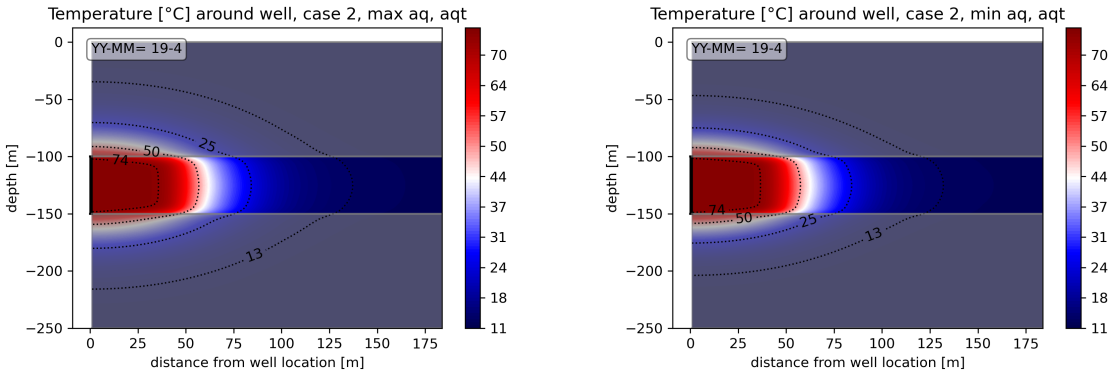

(a) Maximum thermal conductivity **(b)** Minimum thermal conductivity

Figure C.1: Thermal plumes of two scenarios from case 2, without buoyancy flow, after 20 years

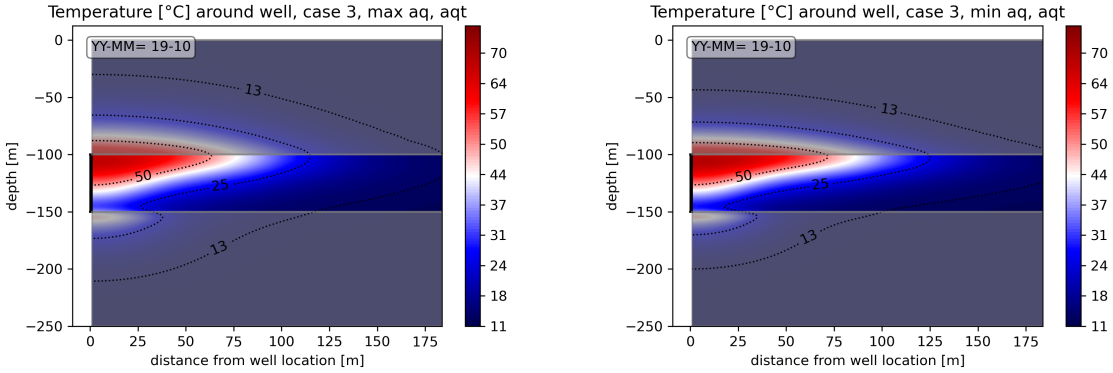

(a) Maximum thermal conductivity **(b)** Minimum thermal conductivity

Figure C.2: Thermal plumes of case 3 after 20 years, after extraction, with minimum plume extend

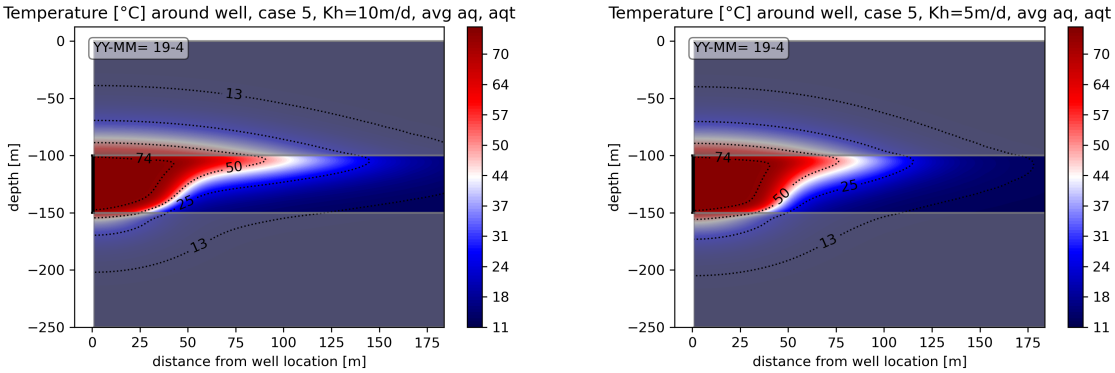

(a) Higher aquifer hydraulic cond. **(b)** Lower aquifer hydraulic cond.

Figure C.3: Temperature plumes after 20 years for same thermal properties, cases with higher and lower hydraulic cond.

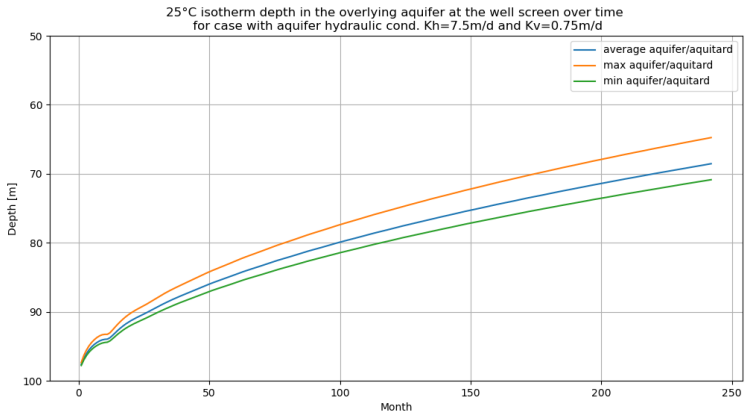

Figure C.4: Temperature impact in overlying clay layer for varied thermal conductivity over the simulation time

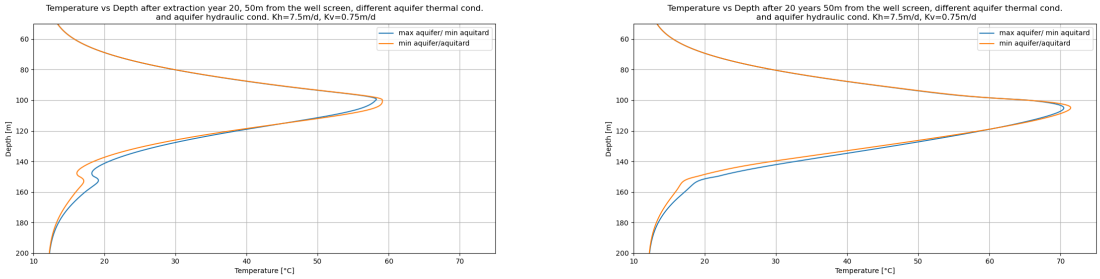

(a) After extraction

(b) After injection

Figure C.5: Thermal impact in overlying clay, in year 20 for varied aquifer thermal conductivity